



# **Control Methods for Low-Inductance and High-Power Permanent Magnet Synchronous Motors with High Number of Poles**

## **Dissertation**

zur Erlangung des akademischen Grades

**Doktoringenieur**

**(Dr.-Ing.)**

von M.Sc. Dmytro Golovakha

geb. am 06. August 1991 in Dokutschajewsk, Donezk Gebiet, Ukraine

genehmigt durch die Fakultät für Maschinenbau

der Otto-von-Guericke-Universität Magdeburg

Gutachter:

Prof. Dr.-Ing. Roland Kasper (OvGU Magdeburg)

Prof. Dr.-Ing. habil. Olga Tolochko (NTUU "KPI" Kiew)

Promotionskolloquium am 24. August 2020

*to the two most important women in my life - my wife Sofia and mother Larisa*

## Acknowledgment

This thesis was developed during my employment as a research assistant at the Institute of Mobile Systems (IMS) at Otto von Guericke University Magdeburg, Germany.

First, I would like to express my high appreciation to my doctoral adviser Prof. Dr.-Ing. Roland Kasper for his unconditional support on my academic development. He was always available for intensive discussions and put a lot of effort into the advance of my research.

In addition, I would like to thank Prof. Dr.-Ing. habil. Olga Tolochko (National Technical University of Ukraine "Igor Sikorsky Kyiv Polytechnic Institute") for agreeing to be the co-examiner of my dissertation and for her valuable suggestions improving the quality of my dissertation thesis.

Furthermore, I would like to thank my colleagues at IMS. It was my great pleasure to work with Dr.-Ing. Wolfgang Heinemann, Dr.-Ing. Olaf Petzold, Dr.-Ing. Martin Schünemann, Dr.-Ing. Valery Makhavikou, Dr.-Ing. Norman Borchardt, Sergey Perekopskiy, Andreas Zörnig, Hadi Amiri, Ralf Hinzelmann, Martin Schmidt, Oleksii Sasin and others, who have supported me in all aspects of life, both mentally and technically.

Also, I would like to express my gratitude to my first Alma Mater – Donetsk National Technical University and Prof. Dr.-Ing. Victor Kalashnikov for the first and fundamental knowledge in the theory of electric drive.

Finally, my deepest gratitude goes to my beloved wife Sofia, my mother Larisa, my godfather Oleg, my other family members and my friends for their support in this challenging but interesting journey.

*Magdeburg in 24. August 2020*

*Dmytro Golovakha*

## **Kurzfassung / Abstract**

### **Kurzfassung**

In dieser Dissertation wird eine OTMIC Regelung (Combined Optimal Torque and Modal Current Control) für Synchronmotoren mit geringer Induktivität, hoher Leistung und hoher Anzahl der Permanentmagnete vorgestellt. Diese Regelungsmethode wurde bei Radnabenmotoren mit nutzenloser Luftspaltwicklung und kombinierter Wicklung implementiert, die von der Otto von Guericke Universität entwickelt und patentiert wurden. Eine niedrige Phaseninduktivität, eine hohe Polpaarzahl und zusätzliche Oberwellen in dem Magnetfeld erschweren die Motorregelung. Aufgrund der geringen Induktivität ist eine hohe Schaltfrequenz erforderlich, um die Phasenstromrippel zu minimieren. Das bedeutet, dass der Steueralgorithmus sehr einfach zu implementieren sein sollte und gleichzeitig eine hohe Dynamik und Systemstabilität bieten sollte, um Motorverluste und Drehmomentrippeln zu reduzieren. Der in dieser Dissertation vorgeschlagene und validierte OTMIC-Kontrollansatz entspricht diesen Anforderungen. Zusätzlich zu dieser Methode wird in der Arbeit auch eine modifizierte sechsstufige Kommutierung mit einer Quellenstromregelung ohne Verwendung einer hohen Schaltfrequenzen aufgrund der Optimierung eines DC-DC-Wandlers vorgestellt. Diese Methode ist der OTMIC-Regelung in der Systemdynamik deutlich unterlegen. Aufgrund seiner Einfachheit kann es jedoch eine Anwendung im Elektrotransport mit geringer und mittlerer Leistungsebene finden. Darüber hinaus kann der Optimierungsalgorithmus des Wandlers in Systemen verwendet werden, um die Abmessungen, Gewicht und Verluste des Wandlers zu minimieren. Somit deckt diese Dissertation den Hauptbereich von Aufgaben ab, die sich beim Entwurf von Steuerungssystemen für elektrische Antriebe mit niedriger Induktivität und hoher Leistung auf der Basis der PMSM ergeben. Darüber hinaus können die in dieser Dissertation vorgestellten Algorithmen auch für standardmäßige PMSM-Antriebe mit hoher Phaseninduktivität verwendet werden.

### **Abstract**

In this dissertation, a Combined Optimal Torque and Modal Current Control (OTMIC) approach for low inductance and high-power permanent magnets synchronous motors is presented. This control method has been implemented on slotless air gap winding and combined winding wheel-hub motors developed and patented by Otto von Guericke University. A low phase inductance, a high number of poles and additional harmonics in a magnetic field of these motors make the motor control a challenge. Due to low inductance, a high switching frequency is required to minimize phase current ripples. This means that the control algorithm should be significantly simple to implement, and at the same time it should be able to provide high dynamics and system stability reducing motor losses and torque ripples. The OTMIC control approach proposed and validated in this dissertation is consistent with these requirements. In addition to this method, a modified six-step commutation with a source current control without using a high switching frequency due to optimization of a DC-DC converter is also presented in the work. This method is significantly inferior to the OTMIC control in the system dynamics. However, it can find its application in inexpensive and low and middle-power mobile applications due its simplicity. In addition, the converter optimization algorithm can be used in systems where dimensions, weight and loss of the electric drive elements matter. The control methods presented in this paper can be applied to standard PMSMs with high inductance. Thus, this dissertation covers the main range of tasks that arise during designing of control systems for low-inductance and high-power electric drives based on the PMSMs. Moreover, the algorithms presented in this dissertation can also be applied to conventional PMSM drives with high phase inductance.

## Content

Acknowledgment .....	III
Kurzfassung / Abstract .....	IV
List of Figures .....	VII
List of Tables.....	X
List of Symbols .....	XI
List of Abbreviations.....	XV
1. Introduction.....	1
2. State of the Art.....	3
2.1 Electric Wheel – Hub Motors .....	3
2.2 Air Gap and Combined Winding Design.....	7
2.3 Problem Statement .....	9
3. Theoretical Framework of PMSM Control.....	11
3.1 PM Motor Operation Principle .....	11
3.1.1 Mathematical Model of PMSM with Air Gap Winding.....	11
3.1.2 Air Gap Winding PM Motor Losses.....	13
3.2 Space Vector PWM.....	15
3.3 Scalar Based Motor Control.....	18
3.4 Vector Control .....	20
3.4.1 Space Vector Representation.....	21
3.4.2 Field Oriented Control.....	25
3.4.3 Direct Torque Control .....	27
3.4.4 Optimal Control.....	29
3.5 Six-Step Commutation Control.....	32
3.5.1 Six-Step Commutation Logic .....	32
3.5.2 Six-Step-Commutation with Control of Source Current .....	35
3.6 Comparison of Conventional Control Methods.....	38
4. Air Gap Winding Motor Control without the Use of High Switching Frequency.....	39
4.1 Optimization of a Multiphase Interleaved Buck-Boost Converter .....	39
4.2 Optimization of Three-Phase Interleaved Converter with Toroid Coil .....	42
4.2.1 Toroid Coil Geometry .....	42
4.2.2 Circuit Operations.....	43
4.2.3 Converter Losses Model.....	46
4.3 Optimization Results of Three-Phase Interleaved Buck Converter.....	48
4.3.1 Input Parameters .....	48
4.3.2 Optimization Results and Validation.....	49
5. Combined Optimal Torque and Modal Current Control.....	53
5.1 Optimal Torque Control for Minimal Motor Losses .....	53
5.2 Optimal Torque Control for Minimal Torque Ripple .....	55
5.3 Modal Current Control.....	57
5.4 Modified Space Vector PWM.....	60
5.5 Control Structure of OTMIC Approach.....	61

---

6.	Modelling and Validation of OTMIC Approach .....	65
6.1	Microcontroller Programming .....	66
6.1.1	Control System Operation .....	66
6.1.2	Phase Currents Measurement .....	70
6.1.3	Electrical Angle Measurement .....	71
6.2	OTMIC Control of Air Gap Winding Wheel-Hub Motor .....	75
6.2.1	Air Gap Winding Wheel-Hub Motor.....	75
6.2.2	48V Experimental Setup.....	76
6.2.3	Offline Calculation of Air Gap Winding Motor Control System.....	77
6.2.4	Step Response of OTMIC Control .....	79
6.2.5	Air Gap Winding Motor under Normal Operating Conditions .....	81
6.2.6	Losses in Air Gap Winding Wheel-Hub Motor.....	84
6.3	OTMIC Control of Combined Winding Wheel-Hub Motor.....	85
6.3.1	Combined Winding Wheel-Hub Motor .....	85
6.3.2	650V Experimental Setup.....	87
6.3.3	Offline Calculation of Combined Winding Motor Control System .....	88
6.3.4	Combined Winding Motor under Normal Operating Conditions.....	90
7.	Conclusion .....	95
	References .....	98
	Appendix .....	107
	Appendix A – Six-step Commutation with Source Current Control .....	107
	Appendix B – Accuracy Verification of Allegro Current Sensors .....	108

## List of Figures

Fig. 1	Left: Tesla Motors Model S [34]; right: Audi e-tron quattro [35].	3
Fig. 2	Protean Electric Pd18 (left) [25] and Schaeffler "E-Wheel Drive" [29] Wheel-Hub Motors.	4
Fig. 3	Wheel Module (left) and Vehicle Concept Designed for the Future from Protean [25].	5
Fig. 4	The Wheel Module (right) and Vehicle Concept Designed for the Future from Schaeffler [29].	5
Fig. 5	Prototypes of Elisa II and LeiRaMo Wheel Hub Motors, a Scooter Motor and a Boat Motor [3],[4].	6
Fig. 6	Production of Air Gap Winding [14].	7
Fig. 7	Comparison of Conventional, Air Gap and Combined Winding Designs for PMSM	8
Fig. 8	Comparison of the conventional magnetization (a) and Halbach array magnetization (b) adapted for air gap and combined winding technologies [9].	9
Fig. 9	Classification of different control techniques for PMSM with air gap and combined winding [20],[47].	10
Fig. 10	B6 – Bridge - Fed 3-Phase PMSM Drive Connections [1]-[22].	12
Fig. 11	Top: B-Field in Air-Gap Winding. Bottom: B-Field Harmonic Spectrum with coefficients $b_k$ [2].	13
Fig. 12	Left: Principle of SVPWM; Right: Hexagon Sector Identification Logic. Left: Principle of SVPWM; Right: Hexagon Sector Identification Logic.	17
Fig. 13	SVPWM of a Three-Phase DC-AC Converter.	18
Fig. 14	Open-Loop Block Diagram of Volt per Herz Control of PMSM.	19
Fig. 15	Illustration of Stationary $\alpha\beta$ and Synchronous $dq$ Reference Frames.	22
Fig. 16	Current PID Control Configuration in Space Vector Representation.	24
Fig. 17	Field Oriented Control (FOC) Block Diagram for PMSM.	25
Fig. 18	PMSM Operation in Normal Range and Field Weakening Range.	26
Fig. 19	Direct Torque Control Block Diagram for PMSM.	28
Fig. 20	LQR Control Block Diagram for PMSM.	30
Fig. 21	FCS-MPC Control Block Diagram for PMSM.	31
Fig. 22	Ideal Three-Phase Currents in Comparison to B-Fields in SSC.	33
Fig. 23	Hall Sensors in CAD-Model (left) and Schematic (right) [18].	34
Fig. 24	Block Diagram of SSC with Input Current Control by Means of DC-DC Converter	35
Fig. 25	Operating Modes of the DC-DC Buck Converter.	36
Fig. 26	Current PI Control Loop for SWC Control [81].	36
Fig. 27	Flowchart of Multiphase Interleaved DC-DC Converters Optimization [7].	41
Fig. 28	Toroidal Core with Optimization Parameters.	42

Fig. 29	Three-Phase Interleaved Buck DC-DC Converter.	43
Fig. 30	Hysteresis Loop and Magnetization Curve $B_M(H)$ .	44
Fig. 31	Results of three-phase interleaved buck converter optimization.	50
Fig. 32	Two prototypes of a three-phase interleaved buck converter (left, middle) and comparison of optimized and non-optimized coils (right).	50
Fig. 33	Measured and Simulated Currents and Output Current of the Three Coils.	51
Fig. 34	Measured and Calculated Converter Total, Conduction, Switching and Coils Losses.	51
Fig. 35	Modal Current Control Loop for Modal Currents $J_{1,2}$	58
Fig. 36	Proposed OTMIC control diagram of PMSM drive system	62
Fig. 37	Flowchart of OTMIC Control Loop for PMSM.	63
Fig. 38	Approximate Relationship between Current Ripples and Switching Frequency.	66
Fig. 39	Control System Operation in Online Mode.	67
Fig. 40	Block Diagram of Proposed OTMIC Control without back-EMF Compensation.	68
Fig. 41	Block Diagram of Conventional FOC without back-EMF Compensation and Decoupling.	68
Fig. 42	Gate Signals Generation by means of MSVPWM, FRT and OCU.	68
Fig. 43	MFT Peripheral Component Interconnection.	69
Fig. 44	Flowchart of OTMIC and FOC Control Loop.	69
Fig. 45	Phase Current Measurement.	70
Fig. 46	Rotor Position and Angular Velocity Estimation with QPRS.	71
Fig. 47	Practical Implementation of the Electric Angle Estimation Process with Incremental Encoder.	72
Fig. 48	Hall Sensors for Electric Angle Estimation.	73
Fig. 49	Practical Implementation of the Electric Angle Estimation Process with Analog Hall Sensors.	74
Fig. 50	Wheel Hub Motor for a Hub-Less Scooter of OvGU left: CAD Model, right: Prototype	75
Fig. 51	Experimental Setup for 48V OTMIC Control System Verification.	77
Fig. 52	Control Hardware for 48V OTMIC Control System Verification.	77
Fig. 53	Optimal Current and Torque Waveforms for (a): Minimal Torque Ripples; (b): Minimal Motor Losses.	78
Fig. 54	Open/Closed Loop Bode Diagrams of OTMIC Control for Air Gap Winding Wheel-Hub Motor.	79
Fig. 55	Step Response of Simulation and Measured Phase Currents and Electrical Torque.	80
Fig. 56	Calculation Process of OTMIC Control Algorithm in the Microcontroller during Step Response.	80
Fig. 57	Simulated Phase Currents and Electrical Torque $T_E$ of (a): OTMIC with Torque Ripple Optimization; (b): OTMIC with Losses Optimization; (c): Conventional FOC control. (d): Harmonic Spectrum of Phase Current (left) and Torque (right) for Every Method.	82



Fig. 58	Experimental Results of Measured Phase Currents and Output Torque $T_M$ of (a): OTMIC with Torque Ripple Optimization; (b): OTMIC with Losses Optimization; (c): Conventional FOC Control. (d): Harmonic Spectrum of Phase Current (left) and Torque (right) for Every Method.	82
Fig. 59	Validation of Torque Ripples for every Method (a): Simulated RMS Value of Electrical Torque; (b): Measured RMS Value of Electrical Torque.	83
Fig. 60	Simulation Results of Phase Currents and Torque During normal Operation with Rated Power of Air Gap Winding Motor (a): OTMIC with Torque Ripple Optimization; (b): Conventional FOC Control. (c): Harmonic spectrum of Phase Current (left) and Torque (right) for Every Method.	83
Fig. 61	Ohmic Motor Losses Simulation for OTMIC and FOC Control Methods	84
Fig. 62	Combined Winding Wheel Hub Motor of OvGU, left: CAD model, right: Prototype	86
Fig. 63	Experimental Setup for 650V OTMIC Control System Verification.	87
Fig. 64	Motor Control Hardware for 650V OTMIC Control System Verification.	88
Fig. 65	B-field in a Combined Winding with its Harmonic Spectrum (left). Optimal Current and Torque Waveforms for a Combined Winding Motor (right).	88
Fig. 66	Open/Closed Loop Bode Diagrams of OTMIC Control for Combined Winding Wheel-Hub Motor.	89
Fig. 67	Simulated Phase Currents and Electrical Torque $T_E$ of (a): OTMIC with Torque Ripple Optimization; (b): Conventional FOC Control. (d): Harmonic Spectrum of Phase Current (left) and Torque (right) for Every Method.	91
Fig. 68	Experimental Results of Measured Phase Currents and Output Torque $T_M$ of (a): OTMIC with Torque Ripple Optimization; (b): Conventional FOC Control. (d): Harmonic Spectrum of Phase Current (left) and Torque (right) for Every Method.	91
Fig. 69	Validation of Torque Ripples for OTMIC and FOC Methods (a): Simulated RMS Value of Electrical Torque; (b): Measured RMS Value of Electrical Torque.	92
Fig. 70	Calculation Process of OTMIC Control Algorithm in the Microcontroller: Simulation (left) and Experimental Results (right).	92
Fig. 71	Simulation Results of Phase Currents and Torque during Normal Operation with Rated Power of Combined Winding Motor (a): OTMIC with Torque Ripple Optimization; (b): Conventional FOC Control, (c): Harmonic Spectrum of Phase Current (left) and Torque (right) for Every Method.	93

## List of Tables

TABLE I.	Comparison of Wheel-Hub Motor DevelopmentsFig. 1	6
TABLE II.	Phase Voltage according to Switching State	16
TABLE III.	Switching Time Estimation for each Sector	17
TABLE IV.	Eight-vector Switching Table of DTC	28
TABLE V.	B-Fields Difference in Six Intervals	33
TABLE VI.	SWITCHING TABLE OF COMMUTATION SIGNALS	34
TABLE VII.	Comparison of Conventional Control Methods for Low Inductance PMSM	38
TABLE VIII.	Parameters of Three-phase Interleaved Buck Converter	49
TABLE IX.	MSVPWM Switching Table	61
TABLE X.	Microcontroller and Current Sensor Parameters	67
TABLE XI.	Electrical Angle Estimation with Hall Sensors	74
TABLE XII.	Air Gap Winding Wheel-Hub-Motor Parameters	76
TABLE XIII.	Parameters of Three-phase Interleaved Buck Converter	78
TABLE XIV.	Combined Winding Wheel-Hub-Motor Parameters	87
TABLE XV.	Control System Parameters for Combined Winding Motor	89

## List of Symbols

Symbols	Description	UOM
$\underline{a}$	vector with phase current harmonic coefficients	
$\underline{a}_L$	current harmonic coefficients for motor losses minimization	
$\underline{a}_\tau$	current harmonic coefficients for torque ripples minimization	
$A_{wire}$	cross-section area of the coils wire	$m^2$
$A_{core}$	cross-section area of the coils core	$m^2$
$\alpha, \beta$	discrete eigenvalues of motor and current sensor	
$\underline{B}$	B-fields acting on three-phases	$T$
$\underline{b}$	vector with B-Field harmonic coefficients	
$\underline{B}_{coils}$	B-fields acting on coils	$T$
$b_{core}$	coils core width	$m$
$c$	constant of coulomb friction and hysteresis loss in PMSM	$Nm$
$C_{bc}$	buck converter capacitor	$F$
$C_{GD}$	gate-drain capacity	$F$
$C_{M12}$	torque coefficient	
$d$	constant of linear mechanical friction and eddy loss in PMSM	$Nm \cdot s/rad$
$D_r$	rotor outer diameter	$m$
$D_{ri}$	shaft diameter	$m$
$D_b$	mean bearing diameter	$m$
$\underline{d}_{PWM}$	duty cycle ratios for three-phases	%
$D_{bc}$	buck converter duty cycle	%
$d_{wire,2}$	coils wire width	$m$
$d_{wire,1}$	coils wire height	$m$
$D_{MS}$	open-loop discrete transfer function	
$D_C$	PID controller discrete transfer function	
$D$	discrete closed loop transfer function	
$\Delta t$	sampling time	$s$
$\Delta t_{bc}$	buck converter switching period	$s$
$\underline{e}$	three-phase back-EMFs	$V$
$E_{onM}$	switch-on energy losses	$J$
$E_{offM}$	switch-off energy losses	$J$
$E_{onD}$	energy loss in the diode due to the inverse recovery effect	$J$
$f_{rm}$	remagnetisation frequency	$Hz$
$f_{PWM}$	switching frequency	$Hz$
$f_e$	commutation frequency	$Hz$
$f_{rated}$	rated PMSM frequency	$Hz$
$f_{e,cr}$	critical PMSM frequency	$Hz$
$f_{MFT}$	MFT tact frequency	$Hz$
$f_{FRT}$	FRT frequency	$Hz$
$f_{AAF}$	frequency of anti-aliasing filter	$Hz$

$F_B$	bearing load	$N$
$G_M$	PMSM transfer function	
$G_S$	current sensor transfer function	
$G_{MS}$	open-loop transfer function	
$\underline{\Gamma}^+$	pseudo inverse transformation matrix	
$H$	magnetic field strength acting on stator	$A/m$
$\underline{H}_{Coils}$	magnetic field strength acting on coils	$A/m$
$h_{core}$	coils core height	$m$
$h_L$	air gap high	$m$
$i_{DC}$	B6 input current	$A$
$\underline{i}$	three-phase line-to-neutral currents	$A$
$\bar{i}_s$	space vectors of three-phase current	$A$
$i_{xy}$	buck converter output current	$A$
$i_{xy,a}$	average buck converter output current	$A$
$\dot{i}_{Coils}$	coils currents	$A$
$\underline{J}$	modal currents	$A$
$k_M$	motor geometric constant	$Nm/(TA)$
$k_w$	roughness coefficient	
$K_P$	PID proportional gain	$V/A$
$K_I$	PID integral gain	$V/A$
$K_D$	PID derivative gain	$V/A$
$\underline{K}_{opt}$	optimal phase current waveforms	$A/Nm$
$L_s, M_s$	phase self and mutual inductances	$H$
$l_s$	stator height	$m$
$l_{wire}$	length of the coil wire	$m$
$l_{core}$	length of the coil core	$m$
$\underline{L}_{Coils}$	coils inductance	$H$
$L_{bc}$	buck converter inductor	$H$
$m_{wire}$	coils wire mass	$kg$
$m_{core}$	coils core mass	$kg$
$m_{Coils,\Sigma}$	coils weight	$kg$
$\underline{M}_{Coils}$	magnetization of three coils	$A/m$
$\mu_r \mu_0$	relative and free space permeabilities	$H/m$
$\mu_{sl}$	sliding friction coefficient	
$\eta_M$	PMSM efficiency	%
$N_D$	PID derivative filter coefficient	
$N_{CC}$	maximum FRT value	
$\sigma$	electrical conductivity	$Sm$
$p$	number of poles	
$P_E$	PMSM electrical power	$W$
$P_M$	PMSM mechanical power	$W$
$P_L$	PMSM total power losses	$W$
$P_\Omega$	PMSM ohmic losses	$W$
$P_W$	PMSM eddy current losses	$W$
$P_H$	PMSM hysteresis losses	$W$

$P_p$	PMSM friction losses	$W$
$P_{no}$	PMSM non-ohmic losses	$W$
$P_{F,bearing}$	bearing friction losses	$W$
$P_{F,w}$	air friction losses	$W$
$P_{BC,\Sigma}$	buck converter total losses	$W$
$P_{Coils,Core}$	buck converter iron losses	$W$
$P_{Coils,\Omega}$	buck converter resistive losses	$W$
$P_{BC,Cond}$	buck converter conduction losses	$W$
$P_{BC,Switch}$	buck converter switching losses	$W$
$\rho_{20^{\circ}}$	phase resistivity measured at $20^{\circ}C$	$\Omega m$
$\rho_{Cu}$	phase resistivity of the wire material	$\Omega m$
$Q_{rr}$	reverse recovery charge	$\mu C$
$R_s$	phase resistance	$\Omega$
$R_{Coil}$	coils resistance	$\Omega$
$R_{DS}$	drain-source resistance	$\Omega$
$R_G$	gate resistance	$\Omega$
$r_{core}$	coils core radius	$m$
$r_s$	winding radius in motor	$m$
$S_{1,2,3,4,5,6}$	B6 switching signals	
$St_{1,2,3,4,5,6}$	switching times	
$S_R$	cross – section of the conductor	$m^2$
$S_{bc1,2}$	buck converter switching signals	
$S_{CS}$	current sensor sensitivity	$V/A$
$t$	time	$s$
$t_{fu}$	voltage drop time	$s$
$t_{ru}$	voltage rise time	$s$
$t_{fi}$	current drop time	$s$
$t_{ri}$	current rise time	$s$
$t_M$	PMSM time constant	$s$
$t_S$	current sensor time constant	$s$
$t_{Req}$	requested time constant	$s$
$T_M$	PMSM output torque	$Nm$
$T_E$	electrical torque generated in the winding	$Nm$
$T_L$	PMSM loss torque	$Nm$
$T_A$	average electrical torque	$Nm$
$T_R$	PMSM torque ripple	$Nm$
$\underline{u}$	three-phase line-to-neutral voltages	$V$
$u_{DC}$	supply DC voltage	$V$
$ \hat{u} _{rated}$	peak value of the equivalent rated stator voltage	$V$
$ \hat{u} _{cr}$	voltage amplitude at the critical frequency	$V$
$ \hat{u} $	magnitudes of the voltage vector	$V$
$\bar{u}_s$	space vectors of three-phase voltage	$V$
$\underline{u}_{Coils}$	coils voltages	$V$
$U_{DR}$	the driver output voltage	$V$
$U_{plateau}$	gate plateau voltage	$V$

$U_{ind\_on}$	overvoltage during the switching-on time	$V$
$U_{ind\_off}$	overvoltage during the switching-off time	$V$
$U_{IOUT(Q)}$	sensor zero current output voltage	$V$
$U_{OE}$	current sensor offset	$V$
$V_{Ref}$	rotating space vector	$V$
$V_{1,2,3,4,5,6}$	switching states	
$V_{Core}$	coils core volume	$m^3$
$\underline{V}$	modal input voltages	$V$
$V_M$	volume of the magnetic material	$m^3$
$\underline{v}_m$	modulating signals in SVPWM	$V$
$\underline{W}$	modal transformation	
$\omega_M$	angular velocity	$rad/s$
$\omega_e$	electrical angular velocity	$rad/s$
$\varphi_e$	electrical angular rotor position	$rad$
$\varphi_M$	mechanical angular rotor position	$rad$
$ \hat{\psi} $	magnitudes of the flux linkage vector	$Wb$
$\bar{\psi}_s$	space vector of magnetic flux	$Wb$
$\psi_M$	constant flux amplitude induced by the permanent magnets	$Wb$
$\theta_\psi$	stator flux phase	$rad$
$\delta$	motor/sensor speed ratio	
$\delta_{sd}$	skin depth	$m$
$\underline{x}_{7..9}$	coils core material coefficients	

## List of Abbreviations

AC	Alternating Current
AAF	Anti-Aliasing Filter
ADC	Analog-to-Digital Converter
B-Field	Magnetic Flux Density
BLDC	Brushless Direct Current Motor
CAD	Computer-Aided Design
CO <sub>2</sub>	Carbon Dioxide
CDOS	Conjugate Direction with Orthogonal Shift
CCS	continues control set
CPU	Central Processing Unit
DC-AC	Direct Current to Alternating Current
DC-DC	Direct Current to Direct Current
DTC	Direct Torque Control
EMF	Back Electromotive Force
FOC	Field Oriented Control
FCS	finite control set
FPU	On-chip Floating-Point Unit
FRT	Free-Running Timer
$HS_1, HS_2, HS_3$	Analog Hall Sensors 1,2,3
$HS_A, HS_B$	Digital Hall Sensors A, B
JA	Jiles-Atherton
GAN	Gallium Nitride
GM	magnitude margin
LQR	Linear Quadratic Regulator
OCU	Output Compare Unit
OvGU	Otto von Guericke University
OTMIC	Optimal Torque and Modal Current Control
MMF	Magnetomotive Force
MPC	Model Predictive Control
MSVPWM	Modified SVPWM

MFT	Multifunction Timer
NLC	Non-Linear Control
PWM	Pulse-Width Modulation
PMSM	Permanent Magnet Synchronous Motor
PM	Permanent Magnet
PHM	phase margin
PWC	Pulse Width Count
PID	Proportional–Integral–Derivative Controller
QPRC	Quadrature Position/Revolution Counter
RMS	Root mean square
SIC	Silicon Carbide
SVPWM	Space Cector Pulse Width Modulation
SBC	Scalar Based Control
SSC	Six-Step Commutation
SKF	Svenska Kullagerfabriken
T1, T2, T3, T4, T5, T6	Transistors 1,2,3,4,5,6
WFG	Waveform Generator



# 1. Introduction

The decline in oil reserves and the desire to reduce CO<sub>2</sub> emissions have led to emergence of numerous studies in the field of electric vehicles over the past two decades. Even though the effectiveness of solving the problem of environmental pollution using local zero emissions remains controversial, they can make a significant contribution to improving air quality in urban areas and urban centers. Demand for electric cars is growing every year, and today many of them surpass gasoline cars in terms of dynamic performance, efficiency as well as low noise. In addition, the design of the car can be completely changed due to removal of the internal combustion engine with all auxiliary units, the exhaust system, the mechanical elements of transmission, differential, tank and other specific drive components. On the other hand, an electric motor has much more advantages compared to a gasoline engine in terms of compatibility with other rapidly developing technologies such as a fuel cell or autonomous transport. But replacing a gasoline engine with a conventional electric motor is not an optimal solution since it does not allow to achieve all advantages of an electric vehicle. Therefore, various research projects have appeared, which, among other things, adopted the technology of a wheel-hub motor. Numerous conceptual studies have shown great prospects for the development of this technology.

One of the most central advantages of the wheel-hub motor is the direct connection between the electric motor and the wheel without any mechanical transmission elements such as shafts, gears, belts, etc. Therefore, the dynamics of torque and rotational speed of the wheel and the car directly depends on the moment inertia of the wheel-hub motor. These electric motors provide torque much faster than internal combustion engines due to their low electrical and mechanical time constant. Moreover, the safety systems used to stabilize cars, such as ABS and ESC, can work with significantly shorter response times, which can make the car even more stable in extreme conditions such as on ice or in a sharp bend. The drive train of an electric vehicle based on an electric drive with wheel-hub motors is much more compact in comparison to electric vehicles with conventional motors. Its main elements are a rechargeable battery, wheel motors including power electronics, a cooling system and a control unit. In some cases, a DC-DC converter can be added to the system to increase or decrease the supply voltage from the battery or from the fuel cell and energy recuperation. Such a small number of units makes it possible to release a lot of space in a vehicle, opens enormous opportunities for the design of mobile applications such as e-Cars, e-Scooter, Drones, e-Longboards etc.

The first important question in this topic has involved the study of the critical effect of the increased mass of wheels spring-loaded with tires on safety and driving comfort. Based on the studies [36]-[38], it can be concluded that increase in the mass of the wheels to 30 kg for a medium-size vehicle is not critical. However, it has also been noted in [38] that, with an increase in the mass of the engine, safety and driving comfort decrease during cornering. In addition, dynamic fluctuations in the load on the wheel under certain conditions can affect the rotation angle of the steering wheel [18]. It means that a driver will have to set large correction angles of the steering wheel. From the point of view of energy, a high mass of the motor leads to higher energy costs and a power loss. These circumstances have become a ground for numerous studies aimed to reduce a motor weight with a simultaneous increase in its power.

Nowadays, the leader in this race to reduce weight and increase the motor power is Otto von Guericke University (OvGU), in which a new type of an electromagnetic structure of the engine based on a permanent magnets synchronous motor has been developed and patented [19]. Whereas the other types of wheel-hub motors are based on the standard structure of the generally accepted PMSMs with slots in the stator and a large volume of copper in the winding. The OvGU motor geometry is based on a thin air gap winding. The air gap winding technology allows to achieve high power and torque and at the same time to reduce the weight of the motor significantly. The price of this optimization is expressed in

a very small inductance, a small motor time constant and additional harmonic in the magnetic field, which greatly complicates the motor control system. The solution to this problem will be presented in this dissertation. Moreover, the new design of the OvGU motors allows to use a slot winding with much smaller slots size compared to standard PMSMs that, in its turn, increase the engine power and phase inductance significantly and the weight of the engine slightly.

The dissertation is divided into seven chapters. After introduction and motivation, a brief overview of wheel-hub motors existing nowadays will be presented, and the operation principle of the new air gap winding as well as the combined winding wheel-hub motors with requirements for their control system will be described. Chapter 3.1 will describe a mathematical model of these motors. Besides, the types of conventional PMSM control methods, which can be applied to these motors' structures, will be analyzed in Chapter 3. Chapter 4 will provide a description of the DC-DC converter optimization, by which the motor control for low and medium power mobile applications can be implemented. This algorithm combined with the conventional six-step commutation and a source current control allows to implement a motor control system without using a high switching frequency. This optimization can also be useful in systems where a DC-DC converter is used to increase supply dc voltage or to keep its level. Chapter 5 will introduce a Combined Optimal Torque and Modal Current Control (OTMIC) method. This method has been modeled and adapted specifically for a high-power PMSM motors with very low phase inductance and high number of poles, considering all its features. This method is significantly simple to implement on a conventional microcontroller, which is very important for the high-frequency control. In addition, it gives an opportunity to minimize the motor loss and torque ripples. In Chapter 6, OTMIC control will be validated based on the experimental results and simulations. All the results and knowledge gained are summarized in Chapter 7. Also, proposals for the further development in this research area will be made in the last chapter.

## 2. State of the Art

This chapter will provide a brief overview of the wheel-hub motor technology with an emphasis on motors manufactured using air gap and combined winding designs. At the end of the chapter, the problem statement for this dissertation will be highlighted.

### 2.1 Electric Wheel – Hub Motors

Nowadays, the most part of electric vehicles are manufactured based on the indirect driven wheels characterized by an indirect force transmission between the electric machine and the wheel hub. In order to transmit mechanical power into the wheel hub, this construction requires transmission elements such as gears, belts, shafts, etc. Thus, all components required for power conversion in both motor and generator operation negatively affect the efficiency of an electric drive train close to the wheel. As two one on of the best nowadays examples of a near-wheel drive system, Audi e-tron quattro (right) and Tesla Model S (left) shown in Fig. 1 can be used. Audi e-tron quattro presented by Audi AG in 2018 is characterized by an electrified drive train with one electric motor in the front axle and two electric motors on the rear axle. According to [35], together these motors can operate with 800 Nm peak torque and 320 kW peak power. All-wheel-drive of Tesla Model S P100D with two induction motors behind and one PMSM in front together have 592 kW peak power and 1373 Nm peak engine torque [34]. However, as it can be seen from Fig. 1, the electric drive train close to the wheel is characterized not only by additional mechanical losses in transmission, but also by its large dimensions and weight, which limit the possibilities of the vehicle design.

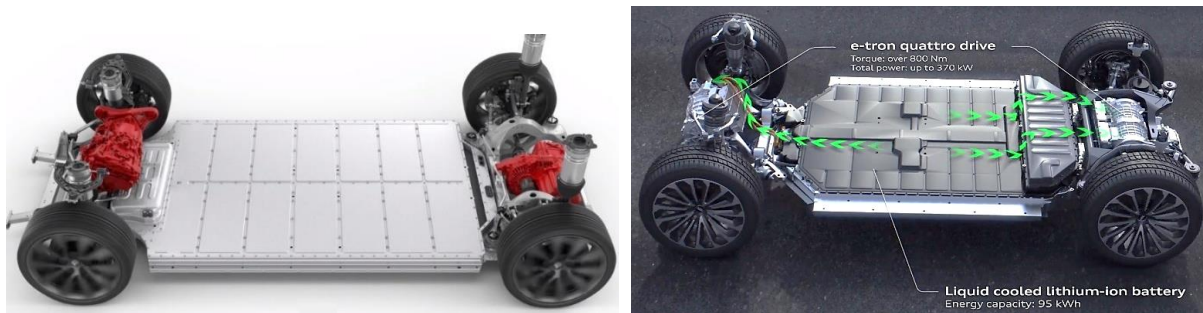


Fig. 1. Left: Tesla Motors Model S [34]; right: Audi e-tron quattro [35].

A new step in the development of electric vehicles can be made thanks to a wheel-hub motor technology. An electric wheel-hub motor allows to achieve a direct connection between the wheel hub and the output side of an electric motor without any transmission elements in the power flow. In addition, the design of wheel-hub motors in general represented by permanent magnets synchronous machine has a compact construction and allows to integrate the power electronics and sensors for rotor position measurements into the internal motor space offering more space in an electric vehicle. Thus, the wheel-hub motor delivers unique benefits for electric vehicles such as:

- greater range and reduced running cost due to the higher efficiency;
- improved driver handling, traction control and stability due to direct connection between a motor and a wheel;
- more space for user and flexible design of mobile applications due to a compact construction;
- reduced development and manufacturing costs of electric vehicles due to a simple electric drive train;
- very good compatibility with the hybrid drive, fuel cell and autonomous driving technology.

In this research activity, Protean Electric Incorporated Company has developed two electric wheel hub motors Pd16 and Pd18 published in [25] and based on the PMSM construction. These wheel-hub motors have been designed for 16- and 18-inch rims and consist of a rotor with internal permanent magnets, a stator with integrated power electronics, a bearing unit and mechanical brakes. In Fig. 2 below, the developed electric wheel hub motor Pd18 is shown in an exploded view (left). This construction has been specifically designed for mass production and is protected by numerous patents. According to [25], the wheel-hub motor Pd18 operated with supply dc voltage equal to 400 V has a rated torque of 650 Nm and rated output power of 60kW with the maximum speed of 1600 rpm or 225 km/h. The motor weight is 36 kg that leads to a high gravimetric power density of 1.66 kW/kg. The integration of the power electronics results in a very compact drive architecture. The motor Pd16 has a reduced performance due to a smaller diameter. Another current development of an electric wheel hub motor has been carried out by Schaeffler AG under the "E-Wheel Drive" name and published in [29]. The motor is shown in Fig. 2 in a sectional view (right). In contrast to Protean Electric wheel hub motors described above, Schaeffler AG is pursuing the concept of an internal rotor designed for a 16-inch rim. This is a highly integrated electrical wheel hub drive consisting of a PMSM machine operated with 420 V supply voltage, a mechanical brake, integrated power electronics and active liquid cooling. In [29], it is shown that the wheel hub motor is supported completely on the wheel bearing and does not have its own motor bearing. In addition, the motor is equipped with an additional mechanical drum brake as a redundant brake unit. The motor can operate with 33 kW rated power, 350 Nm rated torque and has the total weight of 53 kg that leads to the low gravimetric power density equal to 0.62 kW/kg.



Fig. 2. Protean Electric Pd18 (left) [25] and Schaeffler "E-Wheel Drive" [29] Wheel-Hub Motors.

The advantages of wheel-hub motors are clearly visible on prototypes of a wheel module steering system of Protean in Fig. 3 (left) and Schaeffler in Fig. 4 (right). The wheel module has been designed as an electromechanical steer-by-wire system. The control algorithm specifies the direction for complete wheel unit. The wheel module is rotated according to the required direction by means of an actuator integrated in the wheel module coaxially to the steering axis. As it has been mentioned above, the conventional vehicles have a limited wheel steering angle to 45° degrees. The wheel module affords an opportunity to increase this angle to 90° in Schaeffler's concept [29]. The wheel module of Protean can be steered 360° without limitation [25]. This technology facilitates driving in extremely tight urban streets, in loading bays and during parking. In addition, the electromechanical ride height adjustment can be integrated into the wheel module to help passengers to get in and out. Moreover, it leads to the completely new vehicle concepts that bring autonomous transport technologies to a new level.

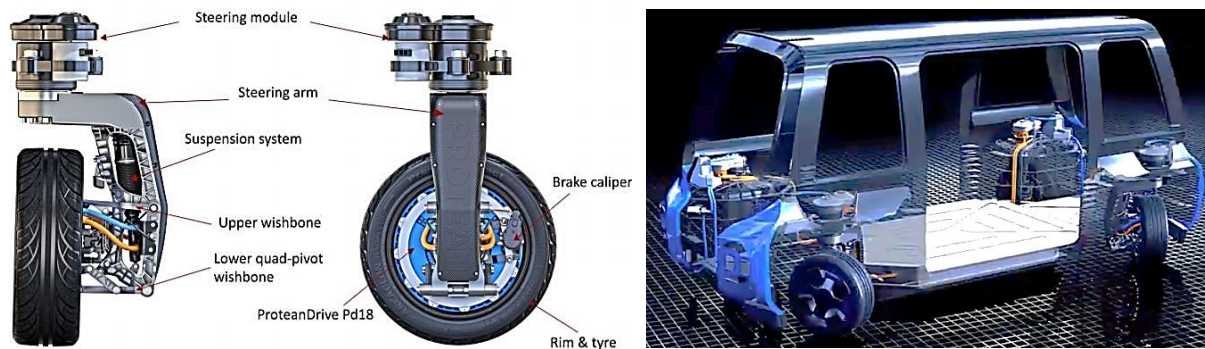


Fig. 3. Wheel Module (left) and Vehicle Concept Designed for the Future from Protean [25].

Wheel-hub motors allow to create a completely new design of mobile applications. For example, the vehicle concepts based on the wheel modules and designed by Protean is shown in Fig. 3 (right) and by Schaeffler in Fig. 4 (left). According to the Schaeffler concept, a wheel-hub module (“Schaeffler Intelligent Corner Module”) with drive components such as batteries, power electronics and control unit have been integrated into a compact vehicle platform with the possibility of further scale to different vehicle sizes. These futuristic concepts are presented for a more detailed presentation of the benefits that a wheel-hub motor can provide.



Fig. 4. The Wheel Module (right) and Vehicle Concept Designed for the Future from Schaeffler [29].

However, the success of these technologies is very dependent on the wheel-hub motor weight. The vertical dynamics of a vehicle is strongly influenced by increase in the wheel masses. According to [36]-[38], an increase in the wheel mass of more than 30 kg is critical for the driving safety and comfort of small and medium-sized vehicles. That is why one of the most central research focuses of an electric wheel-hub motor is its small size, lightweight construction and maximum efficiency, and at the same maintenance of time high torque and power. However, construction of conventional slotted electrical machines doesn't allow to reduce the motor weigh greatly without decreasing its torque and efficiency.

Since 2011, the Otto-von-Guericke University has been researching and building the novel patented principle of a rotating electric permanent magnets synchronous machine with air gap winding in research and industrial projects [10]-[22]. The high potential for increasing the gravimetric power and torque densities compared to the previous lightweight PMSMs is opened by a very thin and light slotless air gap winding or combined air gap and light slotted windings by bonding using double-sided industrial foils [3],[6],[9],[12].

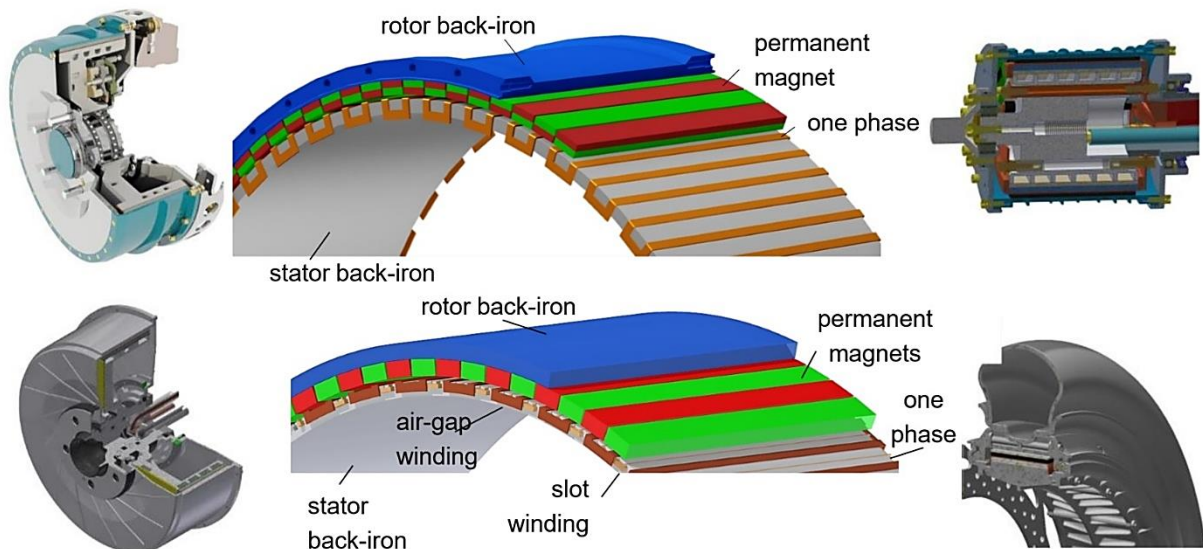






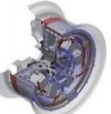


Fig. 5. Prototypes of Elisa II and LeiRaMo Wheel Hub Motors, a Scooter Motor and a Boat Motor [3],[4].

During this time, several prototypes of electrical machines with a new types of air gap (middle, above) and combined winding (middle, below) shown in Fig. 5 have been developed, such as, wheel hub motors for electric vehicles (right, below), e-scooters (left, below), e-bikes, generators, as well as a motor for an electric gliding boat (left, above).

TABLE I. COMPARISON OF WHEEL-HUB MOTOR DEVELOPMENTS

	<i>General Motors</i> [26]	<i>Schaeffler AG</i> [33]	<i>Siemens AG</i> [31]	<i>Fraunhofer</i> [28]	<i>Protean Electric</i> [25]	<i>OvGU Air gap winding</i> [18]	<i>OvGU Combined winding</i> [12]
							
<b>Rim Size [Zoll]</b>	17	16	17	17	18	15	16
<b>Weight [kg]</b>	30	53	50	42	34	20	16
<b>Power [kW]</b>	16	33	63	55	54	40	70
<b>Torque [Nm]</b>	200	350	500	700	650	300	600
<b>Power Density [kW/kg]</b>	0.53	0.62	1.26	1.31	1.59	<b>2</b>	<b>4.375</b>
<b>Torque Density [Nm/kg]</b>	6.67	6.6	10	16.67	19.2	<b>15</b>	<b>37.5</b>

The air gap winding design for a 15-inch wheel-hub motor allows to obtain 40 kW motor power with a very low motor weight of 20 kg providing high power density of near 15 Nm/kg [18]-[22]. The combined winding technology allows to increase these motor properties to 60 kW with a motor weight of 16 kg using lightweight materials [6],[12]. These developments currently have one of the highest gravimetric power and torque densities compared to other developments of electric wheel-hub motors.

Implementation of the air gap winding technology for other mobile applications as e-Scooters, electric gliding boats or windmill generators confirms these advantages [15]. A comparison of the main wheel-hub motors represented by the scientific and industrial space today according to their power properties is presented in the TABLE I. As it can be seen from the table, the proposed technology has the best prospects in terms of the basic requirements for a wheel-hub motor for an electric vehicle.

## 2.2 Air Gap and Combined Winding Design

As it has been mentioned above, the air gap winding design reduces the amount of iron that leads to a smaller motor weight. Very lightweight air gap winding designs offered e.g. by Faulhaber and Maxxon underline this advantage for low-power motors (<200W). The new slotless air gap and combined winding designs patented by Kasper [19] for a 15-inch and 16-inch wheel-hub motors, respectively, which maintain a high torque of near 600 Nm and power of near 70 kW at a very low weight of 16-20 kg are presented in [1]-[22]. Same prototypes of these technologies are shown in Fig. 6. A combination of a very thin (< 5mm) slotless shell between the aluminum stator part and copper wires with a water-cooling system gives the opportunity to generate a high torque with maximum efficiency reducing the motor weight [4],[9]-[22]. The outer rotor with alternating permanent magnets has high number of poles. However, the magnets dimensions are very small that leads also to the weight and costs reduction in comparison to a standard PMSM [18]. The outer rotor is attached to the hub to transmit the electrical torque to a wheel without any gears, belts, shafts, etc. The inner part of the motor includes wheel bearings and a hollow shaft used for power and cooling connections. In addition, the control unit with power electronics can be mounted to the stator inner space providing a very good cooling for power electronic and turning the motor into a portable electric drive. Description of a very efficient automated process to produce air gap windings with a meander structure for external rotors of PMSM shown in Fig. 6 has been published in [14]. Other studies on the manufacturing process of the air gap and combined winding motors, such as calculation and selection of material, temperature studies, acoustics, calculation and valuation of mechanical and electrical losses etc., have been published during the Otto-von-Guericke University research activities in [1]-[22].

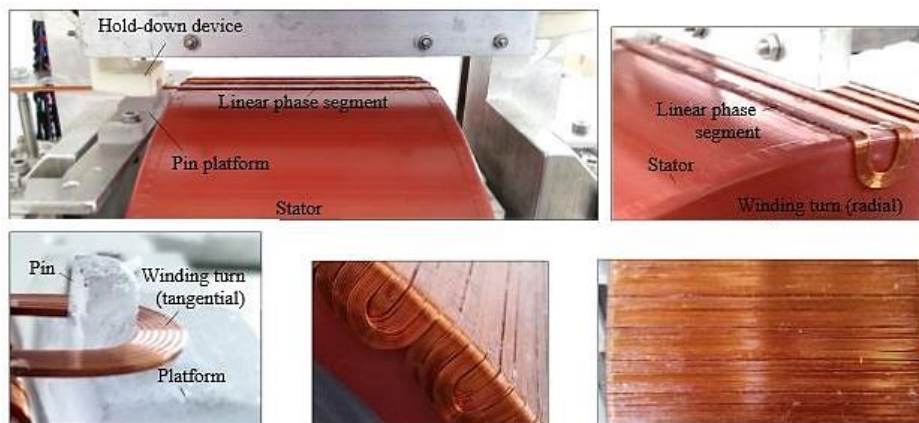


Fig. 6. Production of Air Gap Winding [14].

The difference between the standard PMSM design and the new air gap as well as combined winding technologies can be very clearly demonstrated in Fig. 7. Conspicuously, the air gap winding design reduces a most of the stator back-iron needed for conventional slotted machines increasing the motor torque and power [3]. Moreover, a slotless design prevents any kind of a cogging torque. According to [12], the combination of air gap and additional slot windings comprise advantages of the air gap winding almost doubling the motor power and torque while both motors are operated with the same phase current. A small drawback of the combined winding design compared to a slotless winding is an insignificant

cogging torque. However, it is much less compared to the standard PMSMs and can be reduced by a properly slots filling [12]. The disadvantage of the air gap winding according to [12]-[18] is very low phase inductance of only several  $\mu\text{H}$  due to low number of turns and low iron volume, which makes the motor control a challenge. The combination of air gap and slotted windings allows to increase the phase inductance by one order more. Nevertheless, it does not solve the control problems dramatically.

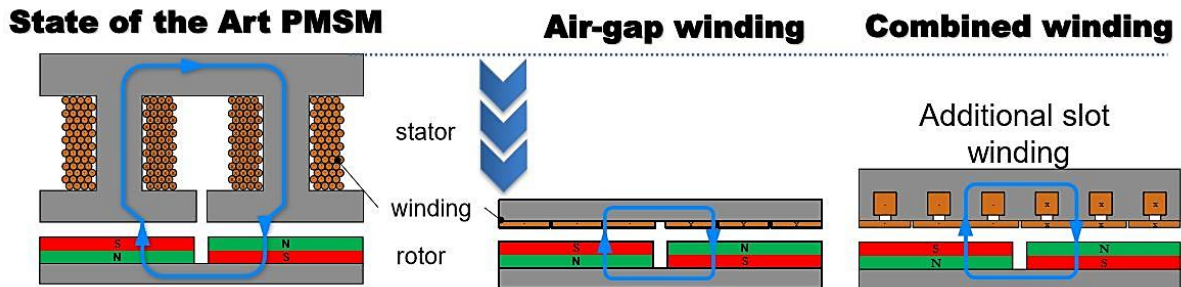


Fig. 7. Comparison of Conventional, Air Gap and Combined Winding Designs for PMSM [3].

The available space in a combined winding wheel hub motor is split between the air-gap winding using the Lorentz force generated by the B-field in the air-gap and slotted winding integrated in the stator back-iron using the B-field in the stator back-iron [12]. Both B-Fields in the air gap and the stator back-iron are driven by the same standard permanent magnets and provide electrical torques added together giving the total electrical torque of the motor. According to [12], both windings operate independently of each other due to a very weakly interaction between the magnetic fields generated by both windings. It leads to simplification of the mathematical model and guarantees that both electrical torques can really be added.

The wheel-hub motor prototypes with the slotted air gap winding design shown in Fig. 5 (right and left above) have been optimized according to [10]-[22] with the conventional radial magnetization principle. In [9], the same optimization approach presented in [13] has been applied to the Halbach array magnetization pattern and compared with the standard radial magnetization. The results presented in [9] shows that the Halbach array magnetization increases the motor torque and power densities, on the one hand, and leads to size and weight reduction due to lack of the rotor back-iron, on the other. A prototype of a wheel-hub motor shown Fig. 5 (left, below) based on the combined winding design with Halbach array magnetization has been constructed and tested in practice in the OvGU. The experimental results have been published in [3]. A comparison of the standard radial magnetization and Halbach array magnetization adapted for air gap and combined winding motor constructions is presented in Fig. 8 (above). The transient FEM simulations presented in [9] and [13] for the vertical magnetic flux density in the air gap for the conventional (below, left) and Halbach array magnetization (below, right) shows the occurrence of additional harmonics in B-Field for both magnetization principles for any air gap high  $h_L$ . It means, that both techniques cannot vanish the additional harmonics of B-Field in the air gap winding that leads to the torque fluctuation, affects the motor efficiency and requires the special control techniques to avoid this problem.



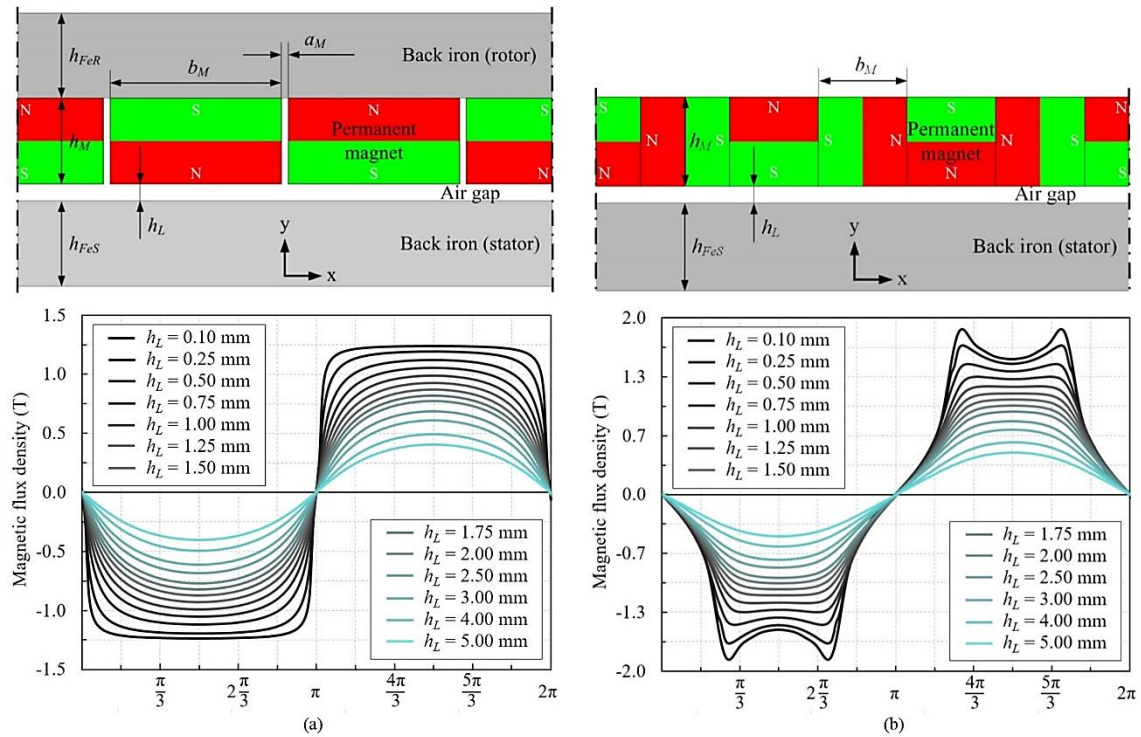


Fig. 8. Comparison of the conventional magnetization (a) and Halbach array magnetization (b) adapted for air gap and combined winding technologies [9].

To sum up, the above presented designs of a slotless air gap winding as well as the combination of air gap and slotted windings for PMSMs can be characterized by the following properties:

- very low phase inductance due to the low stator back-iron volume;
- non-ideal B-Field waveform comprised with additional harmonics;
- high number of poles;
- nearly zero cogging torque for the air gap design and small one for the combined winding;
- very small motor time constant due to the low phase inductance.
- the most part of motor total losses are ohmic losses in the wire due to the low core magnetization and low friction in the mechanical parts.

### 2.3 Problem Statement

The described above properties of permanent magnet synchronous motors with air gap or combined winding require a special control architecture. These motor technologies are based on the PMSM machine, which in an ideal case can be defined by a sinusoidal waveform of back-EMF [46],[47]. However, as it can be seen from Fig. 8, variation of the air gap length leads to a trapezoidal waveform of B-Field that means that the air gap or combined winding motor acquires the properties of a Brushless DC electric motor (BLDC). So, change in the width of the air gap leads to a change in the motor type between PMSM and BLDC. This very interesting feature combined with very low phase inductance and a low motor time constant affords an opportunity to control both motor architectures using the control techniques of PMSM and BLDC presented in Fig. 9. The most promising of them for the air gap or combined motor control will be presented in Chapter 3 in more detail.

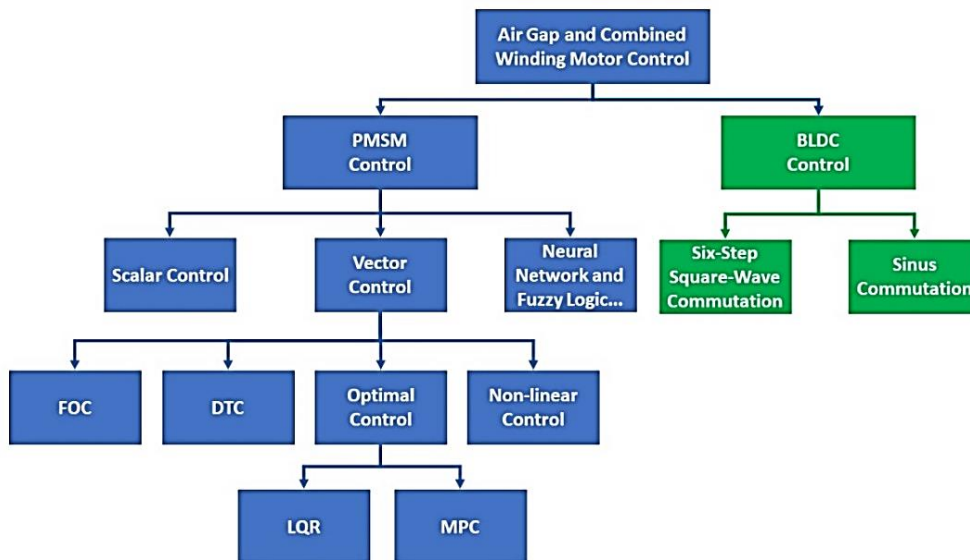


Fig. 9. Classification of different control techniques for PMSM with air gap and combined winding [20],[47].

It should be noted that very low motor inductance in case of using PMSM control methods, such as vector or optimal control, requires a very high switching frequency of power electronic near 100 kHz. However, the power electronic state of the art shows that a new generation of power transistors based on the silicon carbide (SiC) and gallium nitride (GaN) materials makes it possible to implement the motor control on these frequencies [114], [106]. Moreover, BLDC control approach based on the six-step commutation with source current control shows the possibility to control motors without using high switching frequency and reduce the system dynamics. This control method is cheaper, simpler in implementation and can be used in the low- and middle-power mobile applications such as e-Scooters, e-Longboards, etc. However, the motor designs described above are completely new. It means that the PMSM or BLDC control methods already studied and tested in practice must be adapted to new motor types.

Summarizing the above and considering the properties of air gap and combined winding motors, the several requirements for their control algorithms can be distinguished:

- high switching frequency leads to a short calculation interval in the microcontroller that means that the control algorithm should be simple for implementation on the common low-cost microcontroller;
- non-ideal B-Field waveform requires the special approach for compensation of its additional harmonics for torque ripples and motor losses minimization;
- the system dynamics, accuracy and stability should be as high as possible.

From the point of view of a low-frequency control using six-step commutation and source current control by means of the DC-DC converter, the control system should be optimized as much as possible in terms of weight and losses, since its main application is compact vehicles, where dimensions and weight of the electric drive components matter. The problem point in this approach is a DC-DC converter due to presence of coils in it. The method for its optimization will be presented in Chapter 4. The main control method for the air gap and combined winding motor designs is proposed in Chapter 5 and validated in Chapter 6.

### 3. Theoretical Framework of PMSM Control

The main requirements for a high-performance electric drive are ability to offer a precise control, a rapid dynamic response and a steady state response to ensure the system reliability. The control of alternating current machines can be classified into scalar and vector controls. A scalar control is easier to implement in practice, it allows to control multiple motors using one inverter and has a relatively steady-state response. Its biggest drawback is a very low and sluggish dynamics due to lack of a current feedback. To overcome this disadvantage as well as to obtain a steady-state response, it is possible to use a vector control with a closed-loop system. The vector control methods can be divided into field oriented, direct torque, non-linear and predictive or optimal control structures [46],[47]. In addition, due to a very low phase inductance, a PM motor with air gap or combined winding can be set in motion with control methods of a BLDC motor as a six-step commutation control [20]. The fundamental requirements to control of PM motors with an air gap or combined winding are high dynamics, ability to minimize torque ripples and losses taking into account non-ideal B-Field waveforms, absence of complex calculations due to demand in small microcontroller calculation time and stable steady-state response. The mathematical model of a permanent magnet synchronous motor with slotless air gap winding and fundamental PMSM control methods able to satisfy the above listed requirements with their comparison for a very low motor inductance are described in this chapter.

#### 3.1 PM Motor Operation Principle

Building of a mathematical model of PM motors is the first step towards the design and implementation of the control system. This chapter presents the mathematical models of PM motors with slotless air gap winding based on the motor phase currents behavior. In addition, this chapter includes the mathematical model of PMSM losses considering the electromagnetic processes in its elements.

##### 3.1.1 Mathematical Model of PMSM with Air Gap Winding

A dynamic model of a permanent magnets synchronous motor with slotless air gap winding is obtained with consideration of the following conditions [12],[13]:

- the rotor consists of mounted permanent magnets;
- there is no cogging torque due to slotless air gap design;
- harmonic magnetic field density generated by permanent magnets is uniformly distributed over the motor circumference;
- B-field harmonics coefficients are constant and independent from speed and phase currents due to very small current induced magnetic fields;
- the stator has symmetric 3-phase star connected windings and is commutated by a 3-phase inverter (B6 - bridge).

The configuration of a slotless air gap winding PM motor and a 3-phase inverter (B6 bridge) is shown in Fig. 10, where  $R_s$  is a phase resistance,  $L_s, M_s$  are phase self and mutual inductances,  $\underline{e} = [e_a \ e_b \ e_c]^T$  are back-EMFs in three phases,  $\underline{u} = [u_a \ u_b \ u_c]^T$  and  $\underline{i} = [i_a \ i_b \ i_c]^T$  are phase line-to-neutral voltages and currents,  $u_s$  is a voltage in the star point and  $u_{DC}/i_{DC}$  is a supply DC voltage and input current to PMSM B6-bridge [2].

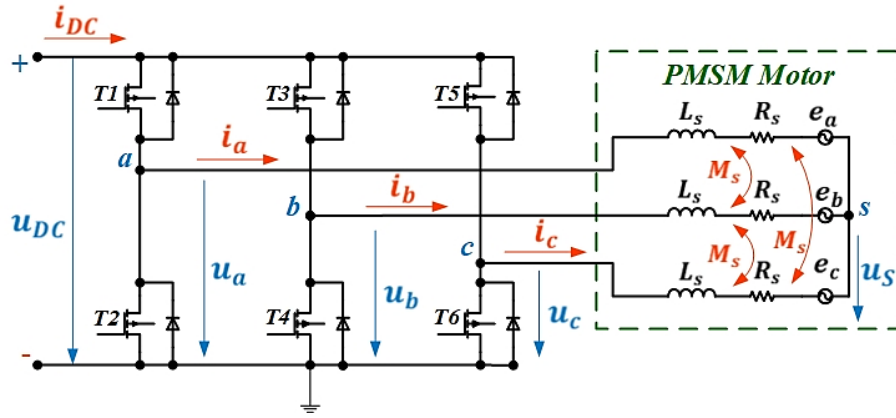


Fig. 10. B6 – Bridge - Fed 3-Phase PMSM Drive Connections [1]-[22].

The mathematical model of a 3-phase PMSM considering Kirchhoff's 1<sup>st</sup> Law

$$i_a + i_b + i_c = 0 \quad (3.1)$$

and Kirchhoff's 2<sup>nd</sup> Law is described by

$$\begin{bmatrix} u_a \\ u_b \\ u_c \end{bmatrix} = \begin{bmatrix} R_s & 0 & 0 \\ 0 & R_s & 0 \\ 0 & 0 & R_s \end{bmatrix} \begin{bmatrix} i_a \\ i_b \\ i_c \end{bmatrix} + \begin{bmatrix} L_s & -M_s & -M_s \\ -M_s & L_s & -M_s \\ -M_s & -M_s & L_s \end{bmatrix} \begin{bmatrix} di_a/dt \\ di_b/dt \\ di_c/dt \end{bmatrix} + \begin{bmatrix} e_a \\ e_b \\ e_c \end{bmatrix} + \begin{bmatrix} 1 \\ 1 \\ 1 \end{bmatrix} u_s, \quad (3.2)$$

$$\underline{u} = \underline{R}_s \underline{i} + \underline{L}_s \frac{d\underline{i}}{dt} + \underline{e} + \underline{u}_s. \quad (3.3)$$

Three phase back-EMF values  $\underline{e}$  calculated by

$$\underline{e} = \omega_M k_M \underline{B}(\varphi_e) \quad (3.4)$$

depend on the mechanical angular velocity  $\omega_M$ , the motor geometric constant  $k_M$  and the averaged B-fields acting on air-gap winding phases  $\underline{B} = [B_a(\varphi_e) \ B_b(\varphi_e) \ B_c(\varphi_e)]^T$  [12],[13],[18]. The three phase B-field  $B_a(\varphi_e)$ ,  $B_b(\varphi_e)$  and  $B_c(\varphi_e)$  are a function of the electrical angle  $\varphi_e$  and depend on harmonic magnetic field density  $B(\varphi_e)$  generated by the permanent magnets as

$$\begin{aligned} B_a(\varphi_e) &= B(\varphi_e) = \sum_k b_k \sin(k \cdot \varphi_e) \\ B_b(\varphi_e) &= B\left(\varphi_e - \frac{2\pi}{3}\right) \\ B_c(\varphi_e) &= B\left(\varphi_e - \frac{4\pi}{3}\right), \end{aligned} \quad (3.5)$$

where  $\underline{b} = [b_1 \ b_2 \ \dots \ b_n]$  is a vector with harmonic coefficients and  $k$  is a coefficient number [12],[13],[18]. An example of a real non-ideal B-field waveform in the air-gap winding as a function of an electric angle and harmonic coefficients  $\underline{b} = [1.15 \ 0.2 \ 0.06 \ 0.01]$  is shown in Fig. 11. According to (3.4), harmonic coefficients  $\underline{b}$  can be obtained with a very good accuracy either based on an FE analysis of the underlying magnetic circuit or based on the approximation of measured back-EMF values [12],[13],[18]. As shown in Fig. 11, non-ideal B-field waveform approximation results in appearance of only odd coefficients.

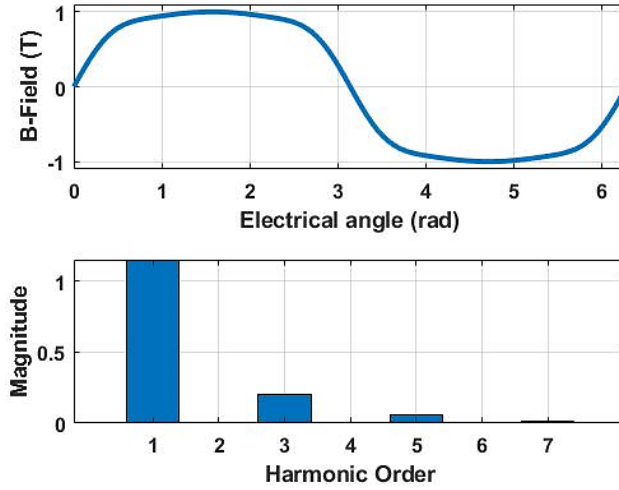


Fig. 11. Top: B-Field in Air-Gap Winding. Bottom: B-Field Harmonic Spectrum with coefficients  $b_k$  [2].

The motor geometric constant  $k_M$  can be found according to the motor geometry as

$$k_M = pl_S r_S, \quad (3.6)$$

where  $p$  is the number of poles,  $l_S$  is the magnet length and  $r_S$  is the winding radius [12],[13],[18]. The motor output torque of air gap winding PM motor

$$T_M = T_E - T_L \quad (3.7)$$

is composed of the electrical torque generated in the air gap winding by Lorentz force

$$T_E = k_M [B_a \quad B_b \quad B_c] \begin{bmatrix} i_a \\ i_b \\ i_c \end{bmatrix} \quad (3.8)$$

and reduced by a loss torque

$$T_L = d \cdot \omega_M + c \cdot \text{sgn}(\omega_M). \quad (3.9)$$

To simplify the mathematical model of the air gap winding PM motor, the linear mechanical friction together with back-iron eddy losses can be combined in the linear friction coefficient  $d$  and mechanical coulomb friction with back-iron hysteresis losses in constant  $c$  [12],[13],[18]. According to (3.9), it can be mentioned that the loss torque depends only on the mechanical speed and is independent on the motor current [12],[13],[18]. Equations (3.1)-(3.9) quite accurately describe the air gap winding motor model in terms of back-EMF, output torque and phase currents based on information of the angular position  $\varphi_e$ , angular velocity  $\omega_M$ , B-field harmonic coefficients  $b_k$  and the motor parameters  $k_M$ ,  $d$ ,  $c$  and can be used for design of the motor control system.

### 3.1.2 Air Gap Winding PM Motor Losses

**Power losses  $P_L$**  are evident as heat occurring during electromechanical conversion and include ohmic losses  $P_\Omega$ , eddy current losses  $P_W$ , hysteresis losses  $P_H$  and losses caused by friction  $P_F$  [5],[12],[18]

$$P_L = P_\Omega + P_H + P_W + P_F. \quad (3.10)$$

**Ohmic loss  $P_\Omega$** , according to Joule's law, is proportional to the electrical power in the conductor and its phase resistance [5],[12],[13],[18]

$$P_{\Omega} = \frac{R_s}{2\pi} \int_0^{2\pi} (i_a^2(\varphi_e) + i_b^2(\varphi_e) + i_c^2(\varphi_e)) d\varphi_e. \quad (3.11)$$

Phase resistance is not constant and dependent on phase temperature, current and switching frequency caused by skin effect. However, the slotless technology is predicated on using a small wire diameter, which makes skin effect insignificant [5],[12],[13],[18]. After all, when required, these features can be included in the mathematical model of the ohmic loss as

$$R_s(\vartheta) = \frac{\rho_{20^0}}{S_R} l_R (1 + \alpha_{20^0}(\vartheta - \vartheta_{20^0}))$$

$$\delta = (\pi f_e \mu_r \mu_0 \sigma)^{-1/2} \quad (3.12)$$

where  $\vartheta$  is the operating temperature of motor phases,  $\rho_{20^0} = 1/\sigma_{20^0}$  is the resistivity measured at  $\vartheta_{20^0} = 20^{\circ}C$ ,  $\alpha_{20^0}$  is the temperature coefficient at  $20^{\circ}C$ ,  $\mu_r \mu_0$  is a relative and free space permeability,  $\sigma$  is the electrical conductivity of the material,  $l_R$  is the phase length and  $S_R$  is the cross – section of the conductor reduced to the skin depth  $\delta_{sd}$ . The skin depth becomes smaller for large wires sections or in case of higher supply frequencies  $f_e$  [5], [12],[13],[18].

**Hysteresis loss  $P_H$**  can be determined from the magnetization curve of the stator stack. The magnetic energy density is composed of the magnetic field strength  $H$  in  $[A/m]$  integrated over the magnetic flux density [18]. This area within the hysteresis loop is smaller or larger depending on the type of material. In addition, the area of magnetic energy can change its shape depending on the re-magnetisation frequency  $f_{rm}$  in  $[Hz]$ . According to [5],[18] and [94], the hysteresis power loss is proportional to the frequency of re-magnetisation multiplied by the magnetic energy density and volume  $V_M$  of the magnetic material

$$P_H = V_M f_{rm} \int_B H dB \approx x_m f_{rm} \hat{B}, \quad (3.13)$$

where  $x_m$  is material-specific constant and  $\hat{B}$  is amplitude of the magnetic flux density.

**Eddy current loss  $P_W$**  according to [5],[18],[94] is proportional to the square of the angular velocity

$$P_W = \omega_M^2 \frac{N_{Dr} \sigma l_S}{12} (b_w h_w^3 B_{t,eff}^2 + h_w b_w^3 B_{r,eff}^2), \quad (3.14)$$

where  $b_w$  and  $h_w$  are width and height of the single wire,  $B_{t,eff}$  and  $B_{r,eff}$  are the root mean square of the derivative of the tangential and radial flux,  $N_{Dr}$  is the number of single wires. It can be mentioned, that the re-magnetisation frequency is equal to the electrical or commutation frequency  $f_e$  and depends on number of poles  $p$  of the motor and the mechanical angular velocity  $\omega_M$

$$f_{rm} = f_e = \frac{p \omega_M}{2} = \frac{\omega_e}{2\pi} \quad (3.15)$$

or the electrical angular velocity  $\omega_e = p \omega_M$ , which underlines that the both iron losses in a greater degree are conditioned by the motor speed.

**Friction losses  $P_F$**  are a consequence of speed-dependent bearing and air frictions. The bearing friction depends on the bearing type, rotor speed, occurring load on a bearing, properties of the lubricant and the external environmental influences [18]. Bearing friction losses can be calculated based on the guidelines proposed by bearing manufactures. As follows according to SKF, bearing friction loss is a sum of rolling friction losses, stiction losses and frictional loss in contact seals as

$$P_{F,bearing} = \omega_M (\Phi_{ish} \Phi_{rs} F_{rr} \left( \frac{60\vartheta_b}{2\pi} \omega_M \right)^{0.6} + F_{sl} \mu_{sl} + T_{seal}) \quad (3.16)$$

where  $\mu_{sl}$  is a sliding friction coefficient,  $F_{sl}$  and  $F_{rr}$  are factors of geometry and radial and axial forces,  $\Phi_{ish}$  and  $\Phi_{rs}$  lubricant displacement and film thickness factors,  $\vartheta_b$  is viscosity and  $T_{seal}$  is a frictional torque of contact seals [10],[11]. The air friction is relatively low compared to the bearing friction and depends on the rotor speed and on the resistance surface of the electrical machine [18]. The air friction losses can be calculated with Saari equation which represents the power associates with the resisting drag torque of the rotating cylinder

$$P_{F,w} = 0.4\omega_M^3 \Theta_M K_{ball} D_b^5, \quad (3.17)$$

where  $K_{ball}$  is the rolling element coefficient,  $\Theta_M$  is the oil bath resistance variable,  $D_b$  is the mean bearing diameter [10],[11]. Nevertheless, these loss components are very small and usually can be neglected [18].

Based on the experimental and simulation results presented in [13], it is possible to make the following assumptions: eddy current and linear friction losses of a PMSM with air gap winding have a quadratic dependence on the angular speed and can be included in constants  $d$ ; hysteresis and mechanical coulomb friction losses are almost proportional to the angular speed and can be combined in constants  $c$ . It can be summarized that the averaged total motor losses consist of ohmic and non-ohmic losses

$$P_L = \frac{1}{2\pi} \int_0^{2\pi} (R_s(i_a^2(\varphi_e) + i_b^2(\varphi_e) + i_c^2(\varphi_e)) + d \bar{\omega}_M^2 + c \bar{\omega}_M) d\varphi_e, \quad (3.18)$$

where non-ohmic losses depend only on the average angular speed in a pole pair segment [13]

$$\bar{\omega}_M = \int_0^{2\pi} \omega_M d\varphi_e \quad \text{and} \quad \bar{\omega}_M^2 = \int_0^{2\pi} \omega_M^2 d\varphi_e. \quad (3.19)$$

The motor losses affect the efficiency of the system and generally describe the quotient between total electrical power  $P_E$  and useful mechanical power  $P_M$ . The motor efficiency  $\eta_M$  can be estimated from [13], as

$$\eta_M = \frac{P_M}{P_E} = \frac{P_M}{P_M + P_L} = \frac{\omega_M T_M}{\omega_M T_M + P_L}. \quad (3.20)$$

Equation (3.18) affords an opportunity to develop a control system able to implement the required motor operations with minimization of total losses and in the same time with maximization of the motor efficiency. This method will be presented in Chapter 5.

## 3.2 Space Vector PWM

The Pulse Width Modulation (PWM) has gained wide popularity in the control of the power electronic devices as DC-DC or DC-AC converters. The several schemes of PWM have been suggested in the references [46],[47]. The PWM technique combined with DC-DC converters makes it possible to reduce or increase the output DC voltage or current by variation of the pulse width. On the other hand, applying PWM in DC-AC converters allows to create an AC waveform of output voltage with variable frequency that is mostly used in synchronous or asynchronous motor control. The main operating principle of the pulse width modulation in DC-AC converters is to modulate the duration of the switching signals supplying the transistors in order to achieve the required output voltage, current or power as a function of frequency considering the criteria of the equal area [46],[47]. Representation of PWM combined with

Space Vector (SVPWM) allows to achieve the optimal AC motor behaviors with a minimal loss. This Chapter introduces the fundamental concepts of PWM as well as SVPWM theory that will be used in development of the control system for air gap and combined winding PM motors. Space Vector PWM (SVPWM) algorithm is based on the representation of DC-AC converter output as eight space vectors. Thus, three-phase reference voltages can be simultaneously represented as one rotating vector by means of SVPWM, accordingly, each phase is not switched separately. The main advantages of SVPWM are less total harmonic distortion, grater power factor and less switching losses in comparison to the sinusoidal PWM [46],[47]. The rotating space vector  $V_{Ref}$  with electrical speed  $\omega_e$  can be defined from three phase reference voltages

$$V_{Ref} = \frac{2}{3} \left( v_{am} + v_{bm} e^{j\frac{2\pi}{3}} + v_{cm} e^{j\frac{4\pi}{3}} \right), \quad (3.21)$$

where  $\underline{v}_m = [v_{am} \ v_{bm} \ v_{cm}]^T$  are modulating signals. Considering, that converter has only two states  $u_{DC}$  or 0, the total possible switching configuration are  $2^3 = 8$ , as shown in TABLE I, where 0 means that the corresponding switching signal of high transistors  $\underline{S}_{high} = [S_1 \ S_3 \ S_5]^T$  is OFF and 1 indicates that  $\underline{S}_{high}$  is ON. In addition, the phase voltages  $\underline{u}$  can be estimated according to the eight space vectors and eight switching states as shown in TABLE II. Six active switching states  $V_1 \dots V_6$  are shown graphically in Fig. 12 (left), where zero state vectors  $V_7$  and  $V_8$  mean that all upper transistors are closed and open respectively [46],[47].

TABLE II. PHASE VOLTAGE ACCORDING TO SWITCHING STATE [46],[47]

Switching state	Switches on	Space vector	Phase-to-neutral Voltage Space Vectors
1	1,4,6	$V_1(100)$	$2/3 \cdot u_{DC} e^{j0}$
2	1,3,6	$V_2(110)$	$2/3 \cdot u_{DC} e^{j\frac{\pi}{3}}$
3	2,3,6	$V_3(010)$	$2/3 \cdot u_{DC} e^{j\frac{2\pi}{3}}$
4	2,3,5	$V_4(011)$	$2/3 \cdot u_{DC} e^{j\pi}$
5	2,4,5	$V_5(001)$	$2/3 \cdot u_{DC} e^{j\frac{4\pi}{3}}$
6	1,4,5	$V_6(101)$	$2/3 \cdot u_{DC} e^{j\frac{5\pi}{3}}$
7	2,4,6	$V_7(000)$	0
8	1,3,5	$V_8(111)$	0

Combination of six active space vectors  $V_1$  to  $V_6$  form a hexagon divided into 6 sectors of  $60^\circ$  degrees in accordance with the electric angle  $\varphi_e$ . The sector identification logic in comparison to  $\varphi_e$  is shown in Fig. 12 (right).



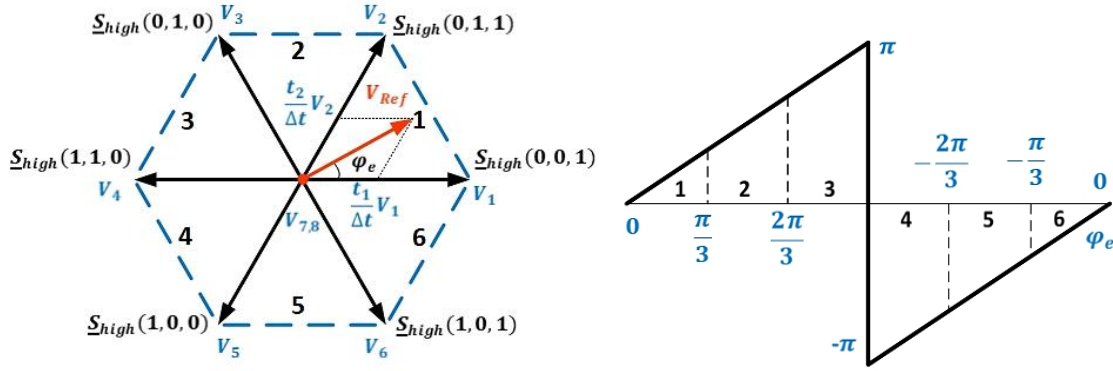


Fig. 12. Left: Principle of SVPWM; Right: Hexagon Sector Identification Logic.

The product of the reference voltage  $V_{Ref}$  and the sampling time  $\Delta t = 1/f_{PWM}$  must be equal to the product of the applied phase-to-neutral voltage space vectors presented in TABLE II. and their duration times  $t_1$ ,  $t_2$  and  $t_0$ , considering that the reference voltage during the switching interval does not change its value. For example, for the first sector, the reference voltage can be found using

$$V_{Ref}\Delta t = V_1 t_1 + V_2 t_2 + V_7 t_0, \quad (3.22)$$

where  $V_1$ ,  $V_2$  and  $V_7$  are the active vectors of the first sector and  $\Delta t = t_1 + t_2 + t_0$ . Thus, the time durations of each active sector can be found as

$$\begin{aligned} t_1 &= \frac{\sqrt{3}|V_{Ref}|\Delta t}{u_{DC}} \sin \left( \text{Sector} \frac{\pi}{3} - \varphi_e \right) \\ t_2 &= \frac{\sqrt{3}|V_{Ref}|\Delta t}{u_{DC}} \sin \left( \varphi_e - (\text{Sector} - 1) \frac{\pi}{3} \right) \\ t_0 &= \Delta t - t_1 - t_2. \end{aligned} \quad (3.23)$$

Thus, the switching time of high transistors  $\underline{St}_{high} = [St_1 \quad St_3 \quad St_5]^T$  can be estimated according to the each active sector with given duration times as described in the TABLE III.

TABLE III. SWITCHING TIME ESTIMATION FOR EACH SECTOR [46],[47]

Switching time	Sector 1	Sector 2	Sector 3	Sector 4	Sector 5	Sector 6
$St_1$	$t_1 + t_2 + 0.5t_0$	$t_1 + 0.5t_0$	$0.5t_0$	$0.5t_0$	$t_2 + 0.5t_0$	$t_1 + t_2 + 0.5t_0$
$St_3$	$t_2 + 0.5t_0$	$t_1 + t_2 + 0.5t_0$	$t_1 + t_2 + 0.5t_0$	$t_1 + 0.5t_0$	$0.5t_0$	$0.5t_0$
$St_5$	$0.5t_0$	$0.5t_0$	$t_2 + 0.5t_0$	$t_1 + t_2 + 0.5t_0$	$t_1 + t_2 + 0.5t_0$	$t_1 + 0.5t_0$

The duty cycle ratio  $\underline{d}_{PWM} = [d_{PWM,a} \quad d_{PWM,b} \quad d_{PWM,c}]^T$  is within the range from 0 to 1 or from -1 to 1 and shows how long transistors are open in comparison to the sampling time and can be defined as

$$\underline{d}_{PWM} = \frac{\underline{St}_{high}}{\Delta t}. \quad (3.24)$$

Transistor switching signals  $\underline{S} = [S_1 \quad \dots \quad S_6]^T$  can be generated by comparison of three-phase duty cycle ratio  $\underline{d}_{PWM}$  with a triangular wave  $v_c$  used for all three phases and operated with a high switching frequency. The amplitude of the triangular carrier wave is equal to one. Thus, as shown in Fig. 13, the upper switches (T1, T3 and T5) operated by control signals  $\underline{S}_{high} = [S_1 \quad S_3 \quad S_5]^T$  is ON, when the

duty cycle ratio  $d_{PWM}$  is greater than value of  $v_m$  and vice versa. The control signals  $\underline{S}_{Low} = [S_2 \ S_4 \ S_6]^T$  of lower transistors (T2, T4 and T6) are described with complement operation of the upper transistors, respectively. It is important to note that in order to eliminate a short circuit, a short dead band should be maintained between the switching OFF of  $\underline{S}_{high}$  and switching ON of  $\underline{S}_{Low}$  and vice versa [46],[47]. A similar operation principle can be applied to the pulse modulation approach for a DC-DC converter considering the DC waveform of the modulation signal [46],[47]. The full calculation process of SVPWM is illustrated in Fig. 13 with the modulation ratio  $f_{PWM}/f_e$  equal to 10 and with a modulation signal 25% less than the supply voltage for better presentation. In practice, for an air gap or combined winding PM motor, this ratio will be much higher.

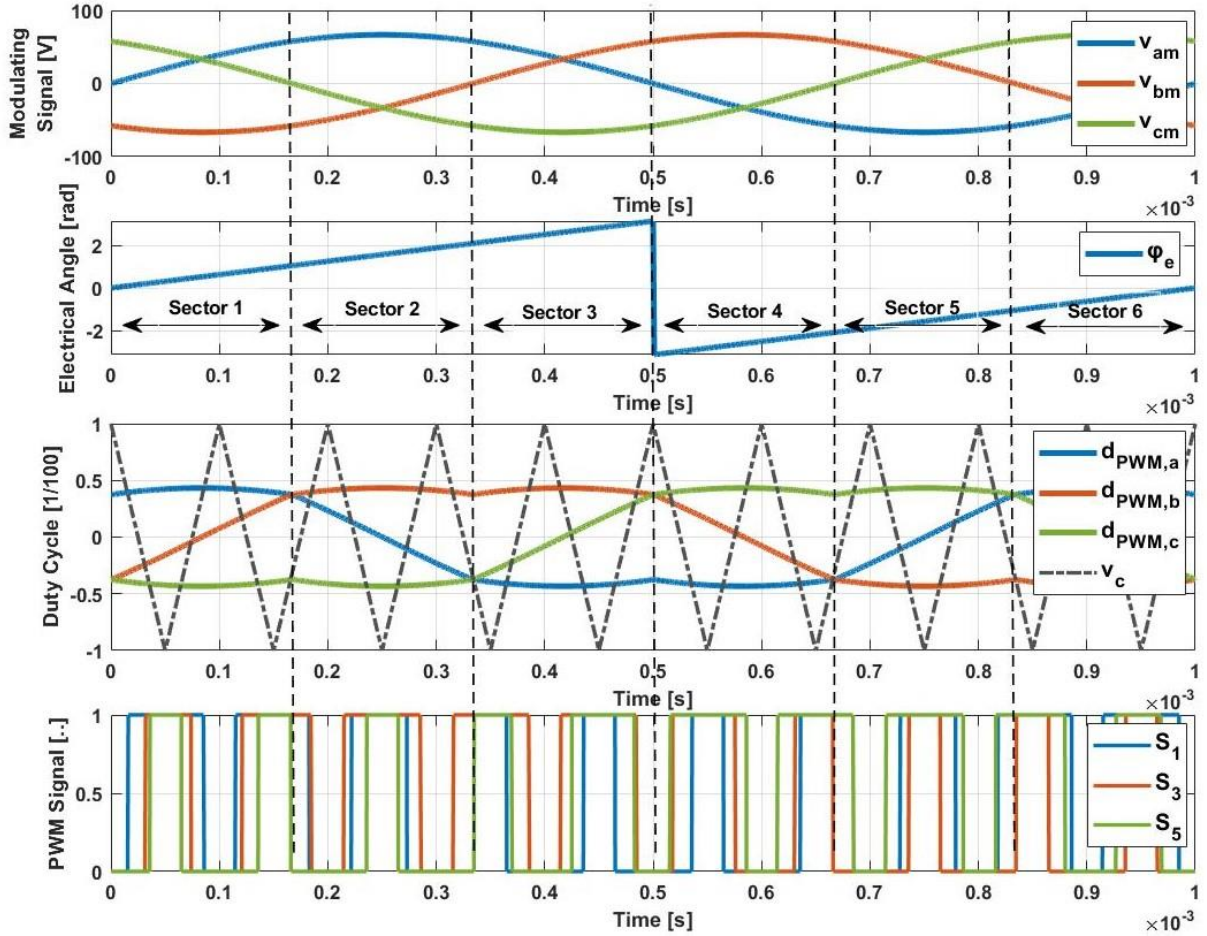


Fig. 13. SVPWM of a Three-Phase DC-AC Converter.

As it can be seen from the figure, the pulse width can be changed by means of a triangular carrier signal. As a result, a positive DC link voltage is generated when the reference signal is above the carrier signal. For a negative DC link voltage, it is the other way around.

### 3.3 Scalar Based Motor Control

Scalar based open-loop control (SBC) methods are classified on V/f schemes and I/f schemes. SBC can be used in drive systems where main conditions are simplicity, low cost and reduced dynamic performance is acceptable. For example, a typical use of such systems are pump or fan drives [46],[47].

The general application of PMSM with air gap or combined winding is e-Mobility that requires a high dynamic behavior. However, for some kinds of low power e-Bikes or e-Longboards, where the control accuracy matters less than costs, these methods can be used. At the same time, performance of open-loop methods often depends on the load conditions and the motor parameters that leads to the power swings and motor asynchronies. In addition, selection of controller parameters cannot be performed with the necessary accuracy [15].

The main idea of V/f control according to [39]-[47] is based on the definition that the supply frequency of the stator depends on the speed of the rotor. It can be described by considering (3.2) under the assumptions that the stator flux linkage is constant, and the voltage drop across the stator resistance can be neglected

$$\underline{u} \simeq j\omega_e \underline{\psi} \rightarrow |\hat{\psi}| \simeq \frac{|\hat{u}|}{2\pi f_e}, \quad (3.25)$$

where  $\underline{\psi}$  is the space vector of the stator flux produced by the stator current and the permanent magnets of the rotor,  $|\hat{\psi}|$  and  $|\hat{u}|$  are the magnitudes of the flux linkage vector and the voltage vector, respectively. Thus, according to (3.25) the reference supply of the inverter is based on the direct relationship between the stator voltage and the electrical frequency, which, in turn, is used to determine the position of the stator flux. The stator flux linkage should be maintained around its nominal level equal to the rated stator voltage and the rotor speed [39]. The open-loop V/f controller accelerates motor to a desired speed by supplying a PMSM with a voltage and frequency according to (3.25). Due to no feedback, the voltage magnitude  $|\hat{u}|$  is predetermined. According to [39]-[47], the following Fig. 14 illustrates the scalar control concept. As it can be seen, the control system consists of three areas.

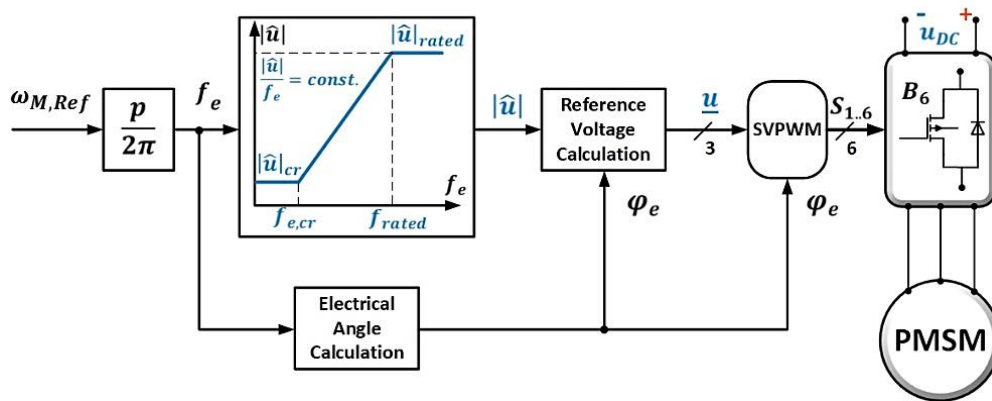


Fig. 14. Open-Loop Block Diagram of Volt per Herz Control of PMSM.

The first range is the actual speed control and generation of a frequency reference ramp with a desired slope of acceleration, considering the stability requirements of the system. A reference angular velocity is formed by the manipulated variable of the speed controller. As it already has been mentioned, the voltage-frequency characteristic curve is used to determine the actuating voltage and the electrical angle by observing a constant magnetic flux. In case if the frequency is less than the critical value, the voltage should be increased. In case, when the reference frequency is higher than the critical value  $f_{e,cr}$ , the voltage amplitude can be calculated according to

$$|\hat{u}| = \frac{|\hat{u}|_{rated} - |\hat{u}|_{cr}}{f_{rated} - f_{e,cr}} f_e, \quad (3.26)$$

where  $|\hat{u}|_{rated}$  is the peak value of the equivalent rated stator voltage,  $f_{rated}$  is the rated frequency and  $|\hat{u}|_{cr}$  is the voltage amplitude at the critical frequency. It has been the second step. The third step is calculation of three reference voltages in sinusoidal waveform and determination of the turn-on times using the space vector modulation for the transistors of the inverter. It should be added that in SBC speed drive systems, the PWM frequency  $f_{PWM}$  should be variable and synchronized with the modulation frequency  $f_e$  [46]. The motor start point is determined by its asynchronous state with the supplied magnetic field. That's why, during PMSM startup, the motor attempts to achieve synchronization with the field, which can lead to unsuccessful motor operation in case of high values of the applied frequency. In order to avoid this problem, the reference frequency should be very low at the start point and rise very slow to its steady-state value. This leads to very low engine dynamics. In the same time, high values of the V/f ratio lead to a case, when a motor becomes overexcited. On the other hand, a low V/f ratio can be associated with under-excitation [39]-[47]. The both states are strictly undesirable and resulted in a rise of power losses and degreasing of torque.

To summarize, it can be mentioned, that scalar control for motors with sufficiently low inductance would exhibit inadequate dynamic behavior. In addition, this control does not allow a direct current control. Ultimately, the control applies to low dynamic requirements where the speed changes slowly. The most important advantages of this method are its low cost, simplicity, the ability to control multiple motors using one inverter and absence of current, speed and position feedback, which eliminates the need for sensors and gives the possibility to create a compact system. On the negative side, the open-loop structure is based on rough approximations, which leads to a nonstable motor operation in some points. In addition, very low PMSM inductance needs a high switching frequency of B6 bridge, which increases costs and makes scalar method ineffective for PMSM with low inductance and high power. In [39]-[42] for V/f systems and in [43]-[45] for I/f schemes, closed-loop solutions have been described using a current and speed feedback and power factor estimation to overcome the above listed disadvantages of scalar control methods. However, they cannot fully satisfy all requirements to a control system of PMSM with very low inductance and high power described in Chapter 2. This requires applying more sophisticated methods, which will be described below.

### 3.4 Vector Control

Field Oriented Control (FOC), Direct Torque Control (DTC), Non-Linear Control (NLC) and Optimal Control methods as Model Predictive Control (MPC) or Linear Quadratic Regulator (LQR) are founded on the Space Vector Representation of motor mathematical model and can be used for synchronous or asynchronous motors. Due to the current and speed feedback, these methods are determined by high dynamics and stability. On the other hand, low phase inductance of an air gap or combined winding PMSM requires a high switching frequency to hold the current and torque ripples in the acceptable range. This fact with necessity for accurate feedback measurements can result in high system costs. However, a new type of transistors as GaN or SiC allows to apply these methods for high-power PMSMs with very low phase inductance. According to [1]-[22], the mathematical model of air gap or combined winding motors is nearly ideal linear due to very low changes in the phase inductance, B-Field or resistance behaviors. Thus, the NLC control can be excluded from the list of possible low inductance PMSM vector control options. If necessary, in cases when the behavior of the motor ceases to be linear, this method can also be applied.

### 3.4.1 Space Vector Representation

The adoption of vector-based approaches makes it possible to simplify the analysis of a three-phase machine system into two orthogonal components  $dq$  using the Park and Clarke transformations. Space vector representation can be applied to control systems of permanent magnet synchronous or asynchronous motors. This section will describe the main principles of space vector approaches presented in [46]-[80] based on the mathematical model of PMSM with air gap or combined winding. The current flowing in the motor winding generates a magnetic motive force MMF according to Ampere's law. In case of a three-phase system, the MMF is align with their own magnetic field and produced by each phase currents separated by  $120^\circ$  electric degrees from each other. Using (3.1), it can be assumed that  $\underline{i}$  is balanced and can be described with the electrical frequency, amplitude  $I_s$ , initial electrical angle  $\varphi_{e,0}$  in the function of time  $t$  as [46]

$$\begin{aligned} i_a(t) &= I_s \sin(\omega_e t + \varphi_{e,0}) \\ i_b(t) &= I_s \sin(\omega_e t + \varphi_{e,0} - 2\pi/3) \\ i_c(t) &= I_s \sin(\omega_e t + \varphi_{e,0} - 4\pi/3). \end{aligned} \quad (3.27)$$

Thus, the space vectors for three-phase current, voltage and magnetic flux can be written as [46]

$$\begin{aligned} \bar{i}_s &= \frac{2}{3} \left( i_a(t) + i_b(t)e^{j\frac{2\pi}{3}} + i_c(t)e^{j\frac{4\pi}{3}} \right) = I_s e^{j(\omega_e t + \varphi_{e,0})} \\ \bar{u}_s &= \frac{2}{3} \left( u_a(t) + u_b(t)e^{j\frac{2\pi}{3}} + u_c(t)e^{j\frac{4\pi}{3}} \right) = R_s \bar{i}_s + \frac{d\bar{\psi}_s}{dt} \\ \bar{\psi}_s &= (L_s + M_s) \bar{i}_s + \psi_m e^{j\varphi_e} \end{aligned} \quad (3.28)$$

where  $\psi_m$  is a constant flux amplitude induced by the permanent magnets. The magnetic flux  $\psi_M$  can be found according to the motor geometry and B-Field integrated over the stator surface  $A_S$  [12],[18]

$$\psi_M = p \int B(\varphi_e) dA_S. \quad (3.29)$$

The fundamental equation that describes the relationship between the voltage and current in a space vector form can be obtained by replacing the flux derivative with the calculated derivative of flux as

$$\bar{u}_s = R_s \bar{i}_s + (L_s + M_s) \frac{d\bar{i}_s}{dt} + j\omega_e \psi_m e^{j\varphi_e} \quad (3.30)$$

Equations (3.28) and (3.30) show that the space vectors of three-phase voltages, currents and flux are three vectors in the complex plane rotating with frequency  $\omega_e$ . It leads to the idea that each vector could be decomposed into a real axis  $\alpha$  and a quadrature component on imaginary axis  $\beta$  shown as a complex plane in Fig. 15. Moreover, the same decomposition can be carried out with respect to  $dq$  reference frame and then used to investigation of the motor control strategies [46],[47].

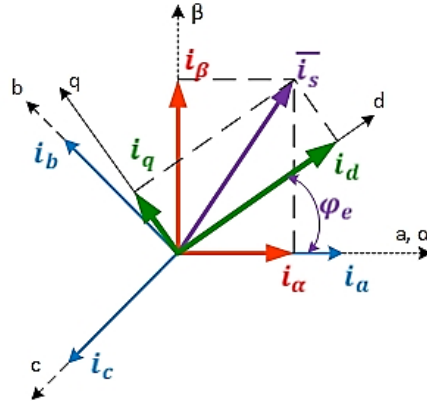


Fig. 15. Illustration of Stationary  $\alpha\beta$  and Synchronous  $dq$  Reference Frames.

**Representation in Stationary Reference ( $\alpha - \beta$ ) Frame** is premised on projecting the space vectors of voltages and current onto real  $\alpha$  and imaginary  $\beta$  axes. The real axis is aligned with the peak of MMF. The imaginary axis is aligned in quadrature to a real axis. The stator currents and voltages can be represented by the complex notations as

$$\begin{aligned}\bar{i}_s &= i_\alpha + ji_\beta \\ \bar{u}_s &= u_\alpha + ju_\beta.\end{aligned}\quad (3.31)$$

Substituting (3.31) into (3.30) gives the model of PMSM in the ( $\alpha - \beta$ ) reference frame as

$$\begin{aligned}u_\alpha &= R_s i_\alpha + (L_s + M_s) \frac{di_\alpha}{dt} - \omega_e \psi_m \sin(\varphi_e) = R_s i_\alpha + \frac{d\psi_\alpha}{dt} \\ u_\beta &= R_s i_\beta + (L_s + M_s) \frac{di_\beta}{dt} + \omega_e \psi_m \cos(\varphi_e) = R_s i_\beta + \frac{d\psi_\beta}{dt}.\end{aligned}\quad (3.32)$$

Projecting phase currents  $i_a$ ,  $i_b$  and  $i_c$  on  $\alpha\beta$  axes give current components in the  $\alpha - \beta$  reference frame and can be achieved by the Clarke and the inverse Clarke transformations

$$\begin{bmatrix} i_\alpha \\ i_\beta \\ i_0 \end{bmatrix} = \frac{2}{3} \begin{bmatrix} 1 & -\frac{1}{2} & -\frac{1}{2} \\ 0 & \frac{\sqrt{3}}{2} & -\frac{\sqrt{3}}{2} \\ \frac{1}{2} & \frac{1}{2} & \frac{1}{2} \end{bmatrix} \begin{bmatrix} i_a \\ i_b \\ i_c \end{bmatrix} \quad \text{and} \quad \begin{bmatrix} i_a \\ i_b \\ i_c \end{bmatrix} = \begin{bmatrix} 1 & 0 & 1 \\ -\frac{1}{2} & \frac{\sqrt{3}}{2} & 1 \\ -\frac{1}{2} & -\frac{\sqrt{3}}{2} & 1 \end{bmatrix} \begin{bmatrix} i_\alpha \\ i_\beta \\ i_0 \end{bmatrix}.\quad (3.33)$$

The real  $\alpha$  axis preferentially is aligned with the direction of  $i_a$  current and the direction of peak magnetic motive force. The energy conservation is expressed in the coefficient  $2/3$ . Zero current  $i_0$  represents the zero balance of three phase currents according to (3.1). Equations (3.31) - (3.33) underline the sinusoidal waveform of currents and voltages in  $\alpha - \beta$  reference due to their direct relationship with original frames (3.27). The stator flux amplitude  $\psi_s$  in  $\alpha - \beta$  reference frame and components of the stator flux linkage can be estimated via

$$\begin{aligned}\psi_\alpha &= \int_0^t (u_\alpha - R_s i_\alpha) dt + \psi_{\alpha|t=0} \\ \psi_\beta &= \int_0^t (u_\beta - R_s i_\beta) dt + \psi_{\beta|t=0} \\ \psi_s &= \sqrt{\psi_\alpha^2 + \psi_\beta^2},\end{aligned}\quad (3.34)$$

where  $\psi_{\alpha,\beta}|_{t=0}$  are the initial components of the stator flux linkage. The electromagnetic torque can be calculated as

$$T_E = \frac{3}{2}p(\psi_\alpha i_\beta - \psi_\beta i_\alpha). \quad (3.35)$$

The torque equation (3.35) gives the possibility to motor torque estimation, when the  $i_\alpha$  and  $i_\beta$  are given. However, in case, if a reference electromagnetic torque is given, it would be difficult to calculate these currents in reverse. Thus, this torque estimation can be used only in direct torque control systems, where there is no need in calculation of  $\alpha - \beta$  current references. The synchronous reference equations are more often used, because there is a simple relation between the electromagnetic torque and  $i_q$  current[46],[47]. However,  $\alpha - \beta$  transformations are based on simple equations and doesn't require the electric angle that makes it possible to build systems without a speed and rotor position sensors.

**Representation in Synchronous Reference ( $d - q$ ) Frame** is based on the clockwise rotating of a space vector in  $\alpha - \beta$  reference frame by  $\varphi_e$  as shown in Fig. 15 [46],[47]. The direct axis  $d$  is align with a rotating flux produced by the permanent magnets. The axis  $q$  is in quadrature to axis  $d$ . This rotation can be expressed mathematically with multiplication of space vectors  $\bar{i}_s$  and  $\bar{u}_s$  by the factor  $e^{-j\varphi_e}$ , which sets a synchronous  $d - q$  reference frame space vectors  $\bar{i}_s'$  and  $\bar{u}_s'$  as

$$\begin{aligned} \bar{i}_s' &= \bar{i}_s e^{-j\varphi_e} = i_d + j i_q \\ \bar{u}_s' &= \bar{u}_s e^{-j\varphi_e} = u_d + j u_q. \end{aligned} \quad (3.36)$$

Similarly with  $\alpha - \beta$  reference frame, multiplying (3.30) by  $e^{-j\varphi_e}$  governs to the fundamental equation

$$\bar{u}_s' = R_s \bar{i}_s' + (L_s + M_s) \frac{d\bar{i}_s'}{dt} + j\omega_e (L_s + M_s) \bar{i}_s' + j\omega_e \psi_m, \quad (3.37)$$

that leads to the relationship between the voltage and current variables and describes the motor dynamic model in the  $d - q$  reference frame. Substituting (3.36) into (3.37) leads to the  $d - q$  mathematical model of PMSM as

$$\begin{aligned} u_d &= R_s i_d + (L_s + M_s) \frac{di_d}{dt} - \omega_e (L_s + M_s) i_q \\ u_q &= R_s i_q + (L_s + M_s) \frac{di_q}{dt} + \omega_e (L_s + M_s) i_d + \omega_e \psi_m, \end{aligned} \quad (3.38)$$

where  $u_d$  includes the real part components, and  $u_q$  is imaginary part. The relationship between the space vector representations of currents and voltages in the  $\alpha - \beta$  reference frame and those in the  $d - q$  reference frame can be achieved by Park and inverse Park transformations as

$$\begin{aligned} \begin{bmatrix} i_d \\ i_q \end{bmatrix} &= \begin{bmatrix} \cos(\varphi_e) & \sin(\varphi_e) \\ -\sin(\varphi_e) & \cos(\varphi_e) \end{bmatrix} \begin{bmatrix} i_\alpha \\ i_\beta \end{bmatrix} \quad \text{and} \quad \begin{bmatrix} i_\alpha \\ i_\beta \end{bmatrix} = \begin{bmatrix} \cos(\varphi_e) & -\sin(\varphi_e) \\ \sin(\varphi_e) & \cos(\varphi_e) \end{bmatrix} \begin{bmatrix} i_d \\ i_q \end{bmatrix} \\ \begin{bmatrix} u_d \\ u_q \end{bmatrix} &= \begin{bmatrix} \cos(\varphi_e) & \sin(\varphi_e) \\ -\sin(\varphi_e) & \cos(\varphi_e) \end{bmatrix} \begin{bmatrix} u_\alpha \\ u_\beta \end{bmatrix} \quad \text{and} \quad \begin{bmatrix} u_\alpha \\ u_\beta \end{bmatrix} = \begin{bmatrix} \cos(\varphi_e) & \sin(\varphi_e) \\ -\sin(\varphi_e) & \cos(\varphi_e) \end{bmatrix} \begin{bmatrix} u_d \\ u_q \end{bmatrix}. \end{aligned} \quad (3.39)$$

The combination of Clarke and Park transformations leads to the Park-Clarke transformation from three-phase values to the  $d - q$  reference frame:

$$\begin{bmatrix} i_d \\ i_q \end{bmatrix} = \frac{2}{3} \begin{bmatrix} \cos(\varphi_e) & \cos\left(\varphi_e - \frac{2\pi}{3}\right) & \cos\left(\varphi_e - \frac{4\pi}{3}\right) \\ -\sin(\varphi_e) & -\sin\left(\varphi_e - \frac{2\pi}{3}\right) & -\sin\left(\varphi_e - \frac{4\pi}{3}\right) \end{bmatrix} \begin{bmatrix} i_a \\ i_b \\ i_c \end{bmatrix} \quad (3.40)$$

$$\begin{bmatrix} i_a \\ i_b \\ i_c \end{bmatrix} = \frac{2}{3} \begin{bmatrix} \cos(\varphi_e) & -\sin(\varphi_e) \\ \cos\left(\varphi_e - \frac{2\pi}{3}\right) & -\sin\left(\varphi_e - \frac{2\pi}{3}\right) \\ \cos\left(\varphi_e - \frac{4\pi}{3}\right) & -\sin\left(\varphi_e - \frac{4\pi}{3}\right) \end{bmatrix} \begin{bmatrix} i_d \\ i_q \end{bmatrix}.$$

The stator flux and motor torque can also be represented in the  $d - q$  frame as

$$\begin{aligned} \psi_d &= (L_s + M_s)i_d + \psi_m \\ \psi_q &= (L_s + M_s)i_q \\ \psi_s &= \sqrt{\psi_d^2 + \psi_q^2} \end{aligned} \quad (3.41)$$

where the flux  $\psi_m$  is aligned with the rotor and has zero  $q$ -axis component, and  $\psi_s$  is the magnitude of the stator flux linkage. The motor electromagnetic torque via the cross product of the space vector of the stator flux and the stator current has the following form

$$T_E = \frac{3}{2}p(\psi_d i_q - \psi_q i_d) = \frac{3}{2}p\psi_m i_q. \quad (3.42)$$

The current and voltage variables in the  $d - q$  reference frame are DC signals. According to (3.42), and taking into account that the flux of a permanent magnet assumed to be constant, the control of stator currents  $q$ -axis component is a key to control of electromagnetic torque. This approach simplifies the control architecture and makes it possible to use a PID control in similar manner to the DC motor control structures as shown in current control loop in Fig. 16 [46],[47].

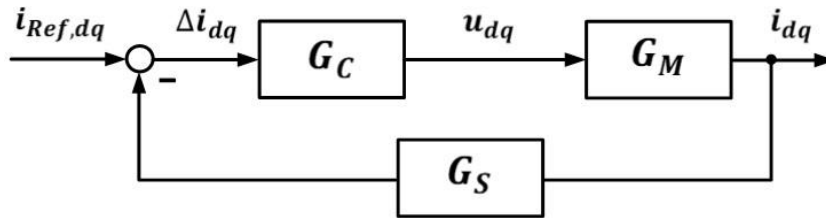


Fig. 16. Current PID Control Configuration in Space Vector Representation.

where  $G_c(s)$  the PID controller transfer function,  $G_M(s)$  is the motor transfer function and  $G_s(s)$  is the current sensor transfer function. However, synchronous transformations require the information about the rotor position. This necessitates the use of position sensor or complex algorithms for its determination. In addition, as shown in (3.27), (3.39), (3.40) and (3.42), the phase current waveforms are ideally sinusoidal. In practice, the back-EMF values often have additional harmonics, which can be displayed on the electric torque according to (3.8). In such situations, the methods of back-EMF compensation with an observer are usually used. The more seamless solution for this problem will be presented in Chapter 5.



### 3.4.2 Field Oriented Control

The Conventional Field Oriented Control (FOC) related to PMSM or AM is based on the Clarke – Parks Transformations of three phase currents to two orthogonal components using (3.40), where  $q$ -component is associated with the motor torque, and  $d$ -component with the magnetic flux [46]-[49]. This simplifies the control loop and leads to torque control architecture which uses a PID control for both currents  $i_d$  and  $i_q$ . The PID current control affords an opportunity to achieve very good accuracy and dynamic operation of the control system. The Clarke-Park transformations are based on the rotor position that can be measured via an encoder or hall sensors on the machine. The current sensors are needed for estimation of actual phase currents values, which will be then transformed into actual  $i_d$  and  $i_q$ . The current references  $i_{Ref,d}$  and  $i_{Ref,q}$  can be estimated according to (3.41) and (3.42), from reference stator flux  $\psi_{Ref}$  and reference motor torque  $T_{Ref}$ , respectively. The difference between current references and actual  $i_d$ ,  $i_q$  values gives the current errors  $\Delta i_d$  and  $\Delta i_q$ , which can be controlled independently according to (3.38) as shown in Fig. 16. Calculated with a given motor and sensors parameters, PID controller can determine the respective actual voltages  $u_d$ ,  $u_q$  in dependence to current error values. The block diagram of Field Oriented Control with nonlinear cross-coupling and back-EMF compensation is shown in Fig. 17. The nonlinear cross-coupling terms in (3.38) through  $\omega_e(L_s + M_s)i_d$ ,  $\omega_e(L_s + M_s)i_q$  and  $\omega_e\psi_m$  can be eliminated using auxiliary variables  $u_q^*$  and  $u_d^*$  as [46]-[49]

$$\begin{aligned} u_d^* &= \omega_e(L_s + M_s)i_q \\ u_q^* &= \omega_e(L_s + M_s)i_d + \omega_e\psi_m \end{aligned} \quad (3.43)$$

However, according to (3.43), very low phase inductance ( $L_s + M_s$ ) of PM motors with air-gap or combined windings makes these components insignificant. Therefore, in order to reduce the calculation time of the microcontroller cycle, this step can be neglected. The mismatch between sinusoidal stator phase currents and non-ideal back-EMF leads to the torque fluctuations. In order to reduce this problem, the back-EMF compensation method based on the back-EMF harmonic content estimation according to (3.4) and (3.5) is widely used and transformed in  $d - q$  frame by means of (3.40).

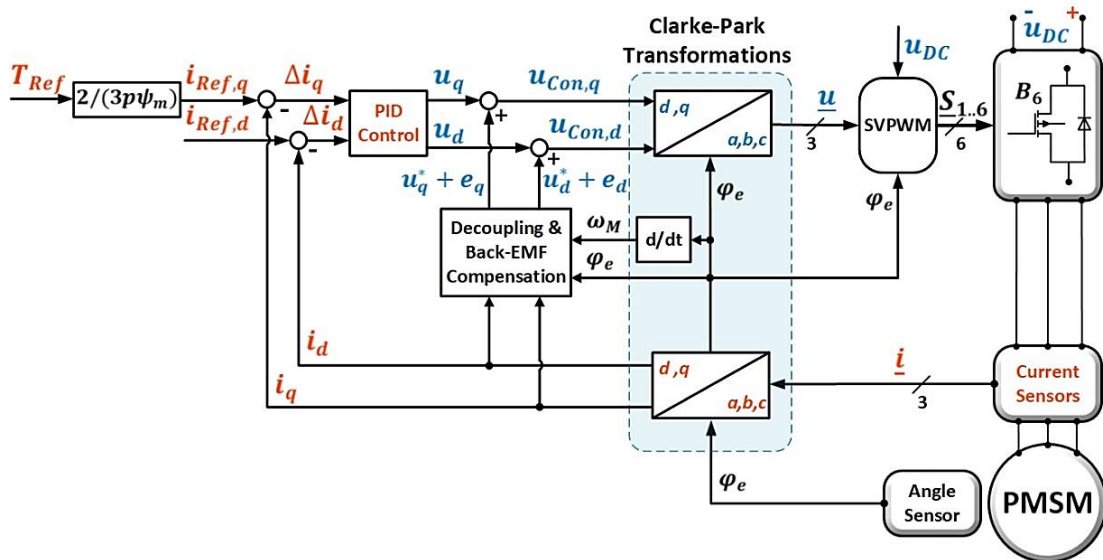


Fig. 17. Field Oriented Control (FOC) Block Diagram for PMSM.

However, this method doesn't change the sinusoidal form of phase current and as a result doesn't compensate every additional harmonic in the torque waveform [46]-[49]. The other possibility to deal with this problem according to [46]-[49] is a supplementing of additional harmonics to the reference currents  $i_{Ref,d}$  and  $i_{Ref,q}$ . Even so, this approach is very complex because of Clarke-Park transformations and requires much calculation time in microcontroller, which is a very important criterion for the control system of a PMSM with air-gap or combined winding due to high switching frequency. The reference voltages  $(u_d, u_q)$  with decoupling components  $(u_q^*, u_d^*)$  and EMF compensation are then converted back into the fixed stator coordinate system voltages  $\underline{u} = [u_a \ u_b \ u_c]^T$  by means of the inverse Clarke-Park transformations. The control voltages  $\underline{u}$  set the motor in motion via a Space Vector Modulation and B6-bridge.

The Field Oriented Control allows to operate the PMSM at speeds higher than the rated one in the field weakening range as shown in Fig. 18. During normal operation,  $i_{Ref,d}$  is set to zero. According to (3.41), and considering that the phase inductance is very low, the stator flux will be equal to  $\psi_m$ . Increase of  $i_{Ref,d}$  saturates the stator with magnetic flux. In the same time, decrease of  $i_{Ref,q}$  leads to loss of motor torque according to (3.42).

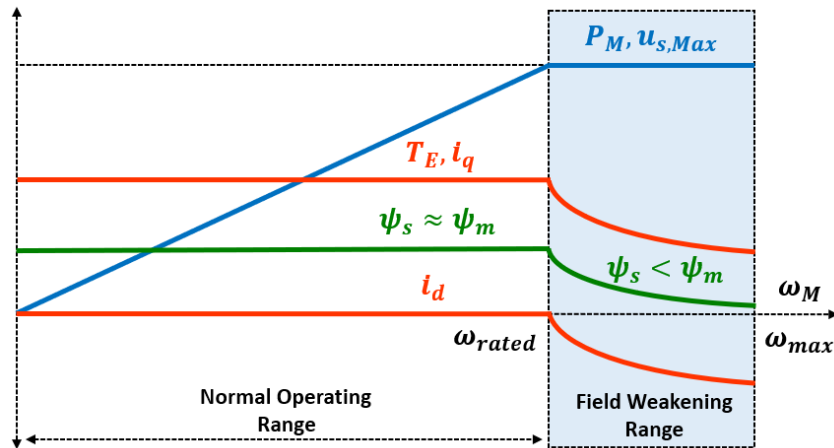


Fig. 18. PMSM Operation in Normal Range and Field Weakening Range.

The field weakening approach guarantees a maximum possible torque, power and efficiency at the speed range after the rated value [46]-[49]. From the practical point of view, in electric vehicles, this approach can find its application in cases, where the load torque is not high and the vehicle runs at an increased speed, for example, from a mountain down. However, for the PM motor with air-gap winding, the implementation of this method can be ineffective due to a very low inductance and low magnetic field produced by the stator winding, which greatly narrows the field weakening area. It can be easily confirmed using (3.41) and (3.42). Nevertheless, FOC allows to implement this approach if appropriate.

To summarize, it can be mentioned, that FOC as a control method for PM motors with air-gap or combined winding has the following advantages [46]-[49]:

- it allows to create a high dynamic and stable PMSM control system;
- it makes it possible to implement the field weakening applications.

However, FOC is based on sinusoidal waveforms of phase currents due to the used Clarke-Park transformations. It leads to the following disadvantages [2]:

- in case of a higher harmonic B-field it is difficult to adapt the phase current waveform explicitly to the specified requirements of torque or losses;
- Clarke-Park transformations introduce additional errors, which may be uncompensated by a controller in case of a high-speed range and may introduce significant current deviations from the values given;
- the necessary transformations, which include trigonometric functions based on the electrical angle, complicate the control implementation in the microcontroller software, which must be carried out in each sampling step with high frequency.

Generally, the solution for the first and the second problems is a back-EMF compensation based on repetitive effects, but for high power low inductance motors it is not effective. The last disadvantage of this method is due to the low motor inductance that requires a high PWM switching frequency to limit the phase currents ripple. It leads to very short sampling time and calculation intervals of a microcontroller, which raises the system price because of necessity to use expensive types of microcontrollers or special hardware like FPGAs [2].

### 3.4.3 Direct Torque Control

The Direct Torque Control (DTC) offers a further possibility for controlling three-phase machines. This method described in [46],[47],[50]-[59] is preferably used for a better control of the power in stationary as well as in dynamic operation. Furthermore, the DTC is dependent on a few parameters of the electrical machine. The Direct Torque Control stems from the fact that the stator flux and motor torque can be controlled directly, without intermediate two  $d - q$  current control loops. In addition, this form of control can be investigated in the stationary reference ( $\alpha - \beta$ ) frame based on (3.33) - (3.35). It means that the estimation of actual values of torque  $T_E$  and flux  $\psi_s$  does not require a speed sensor to detect the rotor angle, and can be carried out from actual values of stator currents in  $\alpha\beta$  coordinate system. The difference between the motor torque  $T_{Ref}$  and flux  $\psi_{Ref}$  references and actual values gives the torque and stator flux errors  $\Delta T_E$  and  $\Delta\psi_s$ . However, in conventional DTC these errors are used in a completely different way compared to the FOC based on PID controllers. The torque and flux errors in the conventional DTC drive the inverter by means of hysteresis controllers without any intermediate current control loops. Hysteresis controllers are used to define the more optimal inverter states, in which the errors in the stator flux and motor torque are minimal and remain within the predetermined hysteresis bands [50]. The output signals from torque and flux hysteresis controllers  $\varepsilon_T$  and  $\varepsilon_\psi$  can be defined as

$$\varepsilon_\psi = \begin{cases} 1, & \text{if } \Delta\psi_s \geq |\text{hysteresis band}| \rightarrow \text{to increase } \psi_s \\ 0, & \text{if } \Delta\psi_s \leq -|\text{hysteresis band}| \rightarrow \text{to decrease } \psi_s \end{cases}$$

$$\varepsilon_T = \begin{cases} 1, & \text{if } \Delta T_E \geq |\text{hysteresis band}| \rightarrow \text{to increase } T_E \\ 0, & \text{if } \Delta T_E = 0 \\ -1, & \text{if } \Delta T_E \leq -|\text{hysteresis band}| \rightarrow \text{to decrease } T_E. \end{cases} \quad (3.44)$$

Equation (3.44) shows that the magnetic flux can be controlled by two switching states. The stator flux can then either be increased or decreased. At a magnification the first switching state is present, at a flux reduction of the flux controller switching state is zero. On the other hand, the motor torque can assume three switching states. If the state is zero, the torque is kept constant by means of a zero-space pointer. If there is a positive switching state, the torque is increased accordingly. A reduction of the torque is required when the actual torque reaches the outer limit of the tolerance band. The eight space vectors  $V_{1..8}$  switching strategy for controlling the amplitude and rotating direction can be selected according to

the combination between the switching states  $\varepsilon_T, \varepsilon_\psi$  and the stator flux phase  $\theta_\psi = \arctan \frac{\psi_\beta}{\psi_\alpha}$  and stored in the TABLE IV. As a result, the selected voltage vector rotates the stator flux and produces the reference motor torque [50].

TABLE IV. EIGHT-VECTOR SWITCHING TABLE OF DTC

$\varepsilon_\psi$	$\varepsilon_T$	$0 \leq \theta_\psi < \frac{\pi}{3}$	$\frac{\pi}{3} \leq \theta_\psi < \frac{2\pi}{3}$	$\frac{2\pi}{3} \leq \theta_\psi < \pi$	$\pi \leq \theta_\psi < \frac{4\pi}{3}$	$\frac{4\pi}{3} \leq \theta_\psi < \frac{5\pi}{3}$	$\frac{5\pi}{3} \leq \theta_\psi \leq 2\pi$
$I$	$I$	$V_2(110)$	$V_3(010)$	$V_4(011)$	$V_5(001)$	$V_6(101)$	$V_1(100)$
	$0$	$V_7(111)$	$V_8(000)$	$V_7(111)$	$V_8(000)$	$V_7(111)$	$V_8(000)$
	$-I$	$V_6(101)$	$V_1(100)$	$V_2(110)$	$V_3(010)$	$V_4(011)$	$V_5(001)$
$0$	$I$	$V_3(010)$	$V_4(011)$	$V_5(001)$	$V_6(101)$	$V_1(100)$	$V_2(110)$
	$0$	$V_8(000)$	$V_7(111)$	$V_8(000)$	$V_7(111)$	$V_8(000)$	$V_7(111)$
	$-I$	$V_5(001)$	$V_6(101)$	$V_1(100)$	$V_2(110)$	$V_3(010)$	$V_4(011)$

Provided that the motor phase resistors and inductance are in the same range, the phase voltages stored in the TABLE IV. and transformed in  $\alpha\beta$  coordinate system by means of (3.33) can be used to flux and torque calculation according to (3.34) and (3.35).

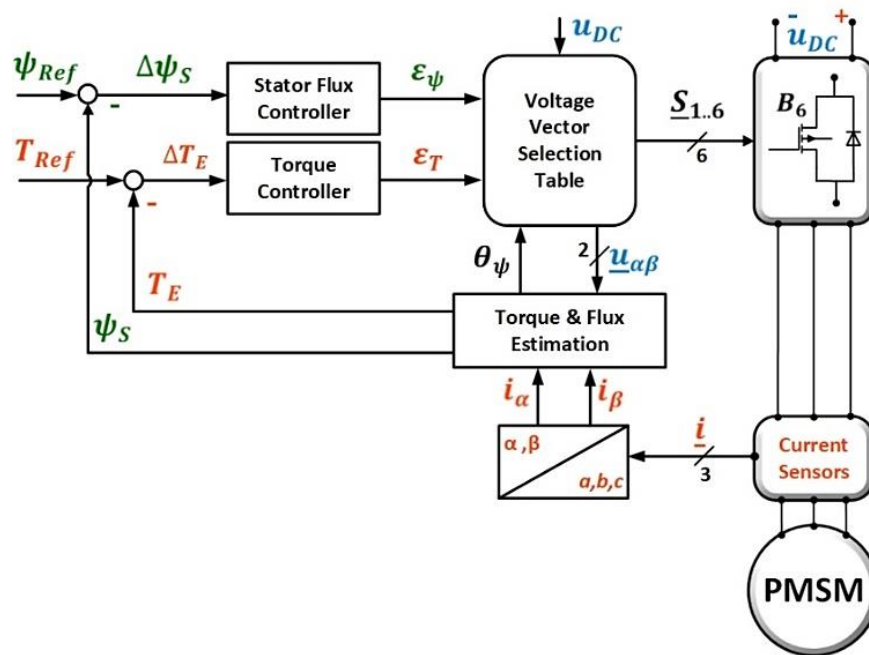


Fig. 19. Direct Torque Control Block Diagram for PMSM.

This avoids the employing of voltage sensors in the system, but at the same time negatively affects its accuracy. The conventional DTC block diagram for PMSM represented in stationary ( $\alpha - \beta$ ) reference frame is shown in Fig. 19. As it can be mentioned from the block diagram, the DTC strategy doesn't require angle sensor and trigonometric transformation from  $\alpha\beta$  to  $dq$  coordinate system. In addition, switching signals stored in the table allow to simplify the DTC implementation in a microcontroller. The main advantage of the DTC is a fast-dynamic response and good robustness against the motor

parameters variation [50]. However, the design of the conventional DTC controller has its disadvantages. The first one is the variable switching frequency due to a hysteresis controller. At high reference torques, it leads to the high torque and current ripple and makes the control system unstable. This problem may be more substantial in case of employing DTC for PM motor with air-gap winding. Very low motor inductance results in a very low stator flux. It means that hysteresis bands of the controllers should be very narrow to keep the current ripples in the acceptable range. It requires an excessively high switching frequencies and makes the implementation of this method impossible for driving a PM motor with air gap winding taking into account a modern power electronics capabilities. For PM motors with combined winding, this problem may be less critical due to the additional slotted winding. However, it does not change the situation significantly. The other disadvantage of the DTC in terms of a non-ideal back-EMF is the compensation complexity of the additional harmonics in the back-EMF. DTC methods based on the representation in  $dq$  reference frame and the PID controller [50]-[59] are devoid of basic virtues of DTC and does not have specific differences in comparison with FOC.

To summarize, it is possible to underline the main advantages of the conventional DTC represented in the  $\alpha\beta$  coordinate system in case of using for a PMSM with combined winding [50]-[59].

- high dynamics due to the direct control of flux and torque;
- indirect control of phase voltages and currents and absence of current controllers;
- absence of Park Transformations;
- requirement to know only the sector, in which the stator flux is positioned, in contrast to FOC, which requires the exact position of the rotor;
- low calculation value in a microcontroller;
- no sensitivity to parameter changings (only to phase resistance variation due to temperature).

However, the next three disadvantages militate against success of implementation of DTC for PM motors with combined winding [50]-[59]:

- excessively high switching frequencies;
- high torque and current ripples;
- difficult implementation of the B-Field additional harmonics compensation.

### 3.4.4 Optimal Control

The Optimal Control is widely used in automotive, power electronics, drives, aerospace and chemicals applications. The desired behavior of the system can be represented in a cost function. The main benefit of the optimal control comes from the estimation of the controller parameters by minimization of quality criteria included in the cost function. Any system can be qualified as a linear system, if such properties as homogeneity, additivity and superposition are related to this system [46]-[47]. It means that it is possible to predict the response to any possible input based on few numbers of inputs. Thus, the system of a PM motor with air-gap or combined winding can be called linear, if phase resistance, inductance, harmonic coefficients of B-field and other motor parameters are constant and independent of the motor speed and load. For a PMSM described as linear systems, there are many optimal control methods like Linear Quadratic Regulator (LQR) or Model Predictive Control (MPC) [60]-[64]. The design of LQR control methods is based on the motor model representation in  $dq$  reference frame using (3.36) - (3.42) and starts with a description of a motor system by means of the state space. The back-EMF compensation with decoupling of  $dq$  current components according to (3.43) affords an opportunity to formulation of the currents state spaces. Respectively, the following time-continuous, linear system can be created as

$$\begin{aligned} d\dot{\underline{i}}_{dq}/dt &= \underline{A}_{dq} \cdot \dot{\underline{i}}_{dq} + \underline{B}_{dq} \cdot \underline{u}_{dq} \\ \begin{pmatrix} \dot{i}_d \\ T_E \end{pmatrix} &= \underline{C}_{dq} \cdot \dot{\underline{i}}_{dq} + \underline{D}_{dq} \cdot \underline{u}_{dq}, \end{aligned} \quad (3.45)$$

with dynamic matrix  $\underline{A}_{dq}$ , input matrix  $\underline{B}_{dq}$ , output matrix  $\underline{C}_{dq}$  and direct link  $\underline{D}_{dq}$ . The quadratic cost function

$$J = \frac{1}{2} \int_0^{\infty} \left( \dot{\underline{i}}_{dq}^T \underline{Q}_{dq} \dot{\underline{i}}_{dq} + \underline{u}_{dq}^T \underline{R}_{dq} \underline{u}_{dq} + 2\underline{u}_{dq}^T \underline{N}_{dq} \dot{\underline{i}}_{dq} \right) dt \quad (3.46)$$

weights states  $\dot{\underline{i}}_{dq}$  and control inputs  $\underline{u}_{dq}$  according to weighting matrices  $\underline{Q}_{dq}$ ,  $\underline{R}_{dq}$  and  $\underline{N}_{dq}$ . The quadratic cost function can be minimized by the solution  $\underline{S}_{dq}$  of the algebraic matrix Riccati equation

$$\underline{A}_{dq}^T \underline{S}_{dq} + \underline{S}_{dq} \underline{A}_{dq} + (\underline{S}_{dq} \underline{B}_{dq} + \underline{N}_{dq}) \underline{R}_{dq}^{-1} (\underline{B}_{dq}^T \underline{S}_{dq} + \underline{N}_{dq}^T) = -\underline{Q}_{dq}, \quad (3.47)$$

which determines the state feedback matrix

$$\underline{K}_{dq} = \underline{R}_{dq}^{-1} (\underline{B}_{dq}^T \underline{S}_{dq} + \underline{N}_{dq}^T). \quad (3.48)$$

The control voltages can be estimated by multiplication of the feedback matrix and the state vector  $\dot{\underline{i}}_{dq}$ . The prefilter  $\underline{F}_{dq}$  is used to specify the requested motor electrical torque  $T_E$  with current  $i_d$  and can be formed from the inverse steady state transfer matrix of the closed loop as

$$\underline{F}_{dq} = \left( \underline{C}_{dq} \cdot (\underline{A}_{dq} - \underline{B}_{dq} \cdot \underline{K}_{dq})^{-1} \underline{B}_{dq} \right)^{-1} \quad (3.49)$$

Multiplication by the prefilter allows to convert the motor torque and current  $i_d$  into the feedforward part of control voltage  $\underline{u}_{dq}$ . The block diagram of LQR control is illustrated in Fig. 20 [60].

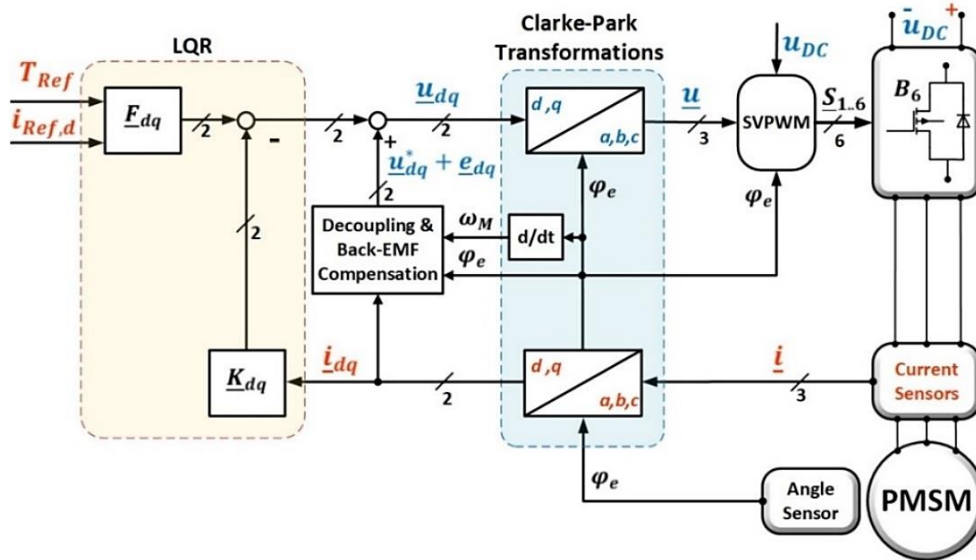


Fig. 20. LQR Control Block Diagram for PMSM.

The Model Predictive Control (MPC) combined with the terminologies of the finite control set (FCS) or continues control set (CCS) allows to predict future response of a process due to the explicit process model used in MPC algorithms [65]-[80]. The original FCS-MPC doesn't include integral action and is based on the numerical optimization. The minimization of the objective function specified as a sum of square errors between the desired and the predicted currents  $\dot{\underline{i}}_{dq}$

$$J = (i_{Ref,d}(t_i) - i_d(t_{i+1}))^2 + (i_{Ref,q}(t_i) - i_q(t_{i+1}))^2 \quad (3.50)$$

helps to solve the optimization problem of future actuations, where  $i_{dq}(t_{i+1})$  are one-step-ahead predictions of  $\hat{i}_{dq}$  and  $t_i$  is the sampling time. The prediction values of  $\hat{i}_{dq}$  can be achieved by

$$\begin{bmatrix} \hat{i}_d(t_{i+1}) \\ \hat{i}_q(t_{i+1}) \end{bmatrix} = (I + \Delta t A_M(t_i)) \begin{bmatrix} i_d(t_i) \\ i_q(t_i) \end{bmatrix} - \begin{bmatrix} 0 \\ \frac{\omega_e(t_i) \psi_m \Delta t}{L_s + M_s} \end{bmatrix} + \Delta t B_M \begin{bmatrix} u_d(t_i) \\ u_q(t_i) \end{bmatrix}, \quad (3.51)$$

where  $\Delta t$  is a sampling interval,  $I$  is the  $2 \times 2$  identity matrix,  $A_M(t_i)$  and  $B_M$  are the system matrices described as

$$A_M(t_i) = \begin{bmatrix} -\frac{R_s}{L_s + M_s} & \omega_e(t_i) \\ \omega_e(t_i) & -\frac{R_s}{L_s + M_s} \end{bmatrix}; B_M = \begin{bmatrix} \frac{1}{L_s + M_s} & 0 \\ 0 & \frac{1}{L_s + M_s} \end{bmatrix}. \quad (3.52)$$

The manipulated voltage variables  $u_d(t_i)$  and  $u_q(t_i)$  can be calculated offline according to the inverter operation and its switching states, for example, from the TABLE II. Substituting (3.51) into the objective function (3.50) gives the eight values of the objective function for every switching state. Thus, searching the minimal value of these eight quantities corresponded to the optimal switching state is the key to a motor control. The block diagram of FCS-MPC control is illustrated in Fig. 21 [65]-[80].

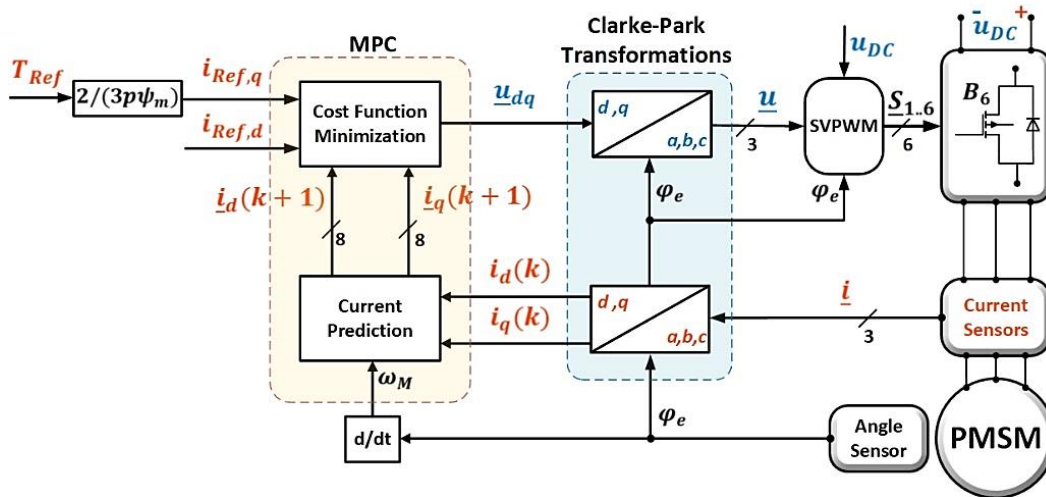


Fig. 21. FCS-MPC Control Block Diagram for PMSM.

It should be noted, that FCS-MPC compared to the LQR doesn't require the decoupling of  $dq$  current components. However, the eight values of the objective function based on (3.50) and (3.51) and their minimal solution must be calculated for each sampling interval. It requires a high processor power. In case of very high switching frequency and, respectively, very small calculation interval, implementation of MPC for a PMSM with air gap or combined winding can be very complicated. According to [70], CCS-MPS method is able to overcome the disadvantages of FCS-MPC in switching frequency uncertainty. However, application of this approach does not simplify the system significantly.

LQR or MPC methods allows to create a fast dynamical and stable system in the one hand, and to minimize the torque ripples or motor losses, in the other. However, these optimal approaches can be successfully implemented for a linear object and are sensitive to changes of system model parameters. It means, that the optimization performance may be affected due to distortion current, dead zone effect

and mismatch of motor or sensor parameters caused by the temperature increase or other factors. It results in the steady state and dynamic performance deterioration and may lead to the system failure. Moreover, the additional dynamics of inverters and current sensors increases the dimension of the system and complicates the selection of weighting factors. According to [70], in order to eliminate these problems, it is possible to use a current and disturbance observation. However, adaptation of this optimal methods for PM motors with very low phase inductance makes extremely difficult the online application and requires a high processor power due to very high switching frequency.

To summarize, according to [65]-[80], it is possible to underline the next main advantages of optimal methods as a control application for a PMSM with air gap or combined winding:

- very fast torque and current response and good steady state performance;
- very good ability for minimization of motor losses and torque ripple.

However, the optimal control algorithm is defined by some shortcomings as:

- high calculation interval during the online application;
- strict dependence on the motor parameters;
- necessity in observer to reconstruct the complete state.

### 3.5 Six-Step Commutation Control

According to [12],[18],[20] and [13], a PMSM with air gap or combined winding can be controlled as a brushless DC Motor with a trapezoidal back-EMF waveform by means of the Six-Step Commutation (SSC) with control of the source current or voltage. This method is not an optimal solution for a combined winding PMSM due to the high phase current ripples during the commutation interval [12]. However, the SSC control due to its simplicity and low-cost can find its application for air gap winding PM motors operating in a middle voltage and current range described in [81]-[91]. This chapter will present the SSC control for the 3-phase air gap and combined winding PM motors based on the six-step square-wave commutation with control of the source current by means of a DC-DC buck-boost converter.

#### 3.5.1 Six-Step Commutation Logic

In case of a PMSM with air gap or combined winding and non-ideal back-EMF, the rotor position, according to the B-Field or back-EMF waveform, can be divided into 6 sectors for one pair of poles as shown in Fig. 22. In order to keep the motor running, the stator windings should be energized according to the rotor position considering the shift between the stator and the rotor magnetic fields. Fig. 22 shows the ideal phase current behaviors without current ripples in commutation points, where  $i_m$  is a required phase current amplitude. However, ideal current waveforms combined with non-ideal B-Fields shown in Fig. 11, according to (3.8), give 12.5% fluctuations of the electrical torque considering that  $k_M = 1$ .



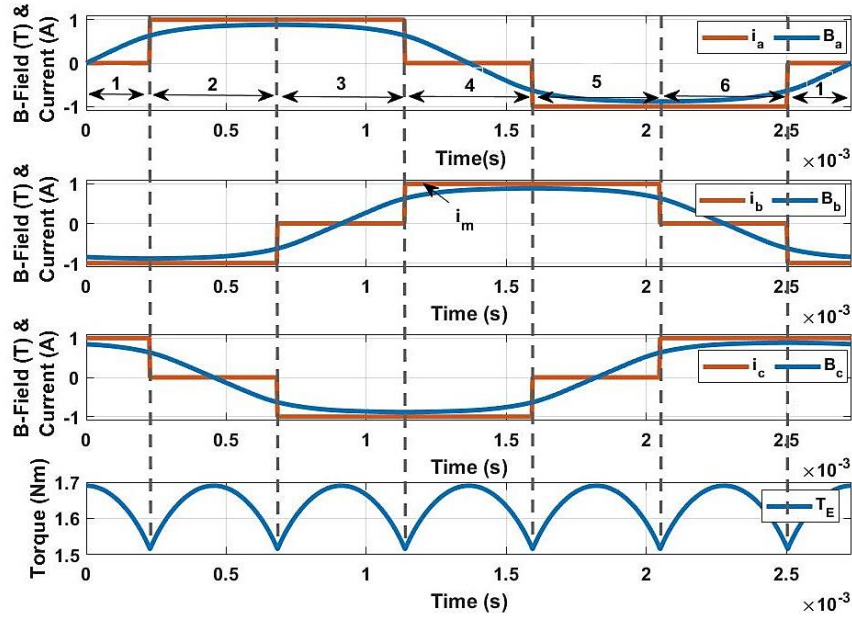


Fig. 22. Ideal Three-Phase Currents in Comparison to B-Fields in SSC.

During the ideal six-step square-wave commutation, the current fluctuations rate caused by the phase inductance can be neglected considering the extremely low motor inductance value. Thus, the square-wave current commutation is caused by the fact that only two phases are turned on at any time. As a result, the ideal motor torque waveform  $T_E$  during the square-wave commutation can be expressed according to (3.8) as

$$T_E(\varphi_e) = k_M(i_x B_x(\varphi_e) + i_y B_y(\varphi_e)) = k_M B_{xy}(\varphi_e) i_{xy} = \frac{i_{xy} e_{xy}(\varphi_e)}{\omega_m}, \quad (3.53)$$

where index  $x$  and  $y$  describe two of the three turned on phases,  $B_{xy}(\varphi_e)$  is the function of B-fields shape difference at position  $\varphi_e$  and  $i_{xy}$  is the motor input current, in ideal representation of SSC is equal to  $i_m$ . Without taking into consideration of commutation process, the conduction interval with the current flowing from phase  $a$  to phase  $b$  can be designated as  $AB$  interval. In the same way, it is possible to describe the other five intervals:  $AC$ ,  $BC$ ,  $BA$ ,  $CA$  and  $CB$ . The B-Field difference shape function  $B_{xy}(\varphi_e)$  in every six intervals can be estimated according to TABLE V.

TABLE V. B-FIELDS DIFFERENCE IN SIX INTERVALS

Sectors	1	2	3	4	5	6
Intervals	$CB$	$AB$	$AC$	$BC$	$BA$	$CA$
$B_{xy}(\varphi_e)$	$B_c - B_b$	$B_a - B_b$	$B_a - B_c$	$B_b - B_c$	$B_b - B_a$	$B_c - B_a$

TABLE V. , Fig. 22 and (3.53) show that, compared to the conventional commutated BLDC motor with trapezoidal B-Field waveforms described in [81], implementation of this method for a PM motor with air gap or combined winding and non-ideal back-EMF and, respectively, B-Field waveforms leads to electrical torque fluctuations. Although these ripples are not enough to cause large fluctuations in the motor speed, nevertheless, they affect the current waveform and the accuracy of the system. The great

advantage of SSC is the lack of need for measuring the exact position of the rotor. The motor commutation requires only information about the interval limits, in which the rotor is located. Thus, the magnetic flux density of permanent magnets can be measured by means of cheap and simple discrete hall sensors. If the rotor position for a 3-phase motor is determined by three hall sensors with offset by  $120^\circ$  electrical degrees, the signal combinations for each rotor position are clearly defined. In SSC, the current should be switched between the phases in six steps every  $60^\circ$  electrical degrees for a full electrical revolution. For example, for a wheel hub motor with air gap winding, the sensors can be arranged above the end faces of the permanent magnets and are firmly connected to the stator as shown in Fig. 23 in a CAD model (left) and schematic (right) [18],[118].

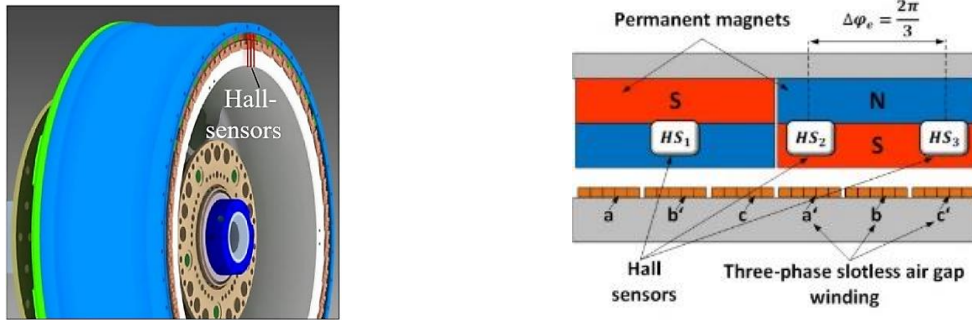


Fig. 23. Hall Sensors in CAD-Model (left) and Schematic (right) [18].

Hall sensors change their logic level each time the detected magnetic flux density exceeds or falls below fixed switching thresholds, whereby unipolar hall sensors can only detect one direction of the rotor rotation. The sensors are positioned on the motor stator in order to detect the magnetic field above the end faces of the alternating permanent magnets. The three digital hall sensor signals  $HS_{1,2,3}$  can be modelled as a function of the electrical angle

$$\begin{aligned}
 HS_1 &= \begin{cases} 0, & B_{sw} < B_a(\varphi_e) \\ 1, & B_{sw} \geq B_a(\varphi_e) \end{cases} \\
 HS_2 &= \begin{cases} 0, & B_{sw} < B_b(\varphi_e + 2\pi/3) \\ 1, & B_{sw} \geq B_b(\varphi_e + 2\pi/3) \end{cases} \\
 HS_3 &= \begin{cases} 0, & B_{sw} < B_c(\varphi_e + 4\pi/3) \\ 1, & B_{sw} \geq B_c(\varphi_e + 4\pi/3) \end{cases}
 \end{aligned} \tag{3.54}$$

using the magnetic flux density curves  $B_{abc}(\varphi_e)$  and a constant switching threshold  $B_{sw}$ , normally equal to zero for a unipolar hall sensors [18],[20]. Based on the hall sensor information, the  $2^3$  possible combinations of commutation signals can be generated to energize the six power transistors in the B6 bridge. Absorption law makes it possible to simplify this combination with *AND* and *OR* logic. Using the absorption law, the modelling effort can thus be reduced. All combinations between six switching signals and three Hall sensor signals are shown in the following TABLE VI. for a clockwise and anticlockwise rotated rotor [18],[20].

TABLE VI. SWITCHING TABLE OF COMMUTATION SIGNALS

	<i>CB</i>	<i>AB</i>	<i>AC</i>	<i>BC</i>	<i>BA</i>	<i>CA</i>
$\curvearrowright$	$\overline{HS_2} \wedge HS_3$	$HS_1 \wedge \overline{HS_2}$	$\overline{HS_1} \wedge HS_3$	$HS_2 \wedge \overline{HS_3}$	$\overline{HS_1} \wedge HS_2$	$HS_1 \wedge \overline{HS_3}$
$\curvearrowleft$	$HS_2 \wedge \overline{HS_3}$	$\overline{HS_1} \wedge HS_2$	$HS_1 \wedge \overline{HS_3}$	$\overline{HS_2} \wedge HS_3$	$HS_1 \wedge \overline{HS_2}$	$\overline{HS_1} \wedge HS_3$

This approach allows the motor commutation regardless of the current control system discussed in the next chapter. However, the application of SSC in practice for a PM with air gap or combined winding leads to large current picks during the commutation points caused by a very low motor inductance. In the other hand, non-ideal back EMF affects the current fluctuations.

### 3.5.2 Six-Step-Commutation with Control of Source Current

According to [81]-[91], the current control of PMSM or BLDC motors with SSC can be achieved with a step-down (buck) DC-DC converter included in the control system between supply voltage and B6 bridge as shown on the motor control circuit diagram in Fig. 24. As it can be seen on the control circuit diagram, the motor input current can be controlled by means of a PI controller. Output from the PI controller is a duty cycle  $D_{bc}$ , which sets a PM motor in motion with the reference current  $i_{Ref}$  via a standard pulse width modulation (PWM) with switching frequency  $f_{PWM}$ .

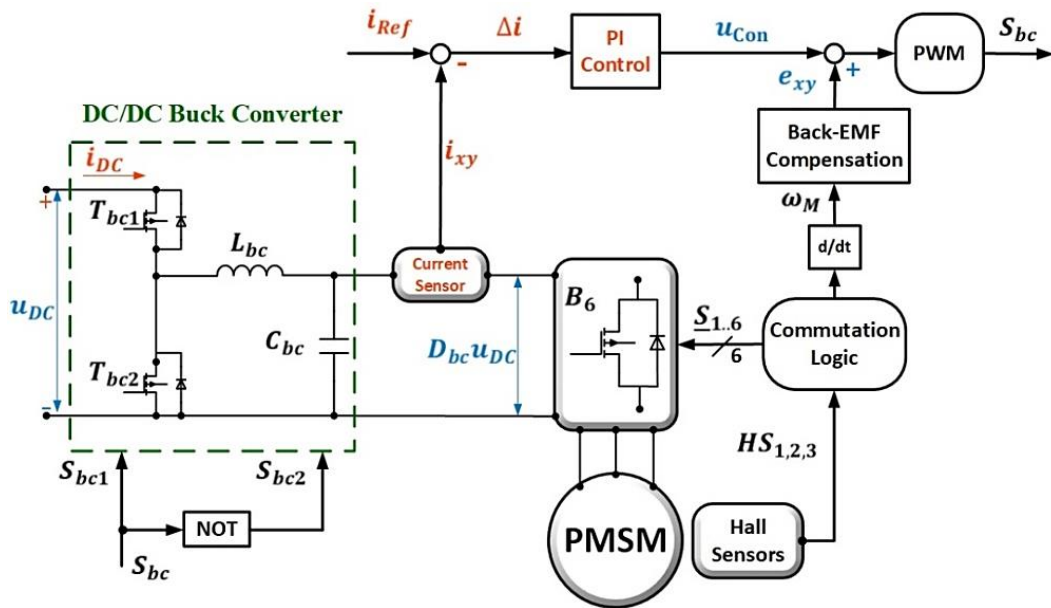


Fig. 24. Block Diagram of SSC with Input Current Control by Means of DC-DC Converter.

A buck converter is able to operate in a continuous current mode without interruptions of inductive current  $i_{coil}$  provided that the inductor value  $L_{bc}$  and the converter switching frequency  $f_{PWM}$  will be high enough [81]. As shown in Fig. 25, the switching signal states of the buck converter  $S_{bc}(t)$  can be separated according to a repetitive state  $n$  as

$$S_{bc}(t) = \begin{cases} 1, & t \in (n\Delta t_{bc}, (n + D_{bc})\Delta t_{bc}) \\ 0, & t \in ((n + D_{bc})\Delta t_{bc}, (n + 1)\Delta t_{bc}), \end{cases} \quad (3.55)$$

where *one* represents switch on, *zero* represents switch off,  $\Delta t_{bc} = 1/f_{PWM}$  is a buck converter switching period inversely proportional to the switching frequency and  $D_{bc}$  is a duty cycle. These two operating modes are shown in Fig. 25 (a), (b), respectively, for one switching period.

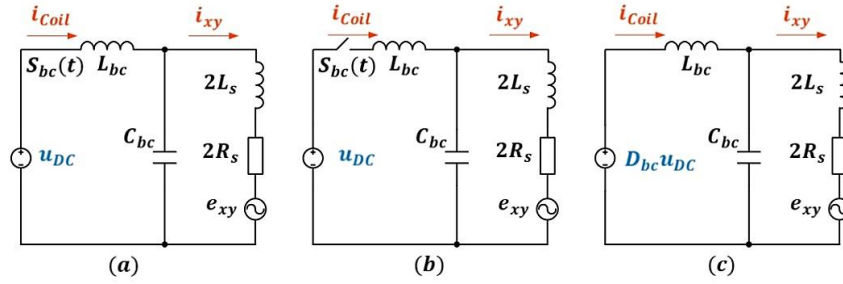


Fig. 25. Operating Modes of the DC-DC Buck Converter.

Taking into account a high frequency system operation state, the average state space model of the step-down converter can be simplified according to Fig. 25 (c) and described mathematically as

$$\begin{aligned} L_{bc} \frac{di_{Coil}}{dt} + u_{DC} &= D_{bc} u_{DC} \\ C_{bc} \frac{du_{DC}}{dt} + i_{xy} &= i_{Coil}, \end{aligned} \quad (3.56)$$

where  $C_{bc}$  is a buck converter capacitor. A buck converter reduces the DC supply voltage  $u_{DC}$  as a function of a duty cycle  $D_{bc}$  according to (3.56). The output current  $i_{xy}$  depends on the converter output voltage and load and consists of an effective motor power and motor losses

$$i_{xy} = \frac{\omega_M T_E + P_L}{D_{bc} u_{DC}}. \quad (3.57)$$

The last equation shows the relationship between the converter output current and the motor torque and affords an opportunity for a motor torque control taking into account equations (3.8) and (3.53). The air gap and combined winding motor model in a two-phase switching mode, assuming that phases  $x$  and  $y$  are conducting, and according to (3.1)- (3.3), can be expressed as

$$u_{DC} = R_{xy} i_{xy} + L_{xy} \frac{di_{xy}}{dt} + e_{xy}(\varphi_e), \quad (3.58)$$

where  $R_{xy} \approx 2R_s$  and  $L_{xy} \approx 2L_s$  are line-winding resistance and inductance. It leads to the well-known DC motor control structure and gives a possibility to implement a PI current control loop for a PM motor with air gap or combined winding as shown in Fig. 26.

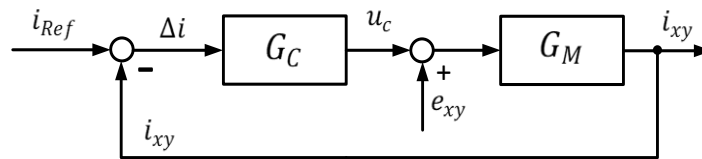


Fig. 26. Current PI Control Loop for SWC Control [81].

Thus, the transfer function of the current control loop can be greatly calculated as

$$G(s) = \frac{G_C(s)}{1 + G_C(s)G_M(s)} = \frac{i_{xy}(s)}{i_{Ref}(s)} = \frac{K_{pc}s + K_{ic}}{L_{xy}s^2 + (K_{pc} + R_{xy})s + K_{ic}} \quad (3.59)$$

where  $G_C(s) = K_{pc} + K_{ic}/s$  is a PI controller transfer function,  $G_M(s) = 1/(L_{xy}s + R_{xy})$  is the motor transfer function and  $K_{pc}$ ,  $K_{ic}$  are the PI gains. Conspicuously, the non-compensated back-EMF leads to the additional torque and phase current fluctuations according to (3.53). A more advanced SSC control

described in [81]-[91] allows to minimize torque fluctuations due to a non-ideal back-EMF and reduce the current peak during commutation. In BLDC systems with trapezoidal back-EMF, it can be achieved with hall sensors. For PMSM with a non-ideal back-EMF, the successful implementation of this method requires the exact rotor position using an encoder or analog hall sensors. The main emphasis in implementation of the advanced SSC are usually placed on the phase current and torque ripple suppression. These ripples can be separated into commutation ripple and fluctuation in the conduction region. For a PMSM with very low inductance, the conduction region ripples are classified into three groups:

1. disturbance ripples caused by non-ideal back-EMF;
2. unbalance ripples due to unbalances in phase inductances and resistances in three phase winding, especially in systems with one dc-link current sensor;
3. modulation ripples due to three-phase B6 inverter modulation, can be reduced by means of the buck converter control method.

For a PM motor with low inductance, the commutation duration is very short and leads to the current peaks able to disable transistors. The improvement of commutation region current performance for the low inductance motors can be achieved with duty ratio  $D_{B6}$  correction for B6 inverter according to [91] as

$$D_{B6} = \frac{2e_{xy}(\varphi_e) + 3R_{ph}i_{xy}}{u_{DC}} - 1, \quad (3.60)$$

The function of the back-EMF shape difference  $e_{xy}(\varphi_e)$  according to (3.4), (3.5) and TABLE V. can be obtained offline and stored in the table for each electrical angle. In this way, the commutation ripple usually resulted from uncontrollable conduction of free-wheel diodes can be minimized. In addition, the compensation of voltage disturbance  $e_{xy}(\varphi_e)$  may reduce the torque fluctuations. Unbalanced torque ripple due to unbalance in phase inductances and resistances can be compensated with observation of the motor parameter  $R_{xy}$  and  $L_{xy}$ . However, due to the very high number of poles these methods are difficult to apply to a PMSM with air gap winding and specially to combined winding motors.

In terms of the buck converter switching frequency  $f_{PWM}$  and phase current ripples  $\Delta i_{a,b,c}$  or  $\Delta i_{xy}$  associated with it in a non-commutation interval can be defined as

$$\Delta i_{xy} = \Delta i_{a,b,c} = \frac{(1 - D_{bc}) \cdot D_{bc} u_{DC}}{L_{bc} \cdot f_{PWM}}. \quad (3.61)$$

The six-step commutation with a source current control has its advantages. Namely, the PWM induced phase current ripples can be minimized by increasing the converter switching frequency  $f_{PWM}$  or inductance value  $L_{bc}$  according to (3.61). Moreover, the buck-bust converter interleaved structures afford an opportunity to control a PMSM with very low inductance without the use of high frequency converters. It leads to the optimization problem for estimation of optimal low weight DC-DC convertor parameters, which will be discussed in Chapter 4. However, due to very low motor inductance it is very difficult to reduce the commutation current peaks, which makes it impossible to use this method with powerful high voltage and high torque drives, for example, for a PMSM with combined winding. Nevertheless, the application of six-step square-wave commutation control by means of step-down converters for a PMSM with air gap winding gives the following advantages:

- system measurements are based on low-cost discrete hall sensors and one current sensor;
- low switching frequency reduces switching losses and makes the system cheaper;

- control algorithm is simple.

However, the SSC algorithm has some shortcomings, such as:

- very poor dynamics and stability of the system;
- high current and torque ripples in commutation points due to the low motor inductance;
- it is difficult to compensate the additional harmonics in the back-EMF waveform;
- requires optimized low weight DC-DC converter.

### 3.6 Comparison of Conventional Control Methods

Based on the simulation results and literary sources [39]-[91], TABLE VII. offers an approximate comparison of the above described control methods in terms of application for air gap or combined winding permanent magnet synchronous motors.

TABLE VII. COMPARISON OF CONVENTIONAL CONTROL METHODS FOR LOW INDUCTANCE PMSM

Control Method	Switching Frequency	Dynamics & Steady State	Implementation Complexity	Torque Ripple & Losses Minimization	Costs
SBC	<i>high</i>	<i>very low</i>	<i>very low</i>	<i>very low</i>	<i>middle</i>
FOC	<i>high</i>	<i>high</i>	<i>middle</i>	<i>middle</i>	<i>middle</i>
DTC	<i>very high</i>	<i>high</i>	<i>low</i>	<i>low</i>	<i>low</i>
SSC	<i>low</i>	<i>low</i>	<i>low</i>	<i>low</i>	<i>very low</i>
Optimal Control	<i>high</i>	<i>very high</i>	<i>very high</i>	<i>high</i>	<i>very high</i>

It should be noted that each of the listed methods can be modified to improve its characteristics. However, with consideration of the main requirement for the control system of a PMSM with very low inductance and high power listed in Chapter 2, the most promising is the Field Oriented Control on the current state of technology, because it gives the opportunity for implementation of the control algorithm without an observer on the low-cost industrial-applied microcontrollers, on the one hand, and has a high system dynamics and steady state, on the other hand. As a low-cost solution for an air gap winding PMSM control, SSC can be used due to its ability to avoid the high switching frequency. However, taking into account its disadvantages, this method can be used in low-cost mobile applications as e-Scooters, e-Boats or e-Longboards, where the system performance is less important than its cost.

In summary, it may be noted that none of the above described conventional methods fully satisfies the requirements for a PMSM with air gap or combined winding, since these motor designs are innovative technologies and none of the standard control methods consider its features. More specifically: very low phase inductance, high number of poles and non-ideal back-EMF waveform, which in the aggregate greatly complicate the task of the motor control. Accordingly, the new Combined Optimal Torque and Modal Current Control (OTMIC) will be presented in Chapter 5 and verified in Chapter 6 for air gap and combined winding PM motors. As a conventional solution, the FOC control will also be implemented and compared with the proposed OTMIC control in Chapter 6. In addition, in the next Chapter, the solution allowing to adapt SSC for low-cost systems based on the above-mentioned motors will be described. This solution can also be combined with other control approaches for example with [81]-[91]. However, these methods are more focused on low-power motors with low inductance value.

## 4. Air Gap Winding Motor Control without the Use of High Switching Frequency

As it has been mentioned above, the basic requirements for any mobile applications are small weight and dimensions together with minimal losses at high power. The air gap or combined winding motor technologies allow to create PMSMs with a very high specific power factor. Nevertheless, it should be considered that the weight and loss of other components of the electric motor drive must be as minimal as possible to maintain the advantages of the air gap winding motor. Conventional high-power DC-DC converters, which are normally used for steps down/up supply voltage while stepping up/down the input current, have high weight, losses and dimensions due to existence of induction coils [7]. DC-DC converters are widely used in e-Mobility for decrease/increase the DC voltage from storage batteries or for the energy recuperation [92],[93]. In addition, as it has been described in Chapter 3.5, the DC-DC converters can be used for current or voltage control in the electric motor drive with six-step commutation [92]. Thus, in mobile applications like e-Scooters, e-Bikes or electric car with air gap or combined winding PMSMs its necessary to optimize the DC-DC converter in terms of weight and losses. In addition, an optimized buck/boost converter with six-step commutation makes it possible to control the low inductance PM motor without the use of high switching frequency, which reduces cost and switching losses. Thus, the proposed algorithm can be used to control a high-power PMSM with low inductance without using a high frequency converter and to reduce the size, weight and losses of the electric drive system.

This chapter will present the optimization algorithm of the multiphase interleaved buck/boost converter. The optimization method affords an opportunity to reduce a converter weight and simultaneously its total losses considering the electromagnetic properties of coils and based on values of DC-DC converter dc supply voltage, output dc current and switching frequency. The optimization results allow to find the optimal coils geometry and prevent current saturation considering the non-linear current behavior in them. In addition, the optimization algorithm can be adapted to any coil core geometry like E-core, profile core, toroid, pot-core as well as air-core inductor and any number of interleaved converter phases. The algorithm will be presented on the example of the optimization of a three-phase interleaved buck converter with toroidal coils.

### 4.1 Optimization of a Multiphase Interleaved Buck-Boost Converter

The one phase step-down converter consists of two semiconductors operated with switching frequency  $f_{PWM}$  and two energy storage elements: a capacitor – for voltage ripple reduction and a coil – for current ripple minimization [92],[93]. Design of high-power DC-DC converters requires the consideration of three following coil properties:

- coil losses in its core and windings;
- core saturation caused by a hysteresis loop;
- nonlinear coil inductance due to sensitivity of the core material to the coil current and the switching frequency.

For example, on the one hand, the low coil inductance leads to the high switching ripple of the coil current, which increases the system losses and affects the motor torque ripple. On the other hand, a large

inductance requires more winding turns or larger cross section of the core, which leads to the high converter weight and iron losses. In addition, the coil inductance  $L_{Coil}(i_{Coil})$  is non-linear and depends on current  $i_{Coil}$  flowing through it. Increase of  $i_{Coil}$  leads to the coil saturation and excessive high current ripples [92],[93].

A multiphase interleaved buck-boost DC-DC converter consists of two, three or more single-phase DC-DC converters connected in parallel and commutated with switching frequency  $f_{PWM}/n$  with a shift in  $2\pi/n$  electrical degrees, where  $n$  is the number of converter phases [92],[93],[95]. In this case, the coil currents as well as switching frequencies of single phases is divided into  $n$ , which reduces the switching losses and the converter weight compared to the one phase step up/down converter operated with the same power range [92]. The disadvantage of the multiphase interleaved converter structure consists in complexity of implementation of the symmetrical commutation of its phases [8]. Accordingly, the three-phase interleaved buck/boost converters are used the most commonly. However, microprocessor technology development makes it possible to increase the number of converter phases, if necessary.

Thus, in a multiphase interleaved converter reduction of the coils size leads to an increase of the total losses and output current ripple. On the other hand, increase of the coil size makes the converter heavier. So, given specification leads to the mathematical optimization problem [7]. The objective function

$$F_{BC} = q_1 m_{Coils,\Sigma} + q_2 P_{BC,\Sigma} \quad (4.1)$$

must minimize the coils weight  $m_{Coils,\Sigma}$  while minimizing the converter total losses  $P_{BC,\Sigma}$ . In the same time, the total losses

$$P_{BC,\Sigma} = P_{Coils,\Omega} + P_{Coils,Core} + P_{BC,Cond} + P_{BC,Switch} \quad (4.2)$$

is a sum of iron  $P_{Coils,Core}$  and resistive  $P_{Coils,\Omega}$  losses in coils and conduction  $P_{BC,Cond}$  and switching  $P_{BC,Switch}$  losses of the power electronic. It means that total converter losses depend on the coil core material and its geometry, number of turns and wire geometry, the properties of transistors and switching frequency, as well as the required input and output voltage and rated output current. According to [7], the input values of the optimization algorithm are supply dc voltage  $u_{DC}$ , switching frequency  $f_{PWM}$ , average output converter current  $i_{xy,a}$  and a number of phases of multiphase interleaved DC-DC converter  $n$ . The output of the optimization algorithm is the optimal number of turns, wire and core geometry. In addition, the algorithm can search for the optimal solution from the given data matrix with the available core and the wire specifications. Furthermore, in order to reduce the scope of the calculation, the optimization algorithm requires initial values of the desired parameters and constraints such as: the full filling of the core space with a wire, the integer number of turns, the induction value below the core saturation and the total losses are less than the admissible total losses. The initial data must be approximately in the optimum range for more accurate results and fast calculation. Change of the weight factors  $q_1$  and  $q_2$  allows to obtain a required matrix with the optimal coil parameters. The optimization process is described on the flowchart shown in Fig. 27. Thus, the optimization algorithm of a multilevel interleaved buck-boost converter can be divided into three stages.

The first stage consists of a coils non-linear model based on the Jiles-Atherton hysteresis model and the equations chain  $\underline{u}_{Coils}(\tau) \rightarrow \underline{B}_{Coils}(t) \rightarrow \underline{H}_{Coils}(t) \rightarrow \underline{i}_{Coils}(t)$ . The time integration of coil voltages  $\underline{u}_{Coils}(t)$  leads to the coils magnetic flux densities  $\underline{B}_{Coils}(t)$ . The Jiles-Atherton hysteresis model describes the relationship between the magnetic flux density and the field strength  $\underline{H}_{Coils}(t)$  [7]. The dependency between real non-linear coil currents  $\underline{i}_{Coils}(t)$  and field strengths is considered in the Ampère's circuital law [7].



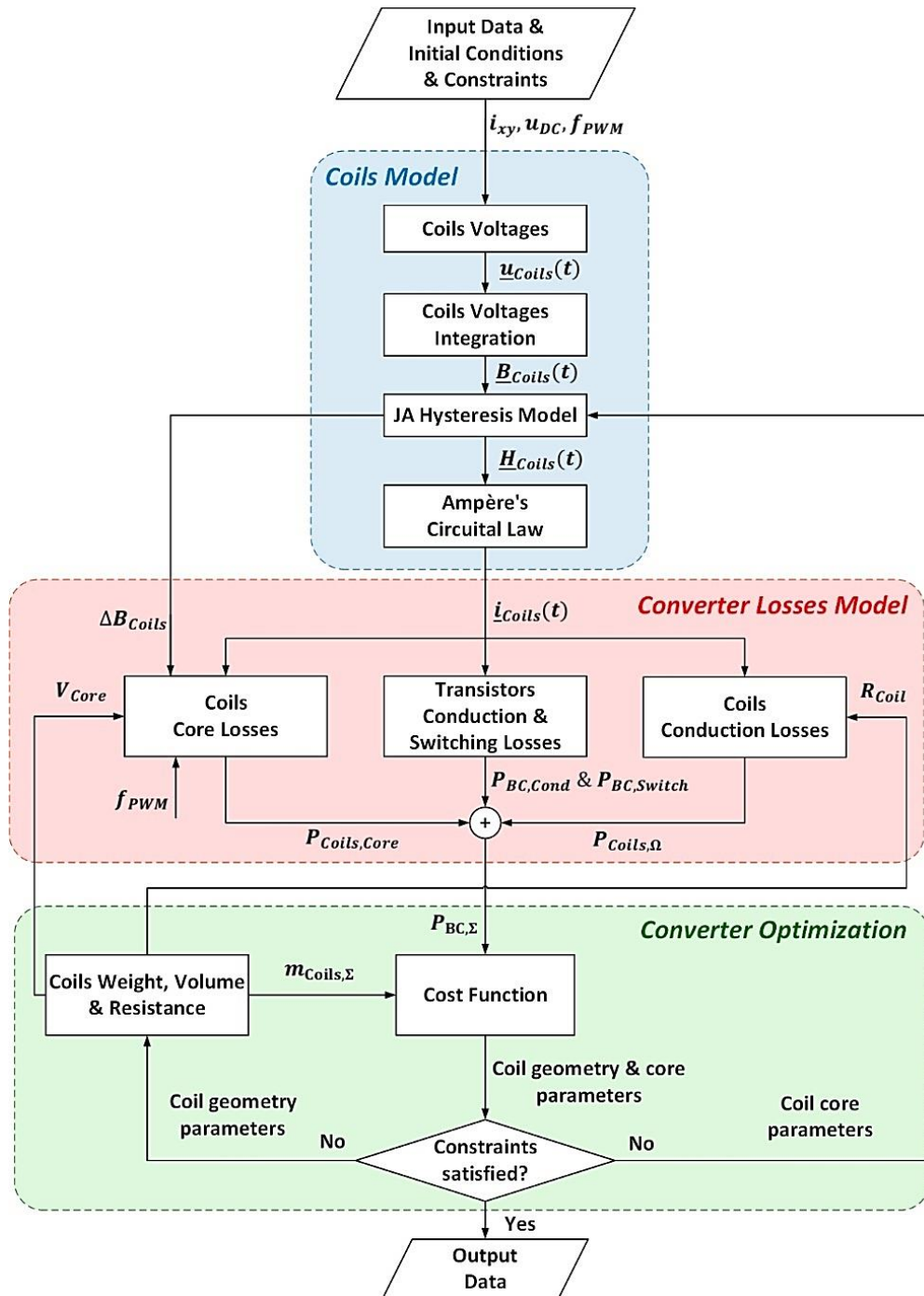


Fig. 27. Flowchart of Multiphase Interleaved DC-DC Converters Optimization [7].

The second stage describes the total converter losses based on the information of real non-linear coils currents, the magnetic flux, coil geometry and transistor parameters. The third stage performs the converter optimization minimizing the coils weight and size as well as the total converter losses and switching ripple of the output current. If necessary, the required optimal solution of coil parameters can be obtained from the given specific catalogue of materials for example from [104].

## 4.2 Optimization of Three-Phase Interleaved Converter with Toroid Coil

This Chapter will present the implementation of the above described optimization algorithm for a three-phase interleaved buck converter with toroid coils. Moreover, the proposed optimization principle can be applied to any coil geometry, any phase interleaved converter number and for converters with magnetically coupled coils.

### 4.2.1 Toroid Coil Geometry

Inductor coils are the most massive element in DC-DC converters and used for smoothing current ripple in them. Its weight and losses increase with rated coil current. Inductor coils can be generally classified into coils with (ferromagnetic-core) and without ferromagnetic core (air-core inductor) [96]. Air-core coils are more stable in use due to constant and independent of current inductance behavior [94]. However, they have substantial dimensions and high number of turns for high inductance that increases the wire resistance and leads to high coil losses at high currents. Considering these disadvantages, the air-core coil design according to [94] is well suited for systems with a low rated current and very high switching frequencies. The ferromagnetic core increases the core inductance and makes it possible to achieve a higher rated current. The inductance behavior in the ferromagnetic-core coil is non-linearly dependent on coil current. Moreover, the coil iron losses are also non-linearly dependent on current ripples and frequency. It means that the coil optimization without consideration of these non-linear effects can lead to coil saturation and loss of inductive properties. There are four main types of ferrite core geometries: toroidal core, profile core, E-core and pot-core [96]. However, according to the process of laying wires in the core the toroidal core presented in Fig. 28 is more optimal, because a toroid form allows to concentrate the maximum magnetic field density in the wire.

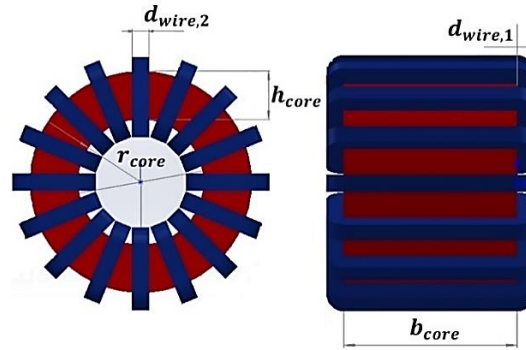


Fig. 28. Toroidal Core with Optimization Parameters.

In case of using the toroidal coils with rectangular wire in the converter, the required core optimization parameters are the inner core radius  $r_{core}$ , core width  $b_{core}$ , core height  $h_{core}$ , wire width  $d_{wire,2}$ , wire height  $d_{wire,1}$  and number of turns  $w_{coil}$  [96]. The length of the wire  $l_{wire}$  and core  $l_{core}$  as well as cross-section area of the wire  $A_{wire}$  and core  $A_{core}$  can be found as

$$\begin{aligned}
 l_{wire} &= w_{coil} (2(h_{core} + b_{core} + 2d_{wire,1}) - d_{wire,1}(4 - \pi)) \\
 l_{core} &= 2\pi(r_{core} + 0.5h_{core}) \\
 A_{wire} &= d_{wire,1}d_{wire,2} \\
 A_{core} &= b_{core}h_{core}.
 \end{aligned} \tag{4.3}$$

Then the total weight of three coils  $m_{coils,\Sigma}$  can be calculated as a sum of wire weight  $m_{wire}$  and a core mass  $m_{core}$  as

$$\begin{aligned}
 m_{wire} &= \rho_{wire} l_{wire} A_{wire} \\
 m_{core} &= \rho_{core} l_{core} A_{core} \\
 m_{Coils,\Sigma} &= 3(m_{core} + m_{wire}).
 \end{aligned} \tag{4.4}$$

As it can be seen, the total coils weight is a function of  $r_{core}$ ,  $b_{core}$ ,  $h_{core}$ ,  $d_{wire,2}$ ,  $d_{wire,1}$  and  $w_{Coil}$  that should be optimized. Thus, the optimization algorithm allows to achieve the minimal coil weight as well as minimal converter losses. For this purpose, the following requirements and constraints must be considered:

- the wire must occupy the entire core space in one layer to achieve the maximum efficiency and minimum weight as  $w_{Coil} d_{wire,2} \leq 2\pi(r_{core} - d_{wire,1})$ ;
- the optimal integer number of turns should give enough inductance to keep the current ripples in the minimal range;
- the coil inductance should decrease minimally with increasing of coil current in its rated range to prevent the core saturation and large current ripples;
- the thickness of the wire should be large enough to achieve the minimal resistance value, but it is necessary to consider the skin effect, which can increase the resistance at high frequencies;
- transistors overvoltage during switching time, switching and conduction losses must also be taken into consideration.

#### 4.2.2 Circuit Operations

A three-phase interleaved buck converter is shown in Fig. 29. Three buck converter phases operate with a switching frequency  $f_{bc} = f_{PWM}/3$  and the angle shift  $2\pi/3$  rad [92]. In terms of values of the input voltage  $u_{DC}$ , input current  $i_{DC}$ , output voltage  $u_{out} = u_{DC} D_{bc}$  and output current  $i_{xy}$ , the converter circuit operation is similar to a single-phase buck converter described in Chapter 3.5.2. However, phases switching frequencies and the coils currents  $\underline{i}_{Coils} = [i_{Coil,1} \ i_{Coil,2} \ i_{Coil,3}]^T$  flowing through them will be three times less for the same value of the average output current  $i_{xy,a}$ , its ripples  $\Delta i_{xy}$  and coil inductance  $\underline{L}_{Coils} = [L_{Coil,1} \ L_{Coil,2} \ L_{Coil,3}]^T$ . As it can be seen from Fig. 29, the coil inductance value has a relation to coil current, that should be considered in the coil mathematical model [96].

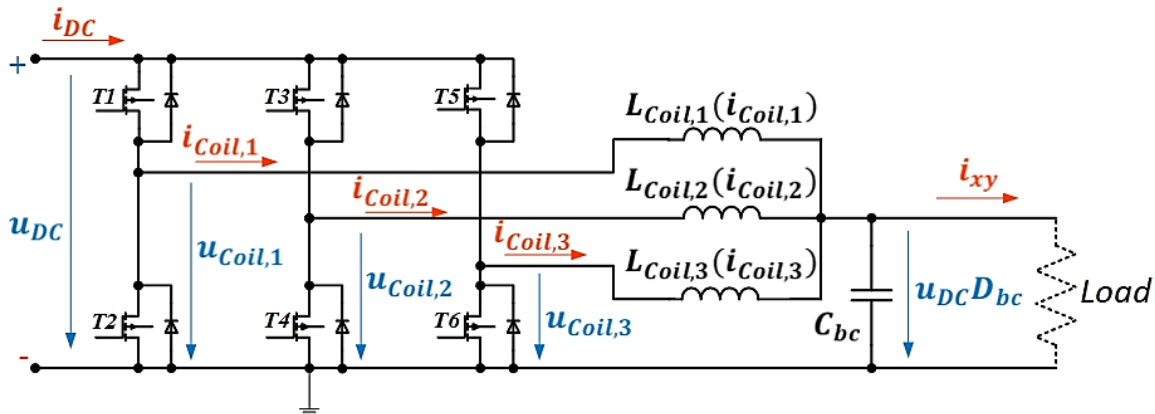


Fig. 29. Three-Phase Interleaved Buck DC-DC Converter.

If the switching frequency  $f_{PWM}$  is fixed, the output voltage  $u_{out}$  is controlled by adjusting the duty cycle ratio  $D_{bc}$ . The coil voltages  $\underline{u}_{Coils} = [u_{Coil,1} \ u_{Coil,2} \ u_{Coil,3}]^T$  have two states when upper switches T1, T3 and T5 are open and closed. Lower transistors (T2, T4 and T6) can be described with a

complement operation of the upper transistors. For any number of phases in the multilevel interleaved buck converter, the highest phase current as well as output current ripples correspond to the duty cycle ratio equal to 0.5 [7],[92]. Thus, to simplify the optimization model, the cycle ratio  $D_{bc}$  can be taken equal to 0.5. Considering that  $\tau$  is time between 0 and  $T_{bc} = \frac{1}{f_{bc}}$ , it is possible to find the relationship between coil voltages and the input supply dc voltage  $u_{DC}$  as

$$\begin{aligned} u_{Coil,1}(\tau) &= \begin{cases} u_{DC} - u_{out}, & \tau \leq \frac{T_{bc}}{2} \\ -u_{out}, & \text{otherwise} \end{cases} \\ u_{Coil,2}(\tau) &= \begin{cases} u_{DC} - u_{out}, & \frac{T_{bc}}{3} < \tau \leq \frac{T_{bc}}{6} \\ -u_{out}, & \text{otherwise} \end{cases} \\ u_{Coil,3}(\tau) &= \begin{cases} -u_{out}, & \frac{T_{bc}}{6} \leq \tau < \frac{2T_{bc}}{3} \\ u_{DC} - u_{out}, & \text{otherwise.} \end{cases} \end{aligned} \quad (4.5)$$

The current flowing in the coil windings generates a magnetic flux, which flows vertically through a surface of a closed core with area  $A_{Core}$  and can be described with a magnetic flux density. The induction law shows the relationship between the magnetic flux density of three coils  $\underline{B}_{Coils} = [B_{Coil,1} \ B_{Coil,2} \ B_{Coil,3}]^T$  and coil voltages  $\underline{u}_{Coils}$  as a function of time  $t$  between 0 and  $T_{bc}$

$$\underline{B}_{Coils}(t) = \underline{B}_{Coils,0} + \frac{1}{w_{Coil} \cdot A_{Core}} \int_0^t \underline{u}_{Coils}(\tau) d\tau \quad (4.6)$$

where  $w_{Coil}$  is the number of turns and  $\underline{B}_{Coils,0} = [B_{1,0} \ B_{2,0} \ B_{3,0}]^T$  is initial conditions of the magnetic flux density in three coils [96]. The Jiles – Atherton model describes the magnetization curve  $B_M(H)$  of a core material shown in Fig. 30 and represents the general relationship between the magnetic flux density and the field strength  $\underline{H}_{Coils} = [H_{Coil,1} \ H_{Coil,2} \ H_{Coil,3}]^T$

$$\underline{B}_{Coils}(t) = \mu_0 M_{Coils,s} \left(1 - \frac{x_{Core}}{H_{Coils}(t)}\right) \quad (4.7)$$

where  $x_{Core}$  is the material constant,  $M_{Coils,s}$  is the saturation magnetization and  $\mu_0$  is the permeability of free space [97],[98].

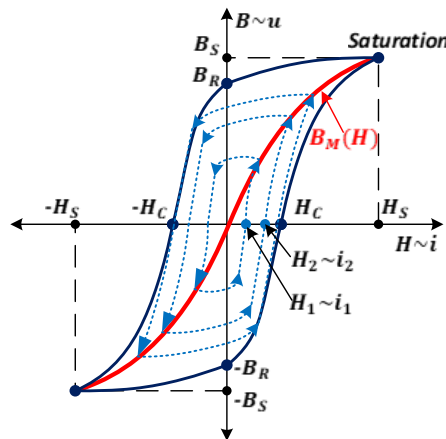


Fig. 30. Hysteresis Loop and Magnetization Curve  $B_M(H)$ .

Usually the manufacturers of magnetic materials propose the more accurate description of the magnetization curve based on the approximation of the measured results, for example, according to [104], the magnetization curve can be described as

$$\underline{B}_{Coils}(\underline{H}_{Coils}) = \left( \frac{x_1 + x_2 \cdot \underline{H}_{Coils}(t) + x_3 \cdot \underline{H}_{Coils}^2(t)}{1 + x_4 \cdot \underline{H}_{Coils}(t) + x_5 \cdot \underline{H}_{Coils}^2(t)} \right)^{x_6} \quad (4.8)$$

where  $\underline{x}_{1..6} = [x_1 \ \dots \ x_6]$  are the material coefficients calculated based on the measured values [104]. For three-phase interleaved converter the relationship between the coils currents  $\underline{i}_{Coils}$  and the field strength can be described with the flow law as

$$\underline{i}_{Coils}(t) = \frac{l_{Core} \cdot \underline{H}_{Coils}}{w_{Coil}} \quad (4.9)$$

where  $l_{Core}$  is the core length [96]. The coil inductance  $\underline{L}_{Coils}$  is non-linear and is a function of current

$$\underline{L}_{Coils}(t) = \frac{w_{Coil} A_{Core} \cdot \underline{B}_{Coils}(t)}{\underline{i}_{Coils}(t)} \quad (4.10)$$

Average values of  $B_{Coils,a}$  and  $H_{Coils,a}$  are constant for each of the three phases and can be obtained as a function of the average output current  $i_{xy,a}$  as

$$H_{Coils,a} = \frac{1}{3} \cdot \frac{w_{Coil} i_{xy,a}}{l_{Core}} \quad (4.11)$$

$$B_{Coils,a} = \mu_0 M_{Coils} \left( 1 - \frac{a_{Core}}{H_{Coils,a}} \right) \text{ or } B_{Coils,a} = \left( \frac{x_1 + x_2 H_{Coils,a} + x_3 H_{Coils,a}^2}{1 + x_4 H_{Coils,a} + x_5 H_{Coils,a}^2} \right)^{x_6} .$$

The magnetic flux density minimum and maximum values as well as its difference  $\Delta B_{Coils}$  can be estimated according to (4.6) as

$$\Delta B_{Coils} = \frac{B_{Coils,max} - B_{Coils,min}}{2}$$

$$B_{Coils,min} = B_{Coils,a} - \frac{1}{w_{Coil} \cdot A_{Core}} \int_0^{\frac{T_{bc}}{2}} u_{Coils,1}(\tau) d\tau \quad (4.12)$$

$$B_{Coils,max} = B_{Coils,a} + \frac{1}{w_{Coil} \cdot A_{Core}} \int_0^{\frac{T_{bc}}{2}} u_{Coils,1}(\tau) d\tau$$

Initial conditions of the magnetic flux density in three coils  $\underline{B}_{Coils,0} = [B_{1,0} \ B_{2,0} \ B_{3,0}]^T$  can be obtained as

$$B_{1,0} = B_{Coils,min}$$

$$B_{2,0} = B_{Coils,min} + \frac{1}{w_{Coil} \cdot A_{Core}} \cdot \int_0^{\frac{T_{bc}}{3}} u_{Coils,2}(\tau) d\tau \quad (4.13)$$

$$B_{3,0} = B_{Coils,min} + \frac{1}{w_{Coil} \cdot A_{Core}} \cdot \int_0^{\frac{2T_{bc}}{3}} u_{Coils,3}(\tau) d\tau$$

The output current  $i_{xy}(t)$  is the sum of the three non-linear coils currents

$$i_{xy}(t) = i_{Coil,1}(t) + i_{Coil,2}(t) + i_{Coil,3}(t) \quad (4.14)$$

and its ripples  $\Delta i_{xy} = i_{xy}\left(\frac{T_{bc}}{2}\right) - i_{xy}(0)$  can be calculated as a difference between the maximum and the minimum current values. The maximum output current is corresponded to the time point equal to the half of the switching period. The minimum – to the time points 0 or  $T_{bc}$ . Similarly, the current ripple of coils currents

$$\Delta i_{Coils} = i_{Coils,max} - i_{Coils,min} = i_{Coil,1}\left(\frac{T_{bc}}{2}\right) - i_{Coil,1}(0) \quad (4.15)$$

must be the same in the ideal system with identical coil resistances and can be found as a difference between current values in the switch-on and switch-off points. The average values of three coils currents are three times lower than the average value of the output current in the ideal converter system. The mathematical model of interleaved converter with different number of phases should be changed depending on the number of phases and phase shift. However, the description principle remains the same. The equations chain  $\underline{u}_{Coils}(\tau) \rightarrow \underline{E}_{Coils}(t) \rightarrow \underline{H}_{Coils}(t) \rightarrow \underline{i}_{Coils}(t)$  based on the Jiles – Atherton model allows to obtain the real non-linear coils currents and find the optimal coil geometry for the required converter power.

### 4.2.3 Converter Losses Model

**The total losses in the power electronic** can be divided into conduction and switching losses. Conduction losses exist due to the drain-source resistance  $R_{DS}$  in the transistor and can be calculated with very good accuracy in analogy to the resistive losses of a motor phases [100] as

$$P_{BC,cond} = \frac{R_{DS}}{T_{bc}} \int_0^{T_{bc}} \left( i_{Coil,1}^2(t) + i_{Coil,2}^2(t) + i_{Coil,3}^2(t) \right) dt. \quad (4.16)$$

The switching losses are produced only during the switch-on and off times of the transistor and increase with increasing of the switching frequency. In contrast with a power conduction loss, the switching losses are more difficult to express mathematically as they vary with many factors. During the switching-on time, a transient process takes place, wherein the transistor drain-source current is increased from 0 to  $i_{Coils,min}$  and the voltage drops from  $u_{DC}$  to  $R_{DS}i_{xy,a}/3$ . Thus, the switching-on time can be divided into the voltage drop time  $t_{fu}$  and the current rise time  $t_{ri}$ . The voltage drop time  $t_{fu}$

$$t_{fu} = \frac{t_{fu1} + t_{fu2}}{2}$$

$$t_{fu1} = (u_{DC} - R_{DS}i_{Coils,min})R_G \frac{C_{GD1}}{(U_{DR} - U_{plateau})} \quad (4.17)$$

$$t_{fu2} = (u_{DC} - R_{DS}i_{Coils,min})R_G \frac{C_{GD2}}{(U_{DR} - U_{plateau})}$$

is depended on the variable gate-drain capacity  $C_{GD}$  and can be divided into two intervals  $t_{fu1}$  and  $t_{fu2}$  as well as the gate-drain capacity value can be conditionally divided into two segments:  $C_{GD1}$  corresponded to the supply voltage  $u_{DC}$  and  $C_{GD2}$  – to  $u_{DC}/2$ , where  $U_{plateau}$  is the gate plateau voltage and  $U_{DR}$  is the driver output voltage [100]. By the same principle, the switch-off time consists of the voltage rise time  $t_{ru}$  and the current drop time  $t_{fi}$ . During  $t_{fi}$  the drain-source voltage remains constant and the drain current decreases from  $i_{Coils,max}$  to 0. Again, according to the gate drain capacity the voltage rise time can be divided into  $t_{ru1}$  and  $t_{ru2}$  as

$$\begin{aligned}
 t_{ru1} &= (u_{DC} - R_{DS}i_{coils,max})R_G \frac{C_{GD1}}{U_{plateau}} \\
 t_{ru2} &= (u_{DC} - R_{DS}i_{coils,max})R_G \frac{C_{GD2}}{U_{plateau}} \\
 t_{ru} &= \frac{t_{ru1} + t_{ru2}}{2}.
 \end{aligned} \tag{4.18}$$

The real model of the transistor contains the stray inductance  $L_{str}$ . The stray inductance together with the connection and cable stray inductances causes overvoltage that leads to additional losses and can damage the power electronics [100]. Thus, the overvoltage during the switching-on time  $U_{ind\_on}$  and switching-off time  $U_{ind\_off}$  can be estimated with a current difference and switching time as

$$\begin{aligned}
 U_{ind\_on} &= \frac{L_{str} \cdot i_{coils,min}}{t_{ri}} \\
 U_{ind\_off} &= \frac{L_{str} \cdot i_{coils,max}}{t_{fi}}.
 \end{aligned} \tag{4.19}$$

The current rise  $t_{ri}$  and drop times  $t_{fi}$  depend on the gate resistance  $R_G$ . The switch-on energy losses  $E_{onM}$  as well as the shutdown energy losses  $E_{offM}$  and the energy loss in the diode due to the inverse recovery effect  $E_{onD}$

$$\begin{aligned}
 E_{onM} &= \left(\frac{i_{coils,min}}{2}(t_{fu} + t_{ri}) + Q_{rr}\right)(u_{DC} + U_{ind\_on}) \\
 E_{offM} &= \frac{1}{2}(u_{DC} + U_{ind\_off}) \cdot i_{coils,max} \cdot (t_{ru} + t_{fi}) \\
 E_{onD} &= \frac{1}{4} \cdot Q_{rr} \cdot (u_{DC} + U_{ind\_on})
 \end{aligned} \tag{4.20}$$

can be calculated with switching times, where  $Q_{rr}$  represents the reverse recovery charge [100]. The necessary parameters for this calculation as:  $C_{GD1}$ ,  $C_{GD2}$ ,  $U_{DR}$ ,  $U_{plateau}$ ,  $Q_{rr}$ ,  $t_{ri}$ ,  $t_{fi}$  and  $R_G$ , are usually described in the datasheet of a transistor. The switching losses  $P_{BC,Switch}$  of a three-phase interleaved buck converter are the product of the circuit energy losses and the converter switching frequency  $f_{PWM}$

$$P_{BC,Switch} = (E_{onM} + E_{offM} + E_{onD})f_{PWM}. \tag{4.21}$$

The described above mathematical model of the switching losses cannot give a very accurate losses estimation due to linearization of the transient process of the current and voltage in switching times. However, for solving the converter optimization problem, its accuracy is enough.

**The total losses of coils** consist of iron and resistive losses. The resistive losses in the three coils according to Joule's law are the result of the coil winding resistance  $R_{Coil}$  depended on the wire geometry and electrical power

$$\begin{aligned}
 R_{Coil} &= \rho_{Cu} l_{wire} / A_{wire} \\
 P_{Coils,\Omega} &= \frac{R_{Coil}(\vartheta)}{T_{bc}} \int_0^{T_{bc}} (i_{Coil,1}^2(t) + i_{Coil,2}^2(t) + i_{Coil,3}^2(t)) dt,
 \end{aligned} \tag{4.22}$$

where  $\rho_{Cu}$  is a specific electrical resistance of the wire material [96]. The temperature and the skin effect influence on the wire resistance can be included in the mathematical model according to (3.12). Iron or core losses consist of hysteresis and eddy current losses and are dependent on switching frequency and magnetic flux density. Core losses can be estimated as

$$P_{Coils,Core} = x_7 \Delta B_{Coils}^{x_8} f_{bc}^{x_9} \quad (4.23)$$

where  $\underline{x}_{7..9} = [x_7 \quad x_8 \quad x_9]$  are material coefficients, or based on the Jiles – Atherton hysteresis model

$$\frac{dM_{Coils}(t)}{H_{Coils}(t)} = \frac{M_{Coils,S}}{x_{Core}} \left[ 1 - \left( \coth \frac{H_{Coils}(t)}{x_{Core}} \right)^2 + \left( \frac{x_{Core}}{H_{Coils}(t)} \right)^2 \right]$$

$$\underline{B}_{Coils}(t) = \mu_0 (\underline{M}_{Coils}(t) + \underline{H}_{Coils}(t)) \quad (4.24)$$

$$P_{Coils,Core} = f_{bc} V_{Core} \int \underline{B}_{Coils}(t) d\underline{H}_{Coils}(t),$$

where  $\underline{M}_{Coils}$  is magnetization of three coils and  $V_{Core}$  is a core volume [97],[98],[104]. However, the core losses in the coils are lower in comparison to the other. So, equation (4.23) may be used for the system simplification. To summarize, the total power losses of a three-phase interleaved DC-DC converter can be included to the objective function (4.1) according to (4.2), (4.16), (4.21) and (4.23). The above listed equation shows that total convertor losses as well as coils weight are the function of the required coil parameters and given switching frequency, dc input voltage and average output current. Thus, the required coil parameters combined in the objective function:  $r_{core}$ ,  $b_{core}$ ,  $h_{core}$ ,  $d_{wire,2}$ ,  $d_{wire,1}$ ,  $w_{Coil}$ , and  $\underline{x}_{1..9} = [\underline{x}_{1..6} \quad \underline{x}_{7..9}]$  can be found based on the minimization of the total converter losses as well as the total coils weight considering the optimization constraints, converter operation power and the given parameters of power electronic.

### 4.3 Optimization Results of Three-Phase Interleaved Buck Converter

This Chapter will present the converter optimization results based on the mathematical model described in Chapter 4.2. The algorithm has been implemented in a Maple software using the DirectSearch package based on CDOS (Conjugate Direction with Orthogonal Shift) method, which provides an optimization of the objective function with a non-standard form and considers any constraints and conditions for setting variables. Compared to other optimization methods, such as Powell, Brent or Quadratic, the CDOS makes the optimization faster due to use of only the constraint violation. Nevertheless, it is necessary to set the initial values as close as possible to the optimum and select the optimization area in order to accelerate the calculation process.

#### 4.3.1 Input Parameters

The slotless air gap winding technology allows to design wheel hub motors with high gravimetric power density of about 2kW/kg [18]. Due to the low phase inductance, the control of air gap winding wheel hub motors requires either high switching frequencies or special control concept described in Chapter 3.5, which consists of a six-step square-wave commutation and source current control by means of a DC-DC buck converter. The high motor power of about 5.1 kW requires an appropriate converter power. Often enough the conventional market offers high-power DC-DC converters that do not satisfy weight requirements and may nullify the advantage of the air gap winding design. Thus, the power electronic must satisfy the required drive performance and its weight must be as low as possible to maintain a high gravimetric power density of the motor. A mathematical model of a three-phase interleaved buck converter with toroid coils has been developed to find the optimal coils parameters for the minimal converter weight as well as the minimal converter losses. The three-phase interleaved buck converter has been optimized for 48V supply voltage, 75 kHz switching frequency and 100A rated average output current the other parameters required for optimization are given in TABLE VIII.



TABLE VIII. PARAMETERS OF THREE-PHASE INTERLEAVED BUCK CONVERTER

Symbol	Description	Value	UOM
$C_{GD1}$	Gate Drain Capacitance	300	$\mu F$
$C_{GD2}$	Gate Drain Capacitance	5	$nF$
$R_{DS}$	Drain-Source on-state Resistance	2	$m\Omega$
$U_{DR}$	Driver Output Voltage	15	V
$U_{plateau}$	Gate Plateau Voltage	4.4	V
$R_G$	Gate Resistance	6	$\Omega$
$t_{ri}$	Current Rise Time	30	ns
$t_{fi}$	Current Fall Time	30	ns
$Q_{rr}$	Reverse Recovery Charge	632	nC
$t_{rr}$	Reverse Recovery Time	206	ns
$u_{DC}$	DC Voltage	48	V
$f_{PWM}$	Switching Frequency	75	kHz
$i_{xy,a}$	Rated Average Output Current	100	A
$r, h, b_{core}$	Core Geometry Parameters for Optimization	Magnetics Catalog [104]	
$x_{1..6}$	Magnetization Curve Coefficients for Optimization	Magnetics Catalog [104]	
$x_{7,9}$	Iron Losses Material Coefficients for Optimization	Magnetics Catalog [104]	

The optimal core geometry parameters:  $r_{core}$ ,  $b_{core}$  and  $h_{core}$  have been selected by means of optimization algorithm from the Magnetics catalog [104]. Moreover, Magnetics catalog offers a wide range of material properties with different coefficients of magnetization curve and iron losses. Thus, in addition to selection of core geometry parameters, the optimal material has been found in the catalog with  $B_M(H)$  coefficients combined with losses coefficients in  $x_{1..9}$ . The wire parameters for optimization are:  $d_{wire,2}$ ,  $d_{wire,1}$  and the number of turns  $w_{Coil}$ .

### 4.3.2 Optimization Results and Validation

The optimal dependence between the three coils weight and the total converter losses has been found by changing the weight coefficients  $q_1$  and  $q_2$ . Fig. 31 shows these dependencies between the converter total losses and the weight (left, above), the coils current ripples and the weight (left, middle), as well as with the converter total losses and the current ripples (left, below), and between the coils current ripples and the optimized coil parameters (right). From the matrix with optimization results, a more suitable spectrum of the coil parameters (circled in red) of core material High Flux 60 $\mu$  has been chosen [104]. Based on these optimization results and input parameters given in TABLE VIII. a prototype of three-phase interleaved buck converters with three toroid coils shown in Fig. 32 (middle) has been designed. The converter prototype has a very low weight – 0.16kg and 40W total losses with the average rated output current. In addition, a three-phase interleaved buck converter with three toroid coils shown in Fig. 32 (left) has also been optimized and designed, which is operated with 75kHz, 60V, 150A and has a coils weight equal to 0.5kg and 150W total losses.

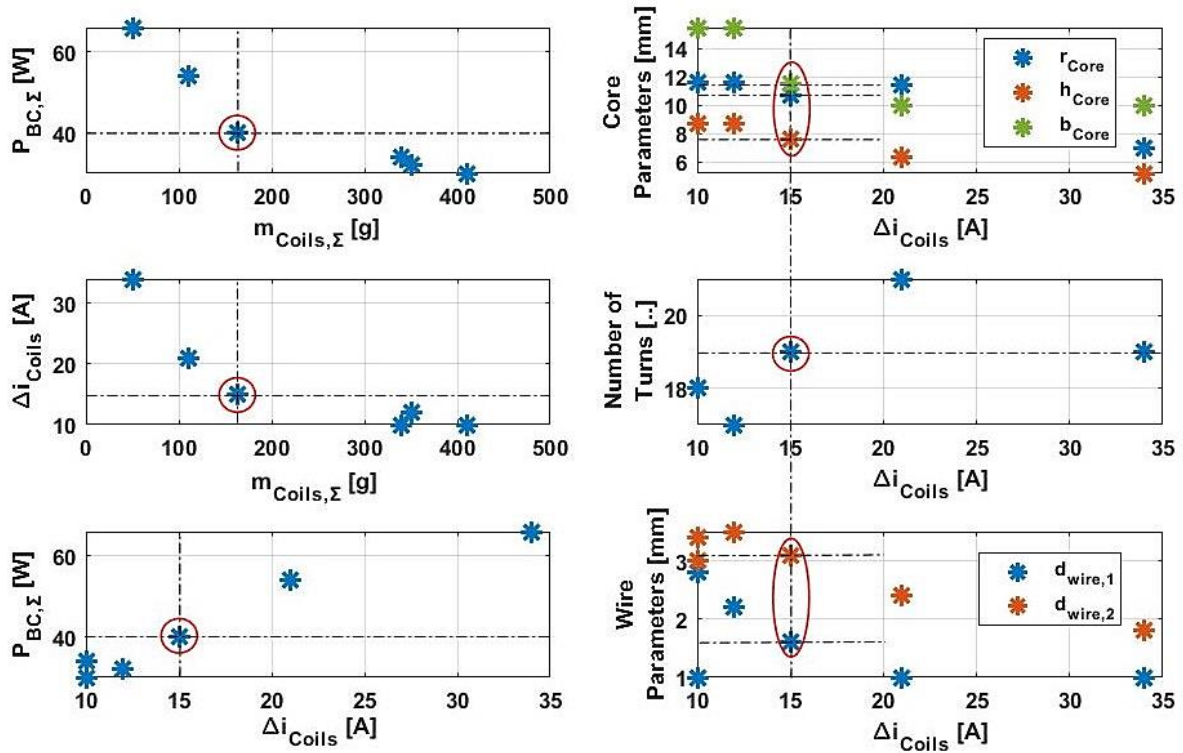


Fig. 31. Results of three-phase interleaved buck converter optimization.

The non-optimized coil in comparison to the optimized coils of the first and the second prototypes are shown together in Fig. 32 (right), where the optimized coil for the first converter prototype (3) operated with rated average current 50A has weight equal to 53g, for the second prototype (2) – 23g, 33A, and the non-optimized coil with the same current and inductance range has a weight equal to 350g.

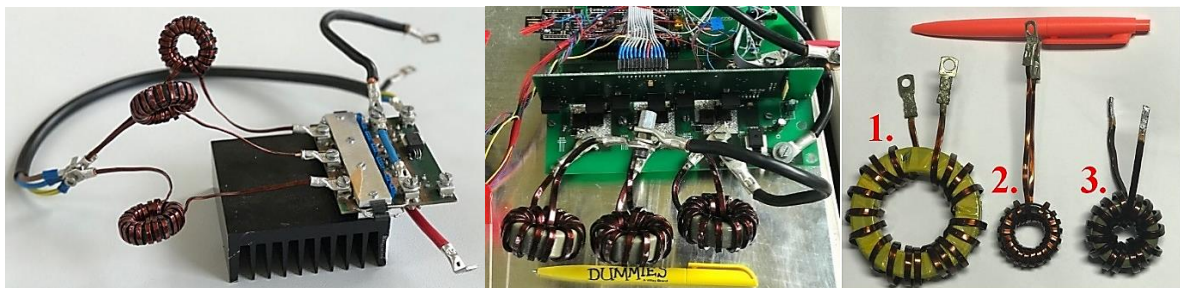


Fig. 32. Two prototypes of a three-phase interleaved buck converter (left, middle) and comparison of optimized and non-optimized coils (right).

The behavior of the three theoretical and measured converter currents as well as the output rated current are shown in Fig. 33. The experimental results quite accurately coincide with theoretical calculations. In addition, the converter loss mathematical model has also been validated by measurements with variation of average output current  $i_{xy,a}$  from 20A to the rated value. The experimental and theoretical results of the converter total (left, above), conduction (left, below), switching (right, below) and coils (right, above) losses are shown in Fig. 34. The practical measurements of the converter losses show the correspondence to the theoretical model.

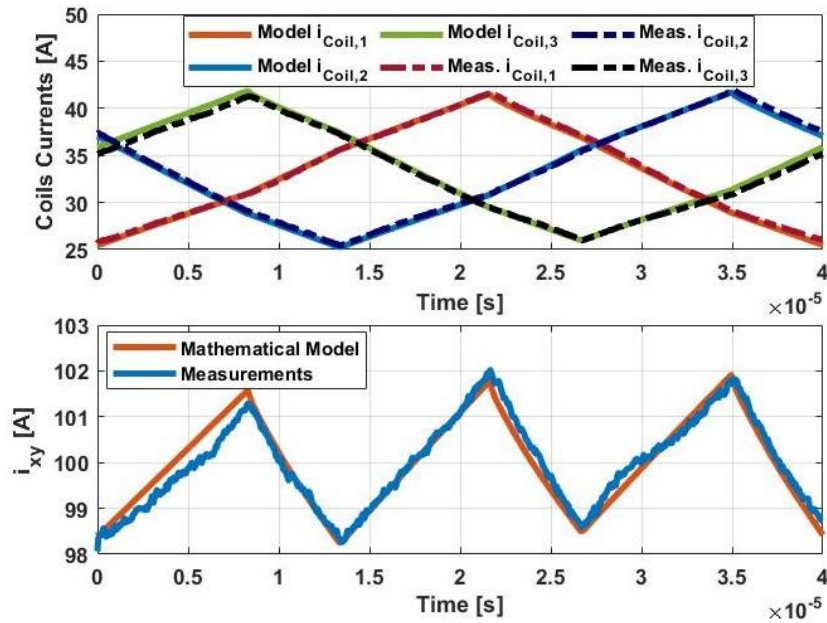


Fig. 33. Measured and Simulated Currents and Output Current of the Three Coils.

The largest discrepancy is observed in calculation of switching losses due to linearization of the transient process in transistors during switching times. However, with an increase of the output current to the rated value, the difference between the theoretical and measured results becomes minimal.

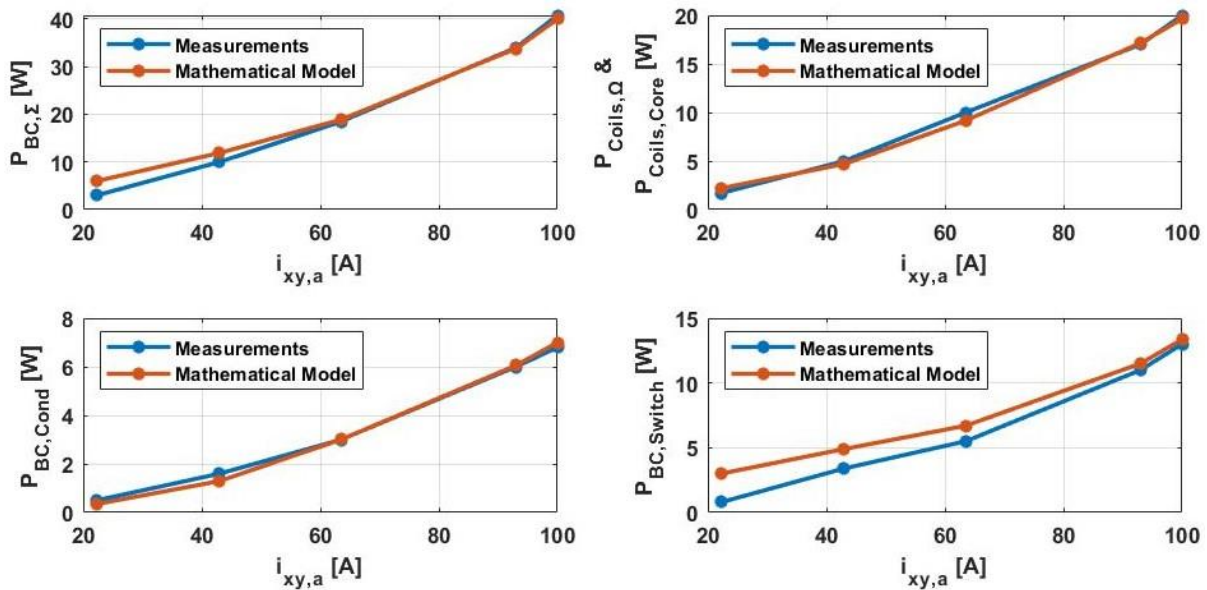


Fig. 34. Measured and Calculated Converter Total, Conduction, Switching and Coils Losses.

Thus, the optimization algorithm of a three-phase interleaved DC-DC buck converter provides an optimal solution by reduction of weight as well as of the total losses in a converter. The algorithm considers the electromagnetic properties of inductor coils and is based on the power electronics parameters and required operating conditions of the converter such as supply voltage, rated output current and switching frequency. The algorithm is based on the non-linear mathematical model of inductor coils determined by the chain structure: coils voltages – magnetic inductions – magnetic field

intensities – coils currents that makes it possible to describe the real inductance behavior in the coils, prevent core saturation and find the optimal coils geometry to obtain the minimal converter weight and losses. In addition, the proposed algorithm can be combined with any kind of coil geometry, allows to take into consideration the air gap in the core and can also be adapted for magnetically coupled coils. In summary, several areas can be distinguished for applying this algorithm:

- low inductance PMSM or BLDC control with six-step commutation and without the use of high switching frequency;
- supply voltage or current control from the storage battery in compact and portable systems, for example in an e-Scooter, e-Bike, e-Boot or electric car;
- PMSM or BLDC motor optimization by their total weight and losses.

Results of the air gap winding PM motor control by means of a three-phase interleaved buck converter described in this chapter combined with the six-step commutation will be presented in Appendix A. However, the most effective solution for that purpose based on the high switching frequency of B6-brifge will be proposed in the next chapter.

## 5. Combined Optimal Torque and Modal Current Control

Essential requirements of PM motors control are reliability, energy efficiency and simplicity of implementation. Conventional vector control methods satisfy these requirements in case of their implementation for standard PMSMs with high phase inductance due to the presence of slots and a high volume of winding copper. The new air gap and the combined winding design of a PM motor invented by Otto-von-Guericke University and described in [1]-[22] conditioned by the absence of slots, a small amount of copper and a large number of pole pairs. On the one hand, this leads to a decrease in the weight of the motor while maintaining or even increasing its power. On the other hand, it reduces the value of phase inductance and presents challenges in relation to motor control. Thus, a motor low phase inductance, large number of poles and in the same time high motor power make it necessary to take into account the following requirements for the control system, which previously have not played an important role in the control systems of standard electric machines:

- Simplicity of implementation. The motor low inductance requires a high switching frequency to implement the minimum current switching ripples. It means, that any common low-cost microcontroller should be able to implement the control loop with a very small step size in the range of  $10\mu\text{s}$  corresponding to a high switching frequency.
- Stability, reliability and high system dynamics. Phase current measurements should be carried out with an adequate accuracy. The current controller must compensate all feedback errors without significant overshoots. A high number of pole pairs also requires accurate angle measurement.
- Ability to motor losses and torque ripple optimization. The rotor magnets properties and geometry as well as the width of the air gap lead to non-sinusoidal form of the B-Field in the air gap, which, according to the torque equation (3.8) leads to torque fluctuations and additional motor losses. Modern vector control approaches according to [60]-[80] can solve these problems involving an observer. However, these methods significantly complicate the structure of the control algorithm and do not meet the first requirement.

The other commonly used control methods for PMSM or BLDC as scalar based or commutation control cannot guarantee a high step response or minimal torque and current ripples. To accomplish these tasks for air gap winding and combined winding design of PM motors, new Combined Optimal Torque and Modal Current Control (OTMIC) was developed in accordance with the features of a new type of electric motor and able to minimize the main disadvantages of conventional methods in case of using for low inductance and high power PMSM. OTMIC control generates optimal phase currents for arbitrary harmonic B-Field to minimize the torque ripples or motor losses.

### 5.1 Optimal Torque Control for Minimal Motor Losses

Motor losses minimization or, equivalently expressed, motor efficiency maximization according to the given torque  $T_{Ref}$  and the motor speed  $\omega_M$  is a typical design requirement of a control system for an electrical motor. In conventional vector control approaches based on trigonometric transformations described in Chapter 3 or in [46]-[80], this task can be accomplished by adding an observer to the system. However, from the point of view of a high-frequency control, this solution requires a powerful type of a microcontroller because of a very short interval of the program cycle. In addition, Space Vector

Representation described with equations (3.27)-(3.42) and based on the sinusoidal waveform of phase currents according to (3.27) in the case of a non-sinusoidal B-field waveform cannot be used to transform additional harmonics of B-Field to  $dq$  coordinate system with (3.40) in order to compensate them. To overcome this problem each additional B-Field harmonic from the equation (3.5) should be transformed to the  $dq$  coordinate system separately as was presented in [74]. This leads to additional inaccuracies and complicates the control algorithm. This chapter proposes a simple solution to this problem, without including an observer into the system. All calculations can be obtained offline and stored in the table according to the rotor electrical angle position, which reduces the computational process in one control cycle. According to (3.8) the electrical torque equation  $T_E$  can be expressed as

$$T_E = k_M [i_a(\varphi_e)B_a(b_k, \varphi_e) + i_b(\varphi_e)B_b(b_k, \varphi_e) + i_c(\varphi_e)B_c(b_k, \varphi_e)], \quad (5.1)$$

where  $b_k$  is a vector with harmonic coefficients of B-fields calculated using (3.5). The torque (5.1) shows, that adaptation of phase current waveforms with consideration of B-field harmonic spectrum is the key to PMSM torque control [4]-[7]. In other words, by making modifications in the current waveform taking into account (3.8), (3.18) and (5.1), it is possible to optimize a torque waveform or motor losses. It leads to the idea, that phase currents  $i(\varphi_e)$  similar to B-field can also be estimated as harmonic functions of an electrical angle  $\varphi_e$

$$i(\varphi_e) = \sum_k a_k \sin(k \cdot \varphi_e), \quad (5.2)$$

where  $\underline{a} = [a_1 \ a_2 \ \dots \ a_n]$  is a vector with phase current harmonic coefficients, and  $k$  is a coefficient number. Taking into account additional constraints according to (3.1)

$$a_3 = 0, \quad (5.3)$$

an average electrical torque

$$T_A = \frac{1}{2\pi} \int_0^{2\pi} T_E d\varphi_e = \frac{3}{2} k_M \sum_k a_k b_k \quad (5.4)$$

can be formulated by Fourier coefficients of phase current  $a_k$  and B-Field  $b_k$ . Total losses of a PMSM motor with air gap winding are described in more detail in Chapter 3.2. Briefly, it may be noted that averaged total losses of a PM motor with air gap or combined winding consist of ohmic and non-ohmic losses and can be expressed using (3.18).

Non-ohmic loss  $P_{no} = d \cdot \bar{\omega}_M^2 + c \cdot \bar{\omega}_M$  is a function of only the average angular speed in a pole pair segment [2], [12], [13]. In the same way as the average electrical torque, according to (3.11), (3.18) and (5.2) motor ohmic losses  $P_\Omega$  can be expressed by Fourier coefficients of phase currents  $a_k$  as

$$P_L = \frac{R_s}{2\pi} \sum_k a_k^2 + d \cdot \bar{\omega}_M^2 + c \cdot \bar{\omega}_M. \quad (5.5)$$

The given specification leads to the mathematical quadratic optimization problem for minimization of the motor losses cost function

$$\text{Min} = P_L(a_k) \quad \text{with constraint} \quad T_A(a_k, b_k) = T_{Ref} \quad (5.6)$$

for unknown parameters  $a_k$  of the phase current harmonics based on the given parameters  $b_k$  of the B-field. The solution of this optimization problem can be specified analytically, e.g. by combining the cost function and constraints in a Lagrange function

$$\mathcal{L}(a_k, \lambda) = \frac{R_s}{2\pi} \sum_k a_k^2 + d \cdot \bar{\omega}_M^2 + c \cdot \bar{\omega}_M + \lambda \left( \frac{3}{2} k_M \sum_k a_k b_k - T_{Ref} \right). \quad (5.7)$$

Solving the  $k + 1$  gradient equations in  $k + 1$  unknowns

$$\nabla_{a_k, \lambda} \mathcal{L}(a_k, \lambda) = 0 \quad (5.8)$$

leads to unknown coefficients of phase current harmonics

$$a_l = \frac{2 T_{Ref} b_l}{3 k_M \bar{b}^2} \quad (5.9)$$

with the sum of squares of selected harmonics of the B-field

$$\bar{b}^2 = \sum_m b_l^2 \quad (5.10)$$

and the selection indices

$$l = \{1, 5, 7, 11, 13, 17, 19, 23 \dots\}. \quad (5.11)$$

Remaining parameters of phase current harmonics are zero. Considering the selection indices  $l$  some harmonics of  $b_k - \{3, 9, 15 \dots\}$  will not contribute to current and torque waveforms. Thus, the optimal phase current waveform  $K_{opt,l}(\varphi_e)$  for motor losses minimization can be estimated for each electrical angle with optimal harmonics coefficients  $l$  as

$$K_{opt,l}(\varphi_e) = \sum_l a_l \sin(l \cdot \varphi_e), \quad (5.12)$$

The equation (5.9) shows, that the optimal current waveforms or, equivalently expressed, the optimal electrical torque waveform can be determined for each electrical rotor angle according to the harmonics of the B-field  $b_k$ , the motor geometric constant  $k_M$  and the given reference torque  $T_{Ref}$ . Thus, this approach guarantees the minimal motor losses for an arbitrary B-field, each demanded torque and regardless of the motor speed.

The design of an air gap or combined winding PM motor stems from the fact that B-field harmonic coefficients are nearly ideally constant and have minor sensitivity to temperature changes [2],[9]. This affords an opportunity for offline estimation of an optimal phase current waveform. Then, these results can be stored in the table as a function of the electrical angle, and this greatly simplifies the control loop calculation in a microcontroller. If necessary, temperature effects on the B-field harmonic coefficients and phase resistance  $R_s$  can be easily incorporated into the model and adapted online.

## 5.2 Optimal Torque Control for Minimal Torque Ripple

The presence of high-frequency components in the electromagnetic torque caused by a non-ideal back-EMF waveform and other factors leads to increase of noise and motor vibration and decrease of the motor efficiency. This means that the level of torque ripples is important indicators of the quality of electromechanical conversion. Consequently, generation of a given torque  $T_{Ref}$  with minimum torque fluctuations is another typical design requirement of a control system for an electrical motor. Electrical torque as a function of a current harmonic coefficient  $a_k$  can be expressed by inserting a phase current definition from (5.2) into the electrical torque equation (5.1) with the B-Field equation (3.5)

$$T_E = k_M \left[ \sum_k a_k b_k \sin^2(k\varphi_e) + \sum_k a_k b_k \sin^2\left(k\left(\varphi_e - \frac{2\pi}{3}\right)\right) + \sum_k a_k b_k \sin^2\left(k\left(\varphi_e - \frac{4\pi}{3}\right)\right) \right] \quad (5.13)$$

A torque ripple can be expressed as mean square excursion between the average torque  $T_A$  and the electrical torque  $T_E$  as

$$T_R^2 = \frac{1}{2\pi} \int_0^{2\pi} (T_E - T_A)^2 d\varphi_e. \quad (5.14)$$

The given equation leads to the mathematical optimization problem for minimization of torque ripples. In this scenario, unknown parameters for an optimal current waveform can be calculated by solving the optimization problem

$$\text{Min} = T_R^2 \quad \text{with constraint} \quad T_A = T_{Ref} \quad (5.15)$$

based on the given  $b_k$ . Using (5.4), (5.13) and (5.14), the optimization problem can be solved analytically in the same way as (5.6) by formulating the Lagrange function

$$\mathcal{L}(a_k, \lambda) = \frac{1}{2\pi} \int_0^{2\pi} (T_E - T_A)^2 d\varphi_e + \lambda \left( \frac{3}{2} k_M \sum_k a_k b_k - T_{Ref} \right), \quad (5.16)$$

calculating derivatives using (5.11) and solving the 1<sup>st</sup> order conditions.

In addition to this straightforward path, there is another approach that leads to simpler expressions and allows to express the solution more accurately. Starting from (3.5) and (3.8) for example 23 harmonics of electrical torque  $T_E$

$$\tau_k = \frac{1}{\pi} \int_0^{2\pi} T_E \cdot \cos(6k\varphi_e) d\varphi_e \quad (5.17)$$

can be determined and combined in vector

$$\underline{\tau} = \underline{A} \underline{a}_\tau \quad (5.18)$$

with matrix  $\underline{A}$

$$\underline{A} = \frac{2}{3} k_M \begin{bmatrix} 2b_1 & 2b_5 & 2b_7 & 2b_{11} & 2b_{13} & 2b_{17} & 2b_{19} & 2b_{23} \\ b_7 - b_5 & b_{11} - b_1 & b_{13} + b_1 & b_{17} + b_5 & b_{19} + b_7 & b_{23} + b_{11} & b_{13} & b_{17} \\ b_{13} - b_{11} & b_{17} - b_7 & b_{19} - b_5 & b_{23} - b_1 & b_1 & b_5 & b_7 & b_{11} \\ b_{19} - b_{17} & b_{23} - b_{13} & -b_{11} & -b_7 & -b_5 & -b_1 & b_1 & b_5 \\ -b_{23} & -b_{19} & -b_{17} & -b_{13} & -b_{11} & -b_7 & -b_5 & -b_1 \\ 0 & 0 & -b_{23} & -b_{19} & -b_{17} & -b_{13} & -b_{11} & -b_7 \\ 0 & 0 & 0 & 0 & -b_{23} & -b_{19} & -b_{17} & -b_{13} \\ 0 & 0 & 0 & 0 & 0 & 0 & -b_{23} & -b_{19} \end{bmatrix} \quad (5.19)$$

and the vector of phase current harmonics  $\underline{a}_\tau$

$$\underline{a}_\tau = [a_1, a_5, a_7, a_{11}, a_{13}, a_{17}, a_{19}, a_{23}]. \quad (5.20)$$

Only the average value of the electrical torque at zero harmonic and multiples of the 6th harmonic appears. Other harmonics are zero. Taking into account that matrix  $\underline{A}$  is square and has a full rank, estimating the torque harmonics as

$$\underline{\tau} = [2T_{Ref}, 0, 0, 0, 0, 0, 0, 0], \quad (5.21)$$

considering that zero coefficient  $\tau_0$  is the required torque  $T_{Ref}$  and all other torque harmonics should be zero, the solution for the linear system of equations defined by (5.18) can be found. On the other hand,



it leads to solving of the optimization problem described in (5.15) and delivers the optimal current waveform coefficients  $\underline{a}_\tau$  for estimation of the minimal torque ripples. For practical applications, a much smaller number of harmonics than given in (5.20) is enough. The larger number of current harmonics presented in (5.19) - (5.21) is necessary to explain the structure of the matrix  $\underline{A}$  in more detail. Thus, the optimal phase current waveform  $K_{opt,\tau}(\varphi_e)$  for torque ripples minimization can be estimated for each electrical angle with optimal harmonics coefficients  $\underline{\tau}$  as

$$K_{opt,\tau}(\varphi_e) = \sum_{\tau} a_{\tau} \sin(\tau \cdot \varphi_e), \quad (5.22)$$

It is important to note that, like a motor losses minimization, the torque ripple minimization approach allows to find an analytical solution for optimal phase currents that can be very effectively applied in online and adaptive applications.

### 5.3 Modal Current Control

In the previous two chapters, two strategies aimed to implement the operation of a PM motor with the minimal loss or minimal torque fluctuations have been described. Both methods are based on a powerful and stable current control able to deal with higher phase current harmonics. In this chapter, a Modal Current Control method will be presented, which introduces all structural benefits of the given optimal control problems and affords an opportunity for a very high speed and torque control. The Modal Current Control relies on the complete mathematical model of a PMSM with the air gap or combined winding described using (3.1) - (3.3). According to node equation (3.1), only two of the three phase currents are independent and controllable. Taking this relation into consideration, the equation (3.2) can be represented as

$$(\underline{u} - \underline{e})\underline{G} = \underline{R}_s \underline{i} + \underline{L}_s \frac{d\underline{i}}{dt} \quad (5.23)$$

using

$$\underline{G} = \frac{1}{3} \begin{bmatrix} 2 & -1 & -1 \\ -1 & 2 & -1 \\ -1 & -1 & 2 \end{bmatrix}. \quad (5.24)$$

For the system simplification, back-EMF  $\underline{e}$  can be neglected and, if necessary, added to input voltage  $\underline{u}$  as a feedforward compensation, or simply estimated as disturbance for the current controller. A coupled system in (5.23) for three phase currents  $\underline{i}$  can be completely separated with a modal transformation  $\underline{W}$

$$\begin{bmatrix} J_{\Sigma} \\ J_1 \\ J_2 \end{bmatrix} = \frac{1}{3} \underbrace{\begin{bmatrix} 1 & 1 & 1 \\ -1 & -1 & 2 \\ -1 & 2 & -1 \end{bmatrix}}_{\underline{W}} \begin{bmatrix} i_a \\ i_b \\ i_c \end{bmatrix} \quad (5.25)$$

applied to this system in a way that the matrix of the modal inductance

$$\underline{\Lambda} = \underline{W} \underline{L} \underline{W}^{-1} = \begin{bmatrix} L_s - 2M_s & 0 & 0 \\ 0 & L_s + M_s & 0 \\ 0 & 0 & L_s + M_s \end{bmatrix} \quad (5.26)$$

becomes diagonal. Thus, the modal transformation in (5.25) transforms three phase currents  $\underline{i}$  into modal currents  $\underline{J} = [J_{\Sigma} \ J_1 \ J_2]^T$ . Considering the star connection in (3.1) and first row of modal

transformation in (5.25), modal current  $J_\Sigma$  will be zero. It means, that only two out of three modal currents  $J_1$  and  $J_2$  associated with the modal inductances  $L_s + M_s$  are significant. The decoupled modal system

$$\frac{1}{3} \begin{bmatrix} 0 & 0 & 0 \\ -1 & -1 & 2 \\ -1 & 2 & -1 \end{bmatrix} \begin{bmatrix} u_a \\ u_b \\ u_c \end{bmatrix} = \begin{bmatrix} R_s & 0 & 0 \\ 0 & R_s & 0 \\ 0 & 0 & R_s \end{bmatrix} \begin{bmatrix} J_\Sigma \\ J_1 \\ J_2 \end{bmatrix} + \begin{bmatrix} L_s - 2M_s & 0 & 0 \\ 0 & L_s + M_s & 0 \\ 0 & 0 & L_s + M_s \end{bmatrix} \begin{bmatrix} dJ_\Sigma/dt \\ dJ_1/dt \\ dJ_2/dt \end{bmatrix} \quad (5.27)$$

shows uncontrollable state of modal current  $J_\Sigma$  due to zeros in the first row of the modal input matrix. According to the system (5.27), the remaining two modal currents  $J_1$  and  $J_2$  come from two identical first order systems with the motor time constant  $t_M$

$$t_M = \frac{L_s + M_s}{R_s}. \quad (5.28)$$

Elimination of the first non-controllable modal current  $J_\Sigma$  leads to

$$\frac{1}{3} \underbrace{\begin{bmatrix} -1 & -1 & 2 \\ -1 & 2 & -1 \end{bmatrix}}_{\underline{\Gamma}} \begin{bmatrix} u_a \\ u_b \\ u_c \end{bmatrix} = \begin{bmatrix} R_s & 0 \\ 0 & R_s \end{bmatrix} \begin{bmatrix} J_1 \\ J_2 \end{bmatrix} + \begin{bmatrix} L_s + M_s & 0 \\ 0 & L_s + M_s \end{bmatrix} \begin{bmatrix} dJ_1/dt \\ dJ_2/dt \end{bmatrix}. \quad (5.29)$$

In this way, the three-phase current control system can be reduced to the control of two completely decoupled first order systems associated with  $J_1$  and  $J_2$ . In practice, the redundant total current  $J_\Sigma$  displays any errors in the control loop due to sensor offsets and other inaccuracies and can be used as an indicator of the quality of control system online. Unconnected modal currents  $J_1$  and  $J_2$  can be controlled completely independently via modal input voltages  $\underline{V} = [V_1 \ V_2]^T$

$$\underline{V} = \begin{bmatrix} V_1 \\ V_2 \end{bmatrix} = \underline{\Gamma} \cdot \underline{u}. \quad (5.30)$$

as shown in the modal current control loop in Fig. 35. The proposed current separation based on the transformation given in (5.25) is very simple for implementation, does not use any trigonometric calculations according to the rotor position as opposed to the conventional Clarke-Park transformations, is independent of motor parameters and suited well for any shape of the non-ideal B-field.

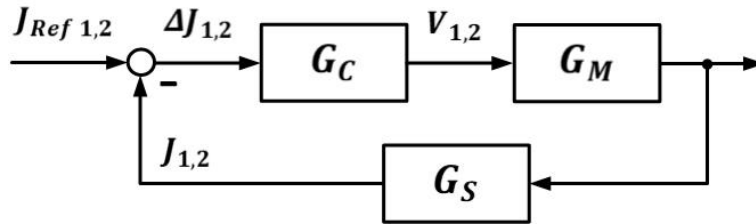


Fig. 35. Modal Current Control Loop for Modal Currents  $J_{1,2}$ .

As shown in Fig. 35, the modal current control loop consists of the motor transfer function  $G_M$ , the current sensor transfer function  $G_S$  and the current controller  $G_C$ . According to the modal system equation (5.29), the modal motor transfer function can be expressed as

$$G_M(s) = \frac{1/R_s}{1 + t_M s} \quad (5.31)$$

The design of a PMSM air gap winding is specified by a large number of poles and a very small motor time constant  $t_M$  in the range of 50-100 $\mu$ s due to a very low motor inductance [2]. This aspect requires a high switching frequency of transistors to keep the current and torque switching ripple in the acceptable range. For this reason, the sensor dynamics must be included in the modal current control loop with a first order sensor model

$$G_S(s) = \frac{1}{1 + t_S s} \quad (5.32)$$

and the sensor time constant  $t_S$ . A microcontroller generates PWM pulses at frequency  $f_{PWM} = 1/\Delta t$  to drive the B6-bridge and to control the motor input voltage. ADC samples the input signal from the current sensors with the same rate. It means that the time continuous transfer function

$$G_{MS}(s) = G_M(s) G_S(s) \quad (5.33)$$

has to be discretized with frequency  $f_{PWM}$  to get the discrete transfer function

$$D_{MS}(z) = \frac{(\beta - 1 + (1 - \alpha)\delta)z + ((\alpha - 1)\delta - \alpha)\beta + \alpha}{R_s(\delta - 1)(z - \alpha)(z - \beta)} \quad (5.34)$$

with the sampling time  $\Delta t$ , discrete eigenvalues of the motor  $\alpha = e^{-\frac{\Delta t}{t_M}}$ , sensor  $\beta = e^{-\frac{\Delta t}{t_S}}$  and the motor/sensor speed ratio  $\delta = \frac{t_M}{t_S}$ . A discrete PID controller with a filtered derivative action according to Forward Euler integrator method can be described as

$$D_C(z) = K_P + \frac{K_I}{z - 1} + \frac{K_D}{N_D + \frac{1}{z - 1}}, \quad (5.35)$$

where  $K_P$  is a proportional gain,  $K_I$  is an integral gain,  $K_D$  is a derivative gain and  $N_D$  is a derivative filter coefficient. A discrete PID affords an opportunity to place all four poles of the discrete closed loop transfer function of the modal current control

$$D(z) = \frac{D_C(z) D_{MS}(z)}{1 + D_C(z) D_{MS}(z)} \quad (5.36)$$

to produce finally a controlled system of 1<sup>st</sup> order described as

$$D(z) = \frac{1 - z_R}{z - z_R}. \quad (5.37)$$

The control parameters of PID can be determined by comparison of coefficients of these discrete closed loop and the reference transfer functions according to the Pole Placement with Zero Cancellation Method as

$$\begin{aligned}
 K_P &= \frac{(1 - \alpha + \delta(\beta - 1))R_s(z_R - 1)}{(\delta - 1)(\beta - 1)(\alpha - 1)} \\
 K_I &= R_s(z_R - 1) \\
 K_D &= \frac{R_s\delta(z_R - 1)(\beta - \alpha)^2}{(\delta - 1)^2(\beta - 1)^2(\alpha - 1)^2} \\
 N_D &= \frac{\beta - 1 + \delta(1 - \alpha)}{(\delta - 1)(\beta - 1)(\alpha - 1)},
 \end{aligned} \tag{5.38}$$

with the requested eigenvalue  $z_R = e^{-\frac{\Delta t}{t_{Req}}}$ , where  $t_{Req}$  is a requested time constant.

The outputs from the Modal PID controllers are two modal control voltages  $V_1$  and  $V_2$ . The final action in the Modal Current Control, according to (5.30), is a modal voltages transformation back to the three control voltages  $\underline{u}$  by means of a Moore Penrose pseudo inverse transformation matrix  $\underline{\Gamma}^+$

$$\begin{bmatrix} u_a \\ u_b \\ u_c \end{bmatrix} = \underbrace{\begin{bmatrix} -1 & -1 \\ 0 & 1 \\ 1 & 0 \end{bmatrix}}_{\underline{\Gamma}^+} \begin{bmatrix} V_1 \\ V_2 \end{bmatrix}. \tag{5.39}$$

The Modal Current Control provides the system stability, very high dynamics and implementation of the given optimal torque reference behavior without any restriction on B-field harmonics, and regardless of the system parameters deflections due to motor temperature variations and other factors. The only important precondition for this approach is accuracy of the mathematical model in (3.1) - (3.3) and the motor parameters such as phase resistance  $R_s$ , phase self/mutual inductance  $L_s, M_s$  and B-field harmonic coefficients, which can be very good performed for air-gap or combined winding of PMSM. The complete Modal Current Control signal flow is included in OTMIC control shown in the control diagram in Fig. 36.

## 5.4 Modified Space Vector PWM

As it has been mentioned above, the first requirement for control systems for a low inductance PMSM is simplicity, that means that a microcontroller should be able to calculate the control loop with the required sampling time. For this reason, the conventional Space Vector PWM approach presented in Chapter 3.2 has been modified and simplified according to the proposed control model. The space vector modulation algorithm provides the calculation of the pulse widths based on the  $\alpha\beta$  reference frame representation. The Modified SVPWM for OTMIC control has been implemented in a three-phase system, considering that the electrical angle and the back-EMF zero values of the first phase  $a$  must match.

The input values to the MSVPWM are three control voltages  $\underline{u}$  obtained after the modal transformation, the electrical angle and the supply DC voltage  $u_{DC}$ . The space vector modulation of three phase PWM signals correspondent to the electrical angle position can be divided into six sectors  $s_i$  [46],[47]. The switching reference function of each inverter leg  $\underline{d}_{PWM} = [d_{PWM,a} \ d_{PWM,b} \ d_{PWM,c}]^T$  represents the duty cycle ratio of each phase or the conduction time normalized to the sampling time  $\Delta t$  for the given switch ranging between -1 and 1. The duty cycle  $\underline{d}_{PWM}$  of each phase can be estimated in accordance with the given values of control voltages and a sector number normalized to the supply voltage as shown in TABLE IX.

TABLE IX. MSVPWM SWITCHING TABLE

Sector	$s_i$	$d_{PWM,a}$	$d_{PWM,b}$	$d_{PWM,c}$
$0 \leq \varphi_e < \frac{\pi}{3}$ & $\pi \leq \varphi_e < \frac{4\pi}{3}$	1 4	$\frac{1}{\sqrt{3}u_{DC}}(u_a - u_b)$	$\frac{1}{\sqrt{3}u_{DC}}(u_b - u_a)$	$\frac{1}{\sqrt{3}u_{DC}}(2u_c - u_a - u_b)$
$\frac{\pi}{3} \leq \varphi_e < \frac{2\pi}{3}$ & $\frac{4\pi}{3} \leq \varphi_e < \frac{5\pi}{3}$	2 5	$\frac{1}{\sqrt{3}u_{DC}}(u_a - u_c)$	$\frac{1}{\sqrt{3}u_{DC}}(2u_b - u_a - u_c)$	$\frac{1}{\sqrt{3}u_{DC}}(u_c - u_a)$
$\frac{2\pi}{3} \leq \varphi_e < \pi$ & $\frac{5\pi}{3} \leq \varphi_e \leq 2\pi$	3 6	$\frac{1}{\sqrt{3}u_{DC}}(2u_a - u_b - u_c)$	$\frac{1}{\sqrt{3}u_{DC}}(u_b - u_c)$	$\frac{1}{\sqrt{3}u_{DC}}(u_c - u_b)$

This modification of a conventional SVPWM leads to a very fast calculation of the required PWM duty cycle for every stator phase according to the electrical angle position. It can be noted, that the proposed modification does not consider the overmodulation region. However, the OTMIC control can be combined with any pulse width modulation approach, and this issue may be considered in more detail in future works.

## 5.5 Control Structure of OTMIC Approach

The proposed Combined Optimal Torque and Modal Current Control (OTMIC) includes the torque ripple or motor loss minimization using the algorithms proposed in Chapters 5.1 and 5.2, the Modal Current Control described in Chapter 5.3 and the Modified SVPWM proposed in Chapter 5.4. Thus, the air gap winding or combined winding PMSM control can be divided into three stages.

The first stage consists of a phase current waveform optimization and the calculation of three phase current references with a given reference torque  $T_{Ref}$  and the electrical angle  $\varphi_e$ . Three optimal phase current waveforms  $\underline{K}_{opt} = [K_{opt,a}(\varphi_e) \ K_{opt,b}(\varphi_e) \ K_{opt,c}(\varphi_e)]^T$  for minimal motor losses or torque ripples can be estimated using (5.12) or (5.22) for each electrical angle as

$$\underline{K}_{opt} = \begin{bmatrix} K_{opt}(\varphi_e) \\ K_{opt}(\varphi_e - 2\pi/3) \\ K_{opt}(\varphi_e - 4\pi/3) \end{bmatrix}. \quad (5.40)$$

Three phase current references  $\underline{i}_{Ref} = [i_{Ref,a}(\varphi_e) \ i_{Ref,b}(\varphi_e) \ i_{Ref,c}(\varphi_e)]^T$  are determined with a given torque reference  $T_{Ref}$  and the electrical angle according to

$$\underline{i}_{Ref} = \frac{T_{Ref}}{k_M} \underline{K}_{opt}, \quad (5.41)$$

and used as a reference for measured phase currents  $\underline{i} = [i_a(\varphi_e) \ i_b(\varphi_e) \ i_c(\varphi_e)]^T$ . The resulting current errors  $\Delta \underline{i}$

$$\Delta \underline{i} = \underline{i}_{Ref} - \underline{i} \quad (5.42)$$

are fed to the Modal Current Control, which means the beginning of the second stage of OTMIC control. At this stage, the current errors are transformed to modal currents errors  $\underline{J}$  with a modal transformation  $\underline{W}$  according to (5.25), which then have to be compensated by two PID controllers separately. PID controllers generate two control voltages  $\underline{V}$ , which are transformed to three phase control voltages  $\underline{u}$  with pseudo inverse transformation (5.39).

The third and the last stage is needed to set PMSM in motion with the optimal torque waveform via a MSVPWM and a B6-bridge according to control voltages  $\underline{u}$ , DC voltage  $u_{DC}$  and the electrical angle  $\varphi_e$ . The control diagram of OTMIC approach with a back-EMF compensation is shown in Fig. 36.

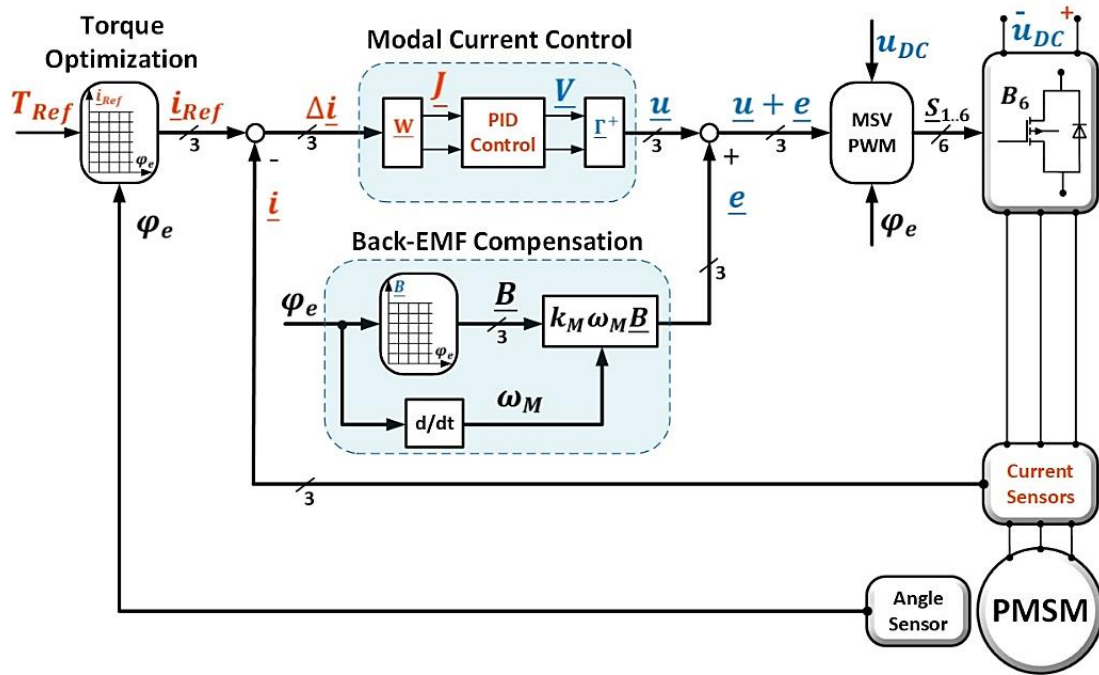


Fig. 36. Proposed OTMIC control diagram of PMSM drive system

The back-EMF compensation can be applied to the system in the same way as the calculation of optimal current references. A B-Filed waveform  $B(\varphi_e)$  can be stored in the table according to the electrical angle. Three phase B-Field waveforms  $\underline{B} = [B_a(\varphi_e) \ B_b(\varphi_e) \ B_c(\varphi_e)]^T$  can be estimated for each electrical angle as

$$\underline{B} = \begin{bmatrix} B(\varphi_e) \\ B(\varphi_e - 2\pi/3) \\ B(\varphi_e - 4\pi/3) \end{bmatrix}. \quad (5.43)$$

Then using the equation (3.4) and the given angular velocity  $\omega_M$ , three back-EMF waveforms  $\underline{e} = [e_a(\varphi_e) \ e_b(\varphi_e) \ e_c(\varphi_e)]^T$  can be found and added to the control voltages  $\underline{u}$ . The conventional approach for estimation of phase currents actual values based on the two current sensors and the calculation of the third current using (3.1) leads to additional errors in the current control loop due to non-ideal offsets and accuracies of the sensors, that matter in a high-frequency control for PMSM with a large number of poles. To overcome this problem, in OTMIC control, the estimation of currents actual values should be implemented on the basis of three current sensors with their pre-calibration. An encoder or two

analog hall sensors can be used for electric angle measurement. This issue is described in more detail in Chapter 6.1.

In comparison to vector control techniques described in Chapter 3, OTMIC method leads to a significant simplification of the microcontroller control loop due to use of independent electrical angle modal transformations with simple coefficients. In addition, an optimal current waveform according to (5.12) and (5.22) can be calculated off-line from 0 to  $2\pi$  radian and stored in a table. Then, three optimal phase current waveforms  $\underline{K}_{opt}$  can be defined according to (5.40) by shifting the given electrical angle by  $2\pi/3$  and  $4\pi/3$  radian for phases  $b$  and  $c$ , respectively, using the modulo operation. Another way to simplify this algorithm without modulo operation, that takes additional estimated time in the microcontroller on-line, is to extend the look-up table from  $2\pi$  to  $2\pi + \pi/2$ . However, this method requires more CPU memory. The simplifications described above together with the periphery for PWM generation, an on-chip floating-point unit (FPU) and parallel running ADC with sensor measurements allow to implement the control loop shown in Fig. 37 with a very short step size  $\Delta t$  less than  $10\mu s$ .

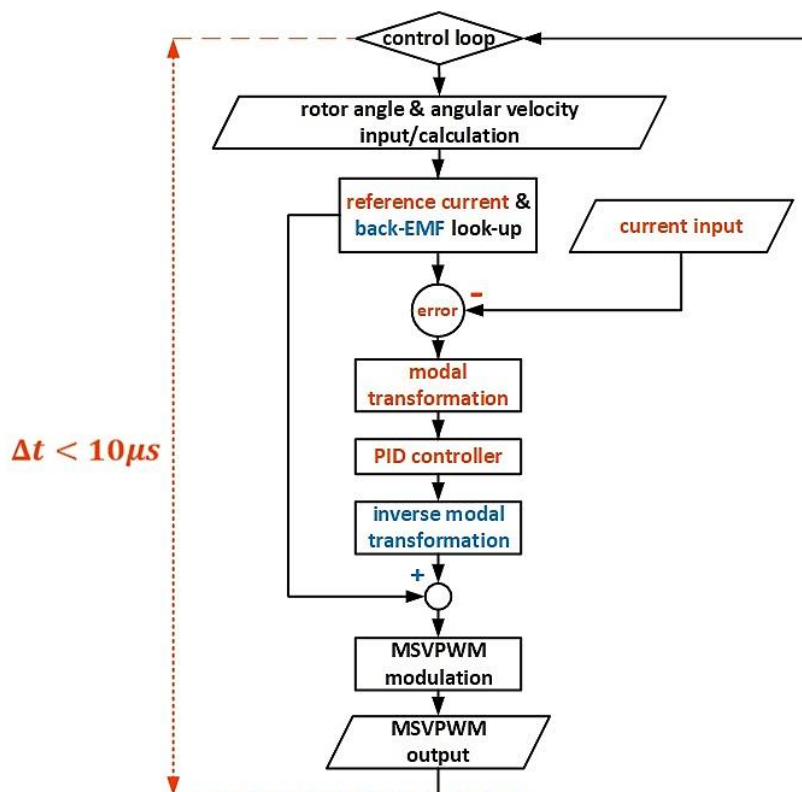


Fig. 37. Flowchart of OTMIC Control Loop for PMSM.

The basic input parameters for OTMIC control are: motor parameters such as motor geometric constant  $k_M$ , number of poles  $p$  and look-up tables with optimal current and, if necessary, B-Field waveforms; PID controller parameters  $K_P$ ,  $K_I$ ,  $K_D$ ,  $N_D$  calculated with a motor phase inductance  $L_S$ , resistance  $R_S$ , sensor time constant  $t_S$  and sampling time  $\Delta t$ ; parameters of current and angle sensors such as sensor sensitivity and offsets values.

Taken together, these findings highlight a role for Combined Optimal Torque and Modal Current Control as a control approach for new low inductance and high-power PMSM. OTMIC control guarantees the performance of the given torque reference behavior, stability and high system dynamics regardless of the system parameters fluctuations due to changes of motor temperature and other factors.

Simplicity of the proposed control method allows its implementation based on any low-cost microcontroller. Moreover, the Optimal Torque and Modal Current Control can be used for any form of B-field making it a universal control approach for any PMSM or BLDC machines. Verification of the proposed method based on the simulation and experimental results is presented in the next chapter.



## 6. Modelling and Validation of OTMIC Approach

Air gap winding or combined winding permanent magnet synchronous motors can be widely applied to any form of electric mobile applications. Technologies of electric vehicles enter a new stage of development in response to a wheel hub motor approach, as they reduce the mechanical section to minimum and allow to create a completely new design of mobile application without mechanical transmissions, differentials, gearboxes and drive shafts. It leads to a weight and manufacturing cost saving. A wheel hub drive is incorporated into a wheel hub and puts it in motion directly offering more space for a user. In this reason, the main requirements for the wheel hub motor are low weight and in the same time high power and torque. Thus, the high specific torque and power densities are the main quality index of wheel hub motors.

Considering this fact, a new concept for very lightweight wheel-hub motors based on the air gap winding or combined winding technologies presented by OvGU University in [1]-[22] is the most promising. Some types of e-Mobility, such as scooters, e-bicycles, longboards etc. operate within a middle speed range (up to 60 km/h) and middle engine torque (up to 200 Nm). On the other hand, due to a larger car weight in comparison with the first ones, modern electric cars require a high motor torque and operation speed (more than 120 km/h). The equation (3.8) shows that the maximal motor torque of an air gap or combined winding motor is directly proportional to the current and is mainly limited by the temperature properties of the winding. In contrast, according to (3.3) and (3.4), the maximal motor speed is determined by the level of DC voltage  $u_{DC}$  supplying the system, which must exceed the maximal back-EMF value  $e_{max} = \omega_{rated} k_M B_{max}$  generated as a function of the rated mechanical angular velocity  $\omega_{rated}$ . As it has been mentioned above, air gap and combined winding technologies lead to a very low motor inductance. To find the dependency between the current ripple and switching frequency of a motor, the equation (3.2) can be approximately rewritten according to [100] as

$$\Delta i_{max} = \frac{(u_{DC} - \sqrt{2}u_0)u_0}{2L_{ph}u_{DC}f_{PWM}}, \quad (6.1)$$

where  $u_0$  is line-to-line voltage. This suggests that maximal phase current ripples  $\Delta i_{max}$  are more dependent on DC voltage, phase inductance and switching frequency  $f_{PWM}$  and less dependent on phase current and motor speed. Based on these facts, the verification of the proposed OTMIC control has been implemented using two prototypes of air gap winding and combined winding wheel hub PM motors. First air gap winding motor can operate in the middle speed at the supply voltage of 48V and has a very low phase inductance of about  $1.5\mu H$  [2]. The second combined winding motor needs a 650V supply voltage for high-speed operation and has increased phase inductance due to the additional slot winding to  $45\mu H$  [3]. Fig. 38 shows the approximate relationship between the current ripples and the switching frequencies from 10 kHz to 200 kHz for both motor types. Thus, the verification of the proposed OTMIC control on two electric drive systems operating at 48V and 650V, respectively, with different levels of phase inductance can lead to a more detailed analysis and give more accurate results. Considering the conventional parameters of power electronic and based on the approximate results shown on Fig. 38, the switching frequency of 100 kHz has been selected for both systems.

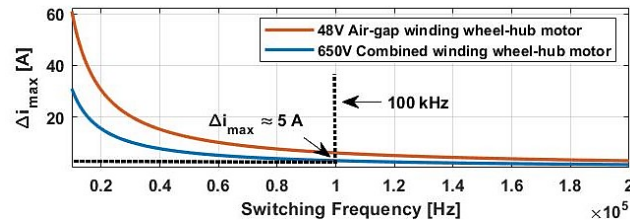


Fig. 38. Approximate Relationship between Current Ripples and Switching Frequency.

The proposed combined Optimal Torque and Modal Current Control approach will be verified in this chapter in comparison to simulation and experimental results in one hand, and to conventional vector control (FOC) selected from the other conventional control methods in Chapter 3.6 on the other hand. According to the main requirements to the control system for low inductance high power PMSM, the OTMIC verification can be divided into three parts. First part describes the control implementation process in the microcontroller, that should be corresponded to the switching frequency of 100 kHz and sampling time of 10  $\mu$ s. The second part shows the OTMIC verification as a control system for 48V air gap winding wheel hub motor. OTMIC dynamic verification is based on the simulation and measurement results of torque and phase currents step response. Then, the proposed and conventional control method during normal PMSM operation will be compared in simulation and in experiment. The last part describes the verification of OTMIC and FOC control methods for combined winding wheel hub motor under normal operating conditions.

## 6.1 Microcontroller Programming

Two preparatory offline calculations must be carried out to ensure a reliable motor startup, considering the motor parameters. More precisely:

1. The calculation of the look-up table with an optimal current waveform for motor losses minimization and torque ripple reduction as a function of the electric angle;
2. Determination of PID controller parameters based on the switching frequency and time constants of the motor and the current sensor.

On the other hand, for microcontroller online operations, all peripherals necessary for an electric angle and a phase currents estimation and for PWM signals output must be configured. Thus, these steps are described in this section in more detail.

### 6.1.1 Control System Operation

The Optimal Torque and Modal Current Control has been implemented based on ARM Cortex-M4F microcontroller running at 200 MHz [109]. The microcontroller operation in online mode presented in Fig. 39 can be contingently divided into three stages: measurement of currents and an electrical angle, straight forward operation of the control algorithm and, finally, generation of control signals by means of PWM. The first and the last operation as well as the torque reference input with a potentiometer can be carried out in parallel with operation of the main control algorithm using additional peripherals such as: ADC (Analog-to-digital converter) for discretization of phase current actual values and the reference torque input; QPRC (Quadrature Position/Revolution Counter) for a rotor angle detection; OCU (Output Compare Unit), FRT (Free Run Timer) and WFG (Waveform Generator) for output PWM signals generation [109].

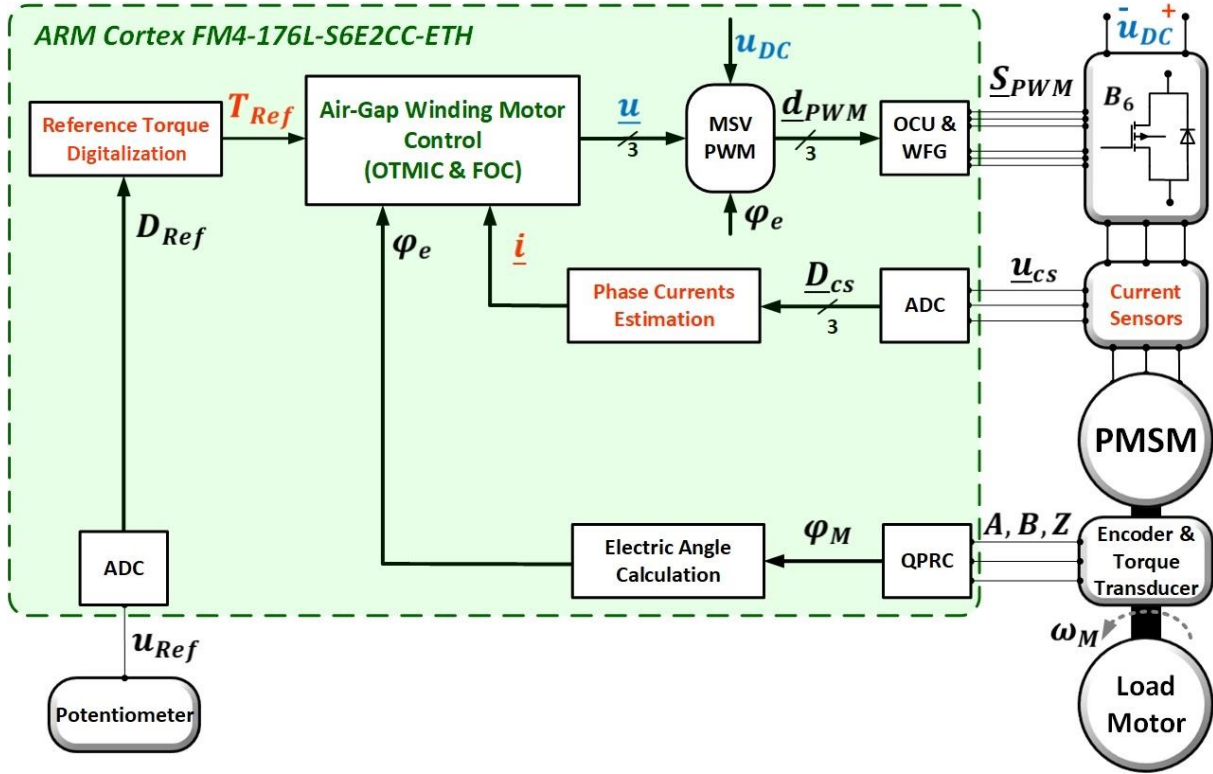


Fig. 39. Control System Operation in Online Mode.

For the electrical angle computation, A02H incremental encoder manufactured by Fritz Kübler GmbH has been used [110]. Three Allegro ACS730 current sensors have been integrated to the system for phase current measurement [107]. The full list of microcontroller and sensors parameters used for implementation of the control system is presented in the TABLE X.

TABLE X. MICROCONTROLLER AND CURRENT SENSOR PARAMETERS [107],[109]

Symbol	Description	Value	UOM
$U_{IOUT(Q)}$	Current Sensor Zero Current Output Voltage	2.5	V
$S_{CS}$	Current Sensor Sensitivity	50	mV/A
$U_{OE}$	Current Sensor Offset Voltage	~40	mV
$U_{CS,max}$	Current Sensor Maximal Output Voltage	3.3	V
$U_{CS,min}$	Current Sensor Minimal Output Voltage	0.3	V
$X_{CS,max}$	ADC analog high value	3.3	V
$X_{CS,min}$	ADC analog low value	0	V
$D_{CS,max}$	ADC digital high value	4096	-
$D_{CS,min}$	ADC digital low value	0	-
$f_{MFT}$	MFT clock frequency	200	MHz
$f_{FRT}$	FRT frequency	100	kHz
$N_{CC}$	Maximum FRT value	1000	-

According to the simulations results in Matlab Simulink, the back-EMF compensation for both motor prototypes working at 48V and 650V supply DC voltages, respectively, does not bring significant results and can be neglected to reduce the computational volume in the microcontroller. The block diagram of

Optimal Torque and Modal Current Control without back-EMF compensation implemented and verified in this chapter is shown in more detail in Fig. 40.

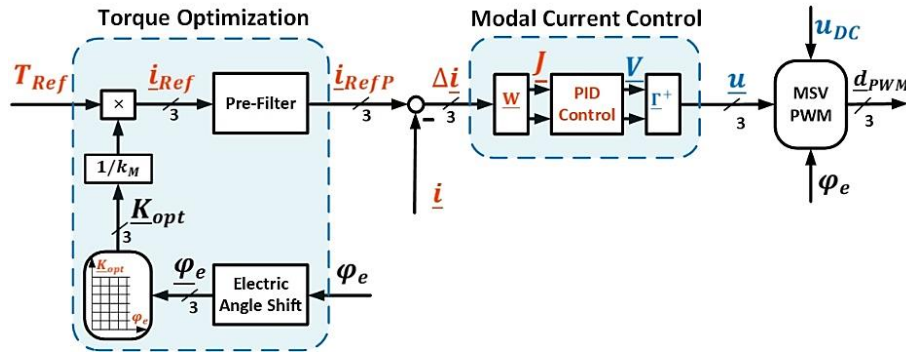


Fig. 40. Block Diagram of Proposed OTMIC Control without back-EMF Compensation.

For a more complete OTMIC analysis, the proposed control has been compared in simulation and in practice with the conventional Field Oriented Control presented in Fig. 41 without back-EMF compensation. Due to very low motor inductance, the decoupling calculation using (3.43) gives very low values of  $u_d^*$  and  $u_q^*$  and has also been neglected to reduce the calculation time of the control cycle in the processor.

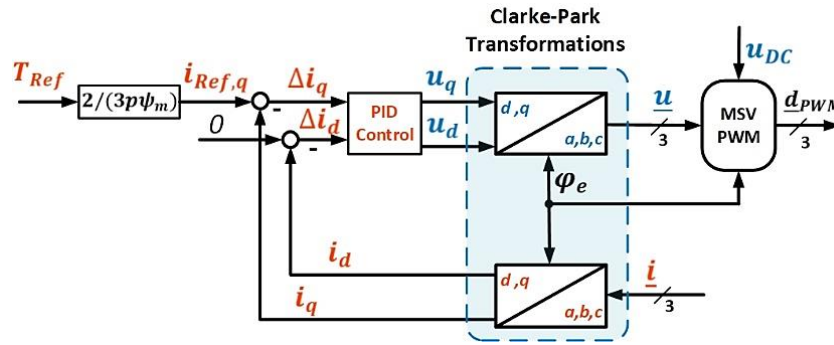


Fig. 41. Block Diagram of Conventional FOC without back-EMF Compensation and Decoupling.

For PWM signal generation, a simple-edge modulation with a triangular shape operating with frequency  $f_{PWM}$  has been used, because it offers better harmonic performance as opposed to other waveforms of the modulation signal [46],[47]. In a simple-edge unipolar modulation, the three duty cycle values from MSVPWM output  $d_{PWM} = [d_{PWM,a} \ d_{PWM,b} \ d_{PWM,c}]^T$  must be scaled between 0 and  $N_{CC}$  and then compared with a triangular shape, that has been implemented in the microcontroller by means of FRT configured in Up/Down Counter Mode as shown in Fig. 42.

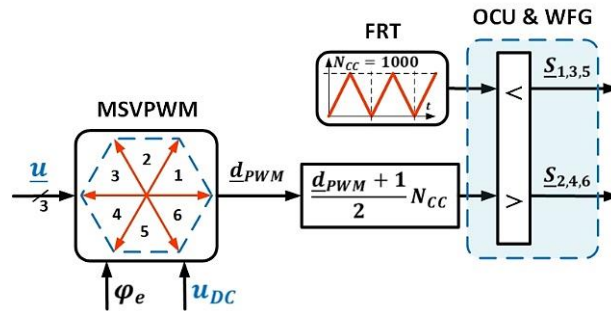


Fig. 42. Gate Signals Generation by means of MSVPWM, FRT and OCU.

In this case  $N_{CC}$  is a maximum FRT value, that can be find as

$$N_{CC} = \frac{f_{MFT}}{2f_{FRT}} = \frac{f_{MFT}}{2f_{PWM}}. \quad (6.2)$$

A comparison between  $\underline{d}_{PWM}$  and FRT has been implemented using OCU. By means of WFG the OCU output signals  $\underline{S}_{PWM}$  have been connected to the correct microcontroller pins and then to the B6-bridge. Thus, the interconnection of the Multifunction Timer peripheral component as shown in Fig. 43 gives an opportunity to generate PWM signals parallel to the main program loop operation.

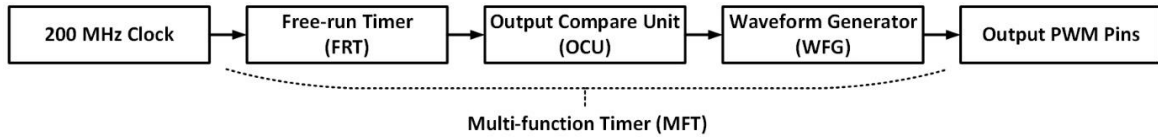


Fig. 43. MFT Peripheral Component Interconnection.

Offline calculated and stored in the table for each electrical angle, the optimal current waveforms together with MFT peripheral component interconnection allow to implement the OTMIC control loop based on ARM Cortex-M4F microcontroller with a very small step size of  $8.3\mu s$  as shown in Fig. 44.

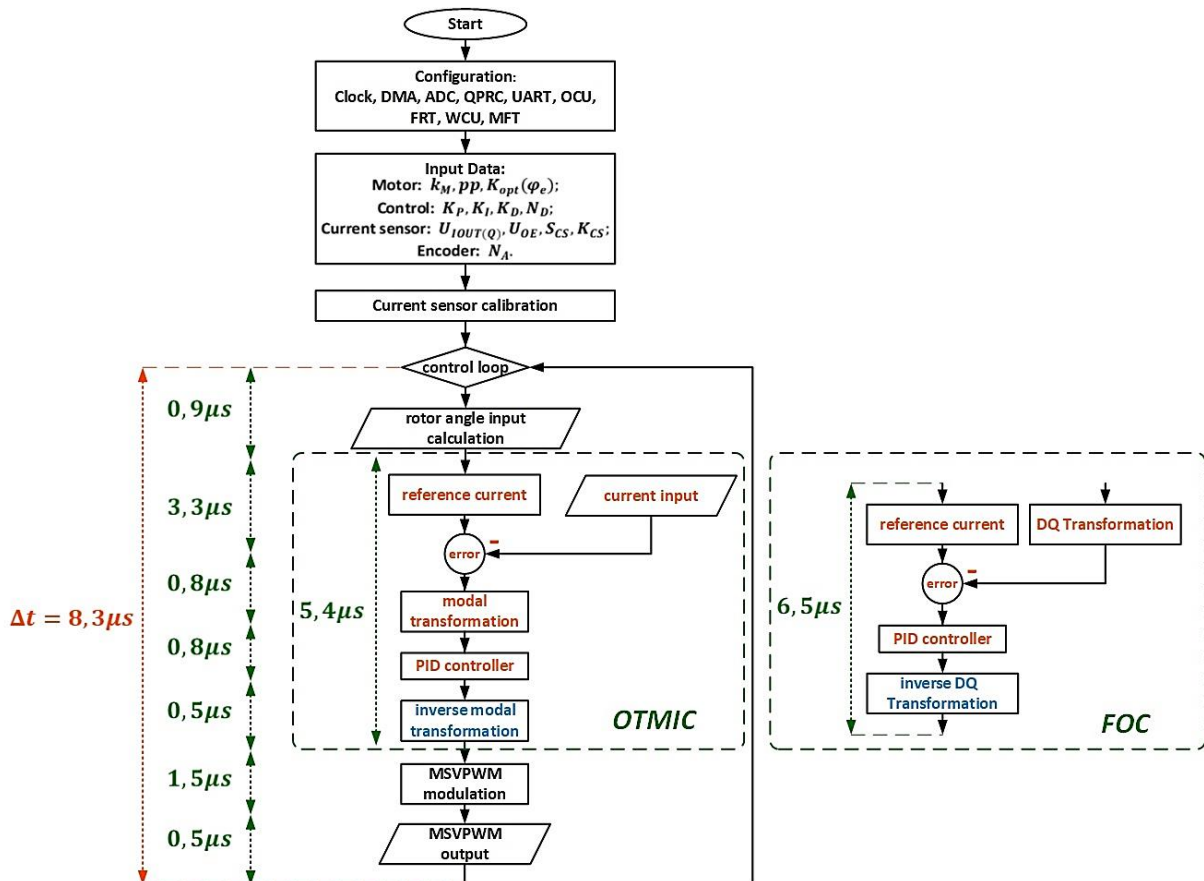


Fig. 44. Flowchart of OTMIC and FOC Control Loop.

To reduce the calculation time, the vector control algorithm has also been optimized by using a table with the sine and cosine values as a function of the electrical angle. However, in comparison to OTMIC control, the Field Oriented Control without the back-EMF compensation, decoupling and observer due

to trigonometric Clarke-Park transformation needs  $9.4\mu\text{s}$  for the control loop calculation on the same microcontroller.

At a given switching frequency of 100 kHz and using ARM Cortex-M4F microcontroller, it is impossible to minimize motor losses or torque ripples with the methods described in [46]-[80] as well as to implement back-EMF compensation, field weakening or sensorless motor control. The solution for this problem is to replace the microcontroller on an expensive one, or to reduce the switching frequency, which will lead to an increase in current switching ripples. However, neither solution is optimal; and this underlines the advantage of the proposed OTMIC control method able to implement above listed requirements in  $8.3\mu\text{s}$ . As shown in the Fig. 44, in order to run the main OTMIC and FOC control algorithm, it is necessary to set the sensors and PID parameters, lookup tables, as well as to calibrate the current and angle sensors. These processes will be described in the following sections.

### 6.1.2 Phase Currents Measurement

A 12-bit analog-to-digital converter (ADC) operates with successive approximation and an integrated sample-and-hold circuit [109]. For three phase current measurement, each current sensor can be connected to its own ADC channel. After the PWM edge, the current sensors need about  $1\mu\text{s}$  until the oscillation of the measuring signal due to the presence of a capacitor in the circuit is stabilized. The ADC also needs approximately  $1\mu\text{s}$  for transient oscillation. Thus, two different times are necessary for the current measurement. The FRT (free-running timer) must trigger two interrupts to check, which of the sensors may currently be converted. A detailed principle operation of the current sensor ACS733KLATR-40ABT based on the hall effect and used in the experimental setup is illustrated in the Fig. 45. The sensor can operate with a bipolar current of up to 40 amperes [107]. The current flowing through the sensor produces an output voltage in the range of 0.3 -3.3 volts. The accuracy of the sensor measurements is 50 mV/A [107]. Analog voltage from the current sensor is converted by means of ADC into a digital value from 446 to 3724 according to the input voltage range [109].

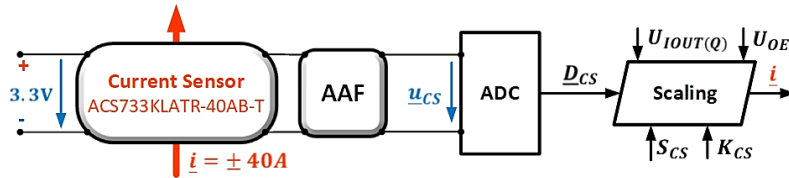


Fig. 45. Phase Current Measurement.

After that, the discrete values at the ADC output should be converted into the values of the current flowing through the sensor as

$$\hat{i} = [(K_{CS}D_{CS} - U_{IOUT(Q)}) - U_{OE}]/S_{CS} \quad (6.3)$$

where  $S_{CS}$  – current sensor sensitivity,  $\underline{D}_{CS} = [D_{CS,a} \ D_{CS,b} \ D_{CS,c}]^T$  – ADC outputs of the three current sensors,  $K_{CS} = \frac{X_{CS,max} - X_{CS,min}}{D_{CS,max} - D_{CS,min}} = \frac{3.3 - 0}{4096 - 0}$  – signal resolution,  $U_{IOUT(Q)}$  – sensor zero current output voltage,  $U_{OE}$  – current sensor offset,  $X_{CS,max}, X_{CS,min}$  – ADC analog high and low values,  $D_{CS,max}, D_{CS,min}$  – ADC digital high and low values. These data are given in the sensor and microcontroller date sheets [107] and [109]. However, such parameters as sensor sensitivity and voltage offset are not ideal constant and dependent on the sensor temperature and other factors [107]. It leads to the fact that, the star connection Kirchhoff's 1st Law (3.1) ceases to be valid. From the point of view of a modal control, this means that the redundant total current  $J_{\Sigma}$  ceases to have zero values and reflects all

asymmetries in the system caused by the discrepancy between the measured current values and their actual values. In addition, as shown in the Fig. 45, to prevent aliasing frequencies from entering the systems and satisfy the Nyquist–Shannon sampling theorem over the band of interest, it is necessary to use an anti-aliasing filter (AAF) at the ADC input with frequency  $f_{AAF}$  [46],[47]. However, the filter frequency should not be chosen too small, since at high engine speeds it can lead to a significant phase shift of the measured currents relative to the given ones. Therefore, for the proposed control system, an AAF has been selected with a frequency equal to half the switching frequency  $f_{PWM}$ . For additional safety and more stable operation of the system, it is necessary to include a discrete pre-filter in the current reference circuit as shown in Fig. 40. The frequency of the pre-filter should correspond to the AAF frequency, so the phase shift between the reference currents and the measured actual values will be minimized [46],[47]. Summing up, it can be noted that for stable engine operation, the current measurement system should be as reliable as possible, work without interference and, if possible, be able to adapt its parameters to any changes in the operating conditions of the system, such as temperature and pressure. Preliminary measurements of the Allegro sensor's accuracy and the harmonic analysis of their signals are presented in Appendix B.

### 6.1.3 Electrical Angle Measurement

A02H Fritz Kübler **Incremental Encoder** used in the system can generate 5,000 pulses from each channel in one revolution [110]. Channel B is shifted by  $90^\circ$  degrees relative to channel A. This makes it possible, by counting the falling and rising edges for each channel, to get 20,000 pulses per one motor revolution. The QPRC (Quadrature Position/Revolution Counter) unit can be used to evaluate the rotary encoder position in parallel with the processor operation without creating a load on it [109]. The 16-bit position counter can count all edges of the A and B encoder signals depending on the configuration and is reset by the Z impulse. The mechanical angular velocity of the rotor  $\omega_M$  has been estimated by means of the multi-functional 16-bit PWC (Pulse Width Count) Timer able to measure the pulse width of the input signal [109]. Accordingly, the angular velocity has been determined as a function of the time between two edges of channel A continuously measured with PWC as

$$\omega_M = \frac{2\pi \cdot f_{MFT}}{N_A \cdot K_{PWC} \cdot N_{PWC}}, \quad (6.4)$$

where  $K_{PWC} = 128$  – sub-factor for the main PWC tact (can be given in the range between  $2^0$  up to  $2^{11}$ ),  $N_A = 5000$  – increment number of one encoder channel and  $N_{PWC}$  – PWC counter value [109].

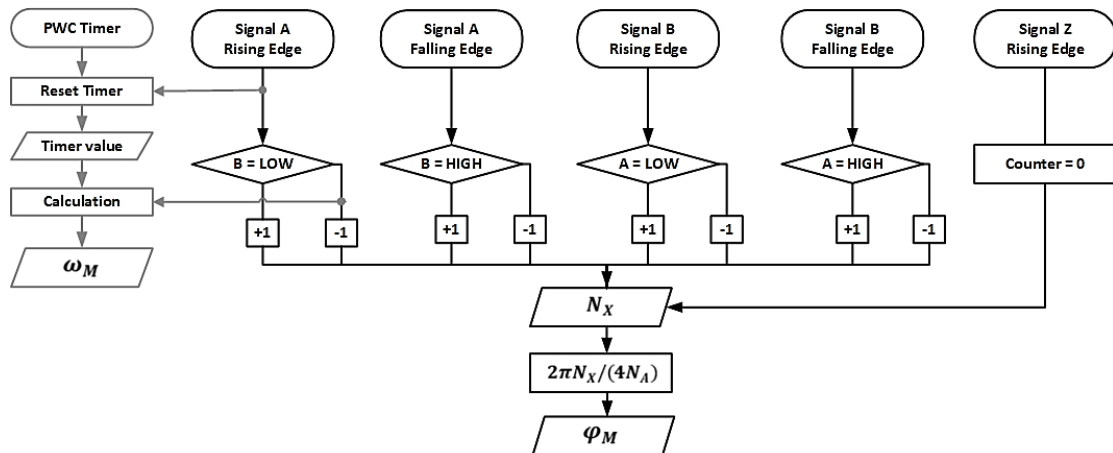


Fig. 46. Rotor Position and Angular Velocity Estimation with QPRS.

Schematically, the calculation of the rotor position  $\varphi_M$  and motor angular velocity  $\omega_M$  are presented in Fig. 46, where  $N_X$  is an actual increment number between 0 and  $4N_A$  corresponded to the rotor position between 0 and  $2\pi$ . According to the mathematical motor model and the MSVPWM operation principle, the rotor position zero point for clockwise and  $2\pi$  point for anticlockwise motor rotation must coincide with the zero crossing of the back-EMF of first phase  $a$ . This makes it necessary to calibrate the mechanical angle, which must be performed before the start of the test. Calibration is carried out by measuring the  $e_a$  and encoder Z impulse during the motor rotation. Thus, the angle error  $\Delta\varphi_M$  can be found as the distance between the zero point of the  $e_a$  and the impulse Z. The required value of the electric angle  $\varphi_e$  can be found using the modulo operation on the difference between the preliminary mechanical angle value  $\varphi_M$  and the error  $\Delta\varphi_M$  multiplied by motor number of poles  $p$  as

$$\varphi_e = \text{mod}((\varphi_M - \Delta\varphi_M)p/2, 2\pi). \quad (6.5)$$

As noted above, the electric angle is necessary to select the optimal current values  $\underline{K}_{opt} = [K_{opt}(\varphi_{e,a}) \ K_{opt}(\varphi_{e,b}) \ K_{opt}(\varphi_{e,c})]^T$  from the offline stored  $K_{opt}(\varphi_e)$  table. Phase  $a$  coincides with  $\varphi_e$ , so to select the optimal current values of phases B and C, it is necessary to shift the electric angle with modulo operation by  $120^\circ$  and  $240^\circ$  electrical degrees respectively as

$$\begin{aligned} \varphi_{e,a} &= \varphi_e \\ \varphi_{e,b} &= \text{mod}(\varphi_e - 2\pi/3, 2\pi) \\ \varphi_{e,c} &= \text{mod}(\varphi_e - 4\pi/3, 2\pi). \end{aligned} \quad (6.6)$$

The resulting vector of three rotor position values  $\underline{\varphi}_e = [\varphi_{e,a} \ \varphi_{e,b} \ \varphi_{e,c}]^T$  makes it possible to find the three reference currents for each phase. The practical implementation of the described above electric angle estimation process is shown in Fig. 47 with measured back-EMF and encoder output signals before and after calibration point for three pairs of poles.

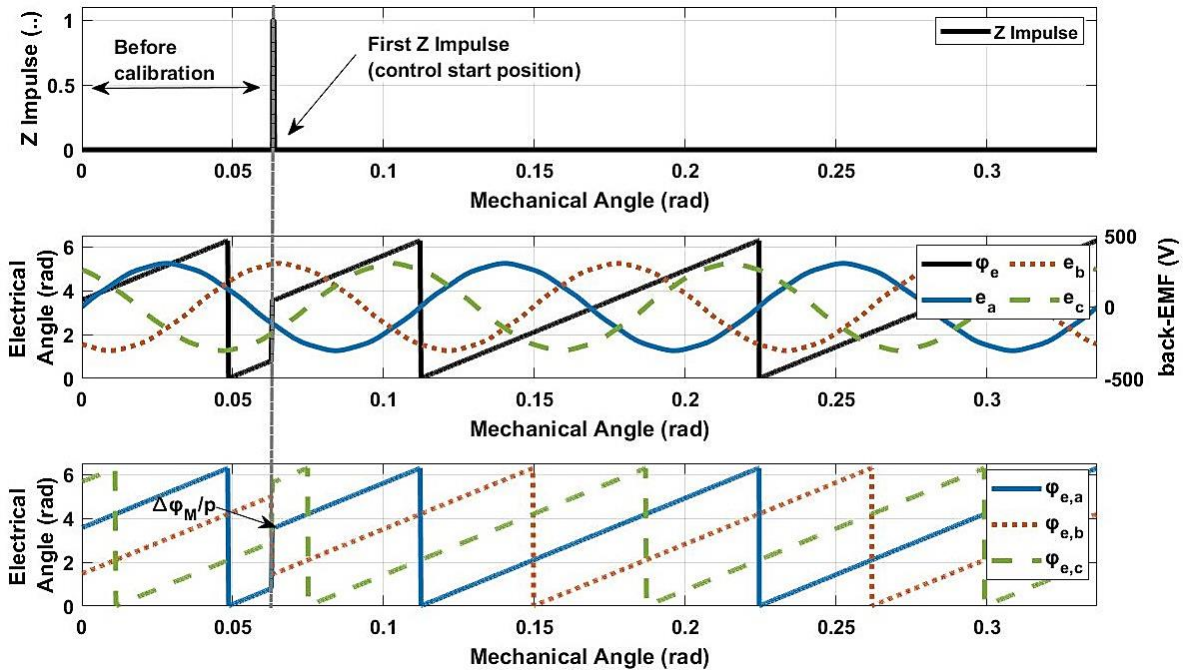


Fig. 47. Practical Implementation of the Electric Angle Estimation Process with Incremental Encoder.



However, as can be seen from the data above, the correct calculation of the electric angle by means of an incremental encoder is possible only after the first Z impulse. On the test stand, this disadvantage is not an obstacle, but during motor operation, for example in an electric vehicle, this problem will be significant. In this case, this disadvantage can be neglected by storing the rotor position value in the microcontroller memory after the engine deenergization, and it should be stored until its next start. However, the power of the microcontroller must always be on. In the event of a battery discharge, it is highly possible that the rotor position data may be lost. It means, that to start the motor, the car must be moved to the first Z impulse, which is a very inconvenient solution. An absolute encoder can solve this problem. Nevertheless, the cost of both absolute and incremental encoders is quite high.

**Absolute electrical angle estimation** also can be implemented by using low-cost analog hall sensors. For example, two analog hall sensors can be fixed to the stator phases with a shift from one another by  $90^\circ$  or  $270^\circ$  electrical degrees in order to detect the alternating magnetic field over the faces of the alternating permanent magnets as shown in Fig. 48 [119], [120].

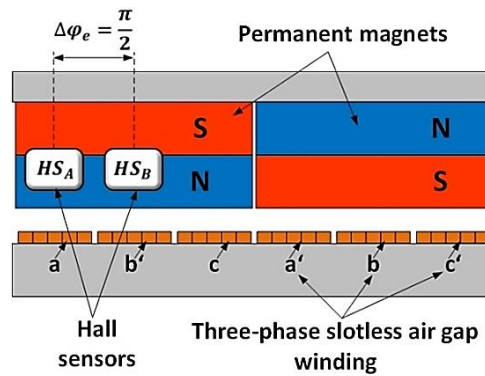


Fig. 48. Hall Sensors for Electric Angle Estimation.

In the instant case, two analog hall sensors will generate two sinusoidal signals shifted on  $90^\circ$  electrical degrees from one another and on the offset voltage relative to zero. This method makes it possible to determine the electrical angle value for any rotor position without calculation of the mechanical angle and preliminary calibration at the beginning of each motor start [119],[120]. The absolute electrical angle estimation can be carried out according to the following algorithm.

At the first stage, a filtered and digitized output signal of hall sensors  $HS_A$  and  $HS_B$  should be shifted on offset voltage value to the zero level [119]. Level shifting makes it possible to define positive and negative half-waves of the signal, which are corresponding to each permanent magnet. This step can be omitted when employing a bipolar power supply. The second step in the processing chain is the necessary standardization of the measured values [119],[120]. Due to the unequal magnetization of the permanent magnets, the high number of pole pairs and the extensity in the air gap, the maximum and minimum values of signal half-waves do not match together, which leads to the additional errors in the angle calculation. Normalized signals  $HS_{A,S}$  and  $HS_{B,S}$  in the range from zero to one as

$$HS_{A,S} = \frac{HS_A^2}{HS_A^2 + HS_B^2}$$

$$HS_{B,S} = \frac{HS_B^2}{HS_A^2 + HS_B^2}$$
(6.7)

can then be used for the electrical angle calculation. Since the inverse functions ( $\arcsin(\varphi_e)$  and  $\arccos(\varphi_e)$ ) equal to the electrical angle value give the correct values only in the corresponding quadrants, the current quadrant for the desired angle function can be determined by evaluating the signals  $HS_A$  and  $HS_B$  as shown in TABLE XI.

TABLE XI. ELECTRICAL ANGLE ESTIMATION WITH HALL SENSORS

Quadrant	$Q_1$	$Q_2$	$Q_3$	$Q_4$
Condition	$HS_A \geq 0 \ \& \ HS_B \geq 0$	$HS_A \geq 0 \ \& \ HS_B < 0$	$HS_A < 0 \ \& \ HS_B < 0$	$HS_A < 0 \ \& \ HS_B \geq 0$
Index (Online)	$HS_{A,S} \frac{N_\varphi}{4}$	$HS_{B,S} \frac{N_\varphi}{4} + \frac{N_\varphi}{4}$	$HS_{A,S} \frac{N_\varphi}{4} + \frac{2N_\varphi}{4}$	$HS_{B,S} \frac{N_\varphi}{4} + \frac{3N_\varphi}{4}$
$\varphi_{e,p}$ (Offline)	$\text{asin}(\sqrt{HS_{A,S}})$	$\text{asin}(\sqrt{HS_{B,S}}) + \frac{\pi}{2}$	$\text{asin}(\sqrt{HS_{A,S}}) + \pi$	$\text{asin}(\sqrt{HS_{B,S}}) + \frac{3\pi}{2}$

To simplify the processing chain in the microcontroller, since the calculation of root and trigonometric functions takes a long time in a standard industrial microcontroller, the preliminary value of the electrical angle  $\varphi_{e,p}$  can be calculated offline and stored in the table [119],[120]. The third stage, as shown in TABLE XI. , is the online calculation of the angle index that will correspond to the required electrical angle in the look-up table, where  $N_\varphi$  - the number of iteration points stored in the table.

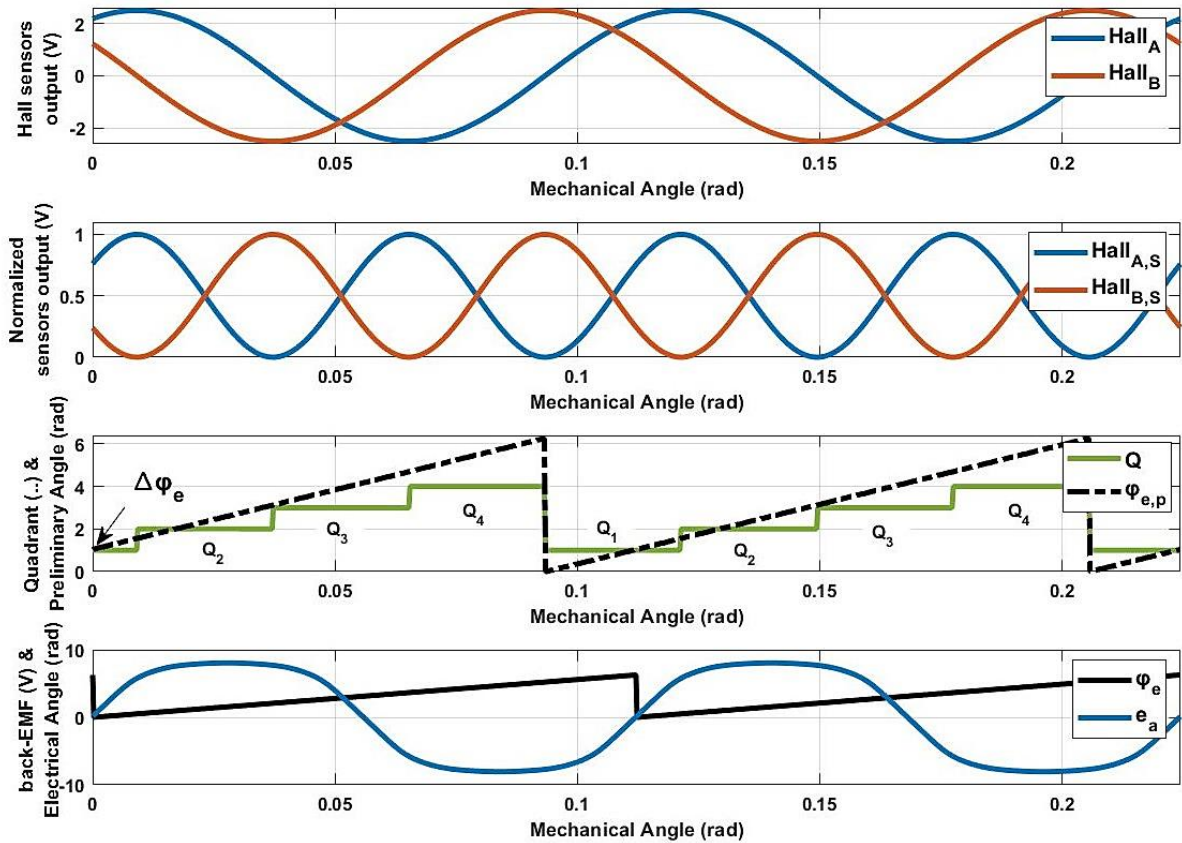


Fig. 49. Practical Implementation of the Electric Angle Estimation Process with Analog Hall Sensors.

Based on the OTMIC mathematical model, the electrical angle behavior should coincide with the back-EMF waveform of the first phase  $a$ . Therefore, the last condition in the electrical angle processing chain is shifting of  $\varphi_{e,p}$  obtained from the lookup table by the difference  $\Delta\varphi_e$  between the back-EMF  $e_a$  and the output of the first hall sensor  $Hall_A$  as

$$\varphi_e = \text{mod}((\varphi_{e,p} - \Delta\varphi_e), 2\pi). \quad (6.8)$$

In case of a high-precision motor manufacturing process this action can be neglected. The full chain of the electric angle estimation with analog hall sensors is shown in Fig. 49. However, the incremental encoder has been integrated to the test stand for verification of the proposed control system, because it gives a fairly accurate rotor position value; the angle calculation using encoder can be performed in parallel with the microcontroller operation; and the sensor calibration on the test stand can be easily carried out prior to start a motor.

## 6.2 OTMIC Control of Air Gap Winding Wheel-Hub Motor

In this chapter, the Optimal Torque and Modal Current Control of a wheel hub air gap winding PM motor for a hub-less scooter will be presented. Section 6.2.1 describes motor parameters and operation principles. The experimental setup that has been used for the proposed control verification is shown in section 6.2.2. The offline estimation of the PID control parameters and the optimal phase current waveforms is described in section 6.2.3. In the last parts of this chapter, the simulation and experimental results of the OTMIC step response will be presented, and comparison of OTMIC with torque ripples and motor losses optimization as well as FOC control during normal operation conditions with loss analyses of both control systems will be described.

### 6.2.1 Air Gap Winding Wheel-Hub Motor

In OvGU research activity, a prototype of a wheel hub motor for a hub-less scooter shown in Fig. 50 has been developed [4]. The CAD model of a scooter wheel hub motor in Fig. 50 (left) illustrates the combination of wheel and air gap winding. A disassembled motor is shown in Fig. 50 (right) for a more detailed demonstration of the air gap winding technology.

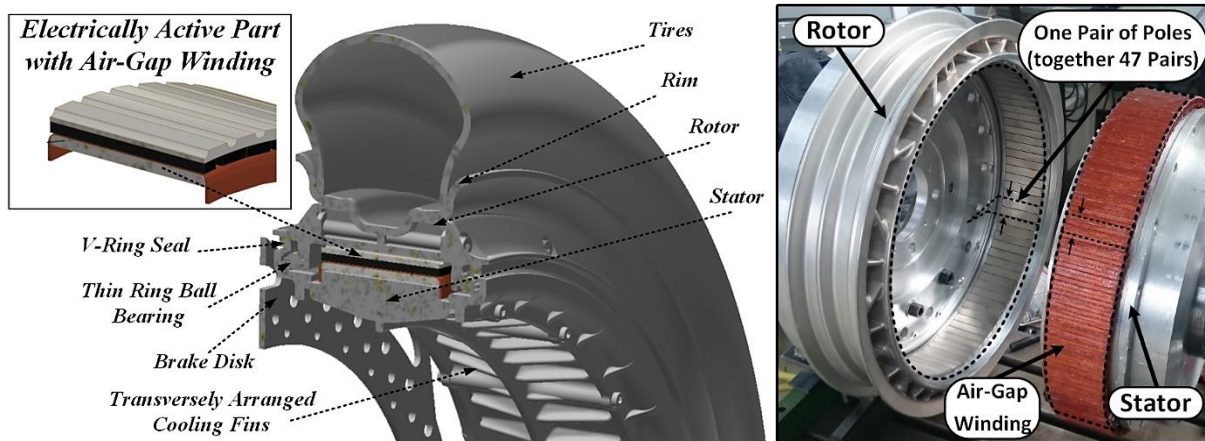


Fig. 50. Wheel Hub Motor for a Hub-Less Scooter of OvGU left: CAD Model, right: Prototype [4]

As can be seen from the figures, there are no slots in the motor, which are typical for a conventional PMSM. This design with straightforward elimination of iron significantly reduces the motor weight to 2.7 kg and at the same time allows to obtain high rated power of 5.1 kW and torque of 85 Nm.

TABLE XII. AIR GAP WINDING WHEEL-HUB-MOTOR PARAMETERS [2]

Symbol	Description	Value	UOM
$p$	Number of Poles	94	—
$k_M$	Motor Constant	0.304	Nm/(TA)
$L_s + M_s$	Phase Inductance	1.5	$\mu H$
$R_s$	Phase Resistance	0.026	$\Omega$
$t_M$	Motor Time Constant	58	$\mu s$
$u_{DC}$	DC Voltage	48	V
$\omega_{rated}$	Rated Speed	60	rad/s
$T_{rated}$	Rated Torque	85	Nm
$c$	Constant of Coulomb Friction and Hysteresis Loss	0.0832	Nm
$d$	Constant of Linear Mechanical Friction and Eddy Loss	0.0008	Nm · s/rad
$b_k$	B odd harmonics	[1.15 0.2 0.06 0.01]	

More motor data are given in TABLE XII. On the other hand, the air gap winding design leads to a very low phase inductance of 1.5  $\mu H$  and high number of poles. As was mentioned above, due to a very low inductance, the motor requires high switching frequency of about 100 kHz and a microcontroller sampling time of 10 $\mu s$  to keep current and torque ripples in an acceptable range. In addition, the non-ideal B-Field with harmonic coefficients  $b_k$  shown in TABLE XII. leads to additional torque ripples and motor losses during motor operation. Accordingly, all the above-mentioned motor features make it an ideal object for OTMIC control verification.

### 6.2.2 48V Experimental Setup

For verification of proposed Optimal Torque and Modal current Control with either optimized motor losses or torque ripples for low inductance PM motors, the experimental platform shown in Fig. 51 has been used. As it can be seen from Fig. 51, the mechanical drive train consists of an electric load machine, an incremental encoder, a speed/torque measuring shaft, two steel disk couplings and a metal angle. The latter serves as a locating bearing and holds the test specimen. The wheel hub motor with the air gap winding presented above has been connected to a 49.4 kW load motor LAK 4160-C from T-T Electric with rated torque of 312 Nm and speed of 1510  $\text{min}^{-1}$  used for speed generation [112]. The incremental encoder A02H manufactured by Fritz Kübler GmbH has been integrated in the drive train for the rotor angle measurements [110]. This accurate encoder can generate 20000 impulses per one motor revolution and 425 pulses per one pair of poles; and this is a suitable accuracy of electric angle measuring for OTMIC control of the scooter motor. The motor output torque  $T_M$  estimation has been carried out using KTR DATAFLEX 32/100 with 1 kHz cut-off frequency and measuring range of about  $\pm 100$  Nm with a linearity error including hysteresis of  $<0.1\%$  [108]. Furthermore, an integrated speed measurement with 720 pulses per revolution is included in rotating shaft and can be used up to a speed of 10000  $\text{min}^{-1}$  [108]. Overall, the torque measuring shaft has a very low mass inertia of 219  $\text{kgmm}^2$  and thus has only a very minor influence on the dynamics of the drive train. The air gap winding motor has been powered by TopCon Quadro Power Supply Unit able to generate DC voltage  $u_{DC}$  up to 60V and current  $i_{DC}$  up to 365A [111].

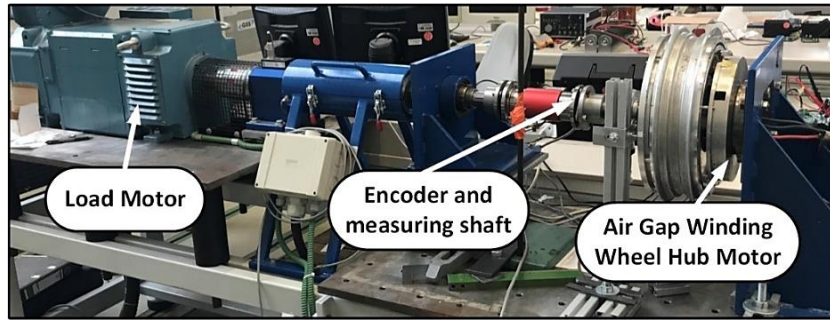


Fig. 51. Experimental Setup for 48V OTMIC Control System Verification.

The air gap winding motor control hardware is shown in Fig. 52. According to the necessity for high switching frequency due to low phase inductance to drive the motor, six GaN Systems MOSFETs GS61008P able to switch up to 90 A at a rate of up to 300 kHz [106] have been connected as B6 bridge. Due to limited cooling of the MOSFETs, phase currents have been restricted to 20 A. For phase current measurement, three Allegro ACS730 hall-effect based sensors with a very small time constant of  $1\mu\text{s}$  [107] have been used. ARM Cortex-M4F microcontroller running at 200 MHz [109] has been used for PWM signals generation to power the B6 bridge needed to put the motor in motion with a given torque  $T_{Ref}$  according to the generated speed from the load motor.

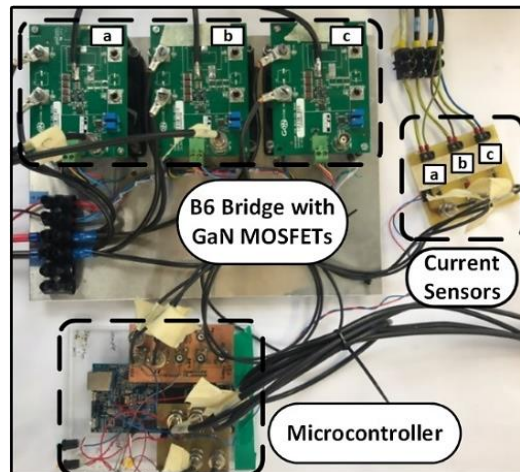


Fig. 52. Control Hardware for 48V OTMIC Control System Verification.

In the experiment, the current and torque step response have been measured and compared to simulation results. By means of the assembled experimental setup, the power supplies, the B6 bridge based on the GaN MOSFETs, the phase current sensors, the incremental encoder and the control board, the validation of the proposed OTMIC control for the air gap winding PM motor has been experimentally investigated in all four quadrants and compared to simulation results. In addition, proposed OTMIC control has been compared in simulation and experimental with conventional FOC control implemented on the same test stand.

### 6.2.3 Offline Calculation of Air Gap Winding Motor Control System

The optimal torque control for minimal motor losses proposed in Chapter 5.1 is based on the information of B-Field harmonic coefficients obtained offline from the approximation of measured back-EMF values according to (3.4) with a given motor geometric constant  $k_M$  and angular velocity  $\omega_M$ . B-Field waveform of an air gap winding wheel hub scooter motor with harmonic order  $b_k$  is shown in Fig. 11.

According to (5.9) – (5.11), it is possible to find the harmonic coefficients  $\underline{a}_L = [0.58 \ 0.03 \ 0.005 \ 0.0016]$ . This information using (5.12) gives the opportunity to estimate the three optimal phase current waveforms as a function of electrical angle and to store this data in the table offline. This table data with 1008 points per one electrical period is shown in Fig. 53 (b, left). In this way, the calculation time of the control loop in a microcontroller can be reduced. The theoretical optimal torque waveform for minimal motor losses calculated according to (3.18) with given  $\underline{K}_{opt}$ , phases B-Fields and the electrical angle as

$$T_{opt} = [B_a(\varphi_e) \ B_b(\varphi_e) \ B_c(\varphi_e)] \begin{bmatrix} K_{opt,a}(\varphi_e) \\ K_{opt,b}(\varphi_e) \\ K_{opt,c}(\varphi_e) \end{bmatrix}, \quad (6.9)$$

is shown in Fig. 53 (b, right).

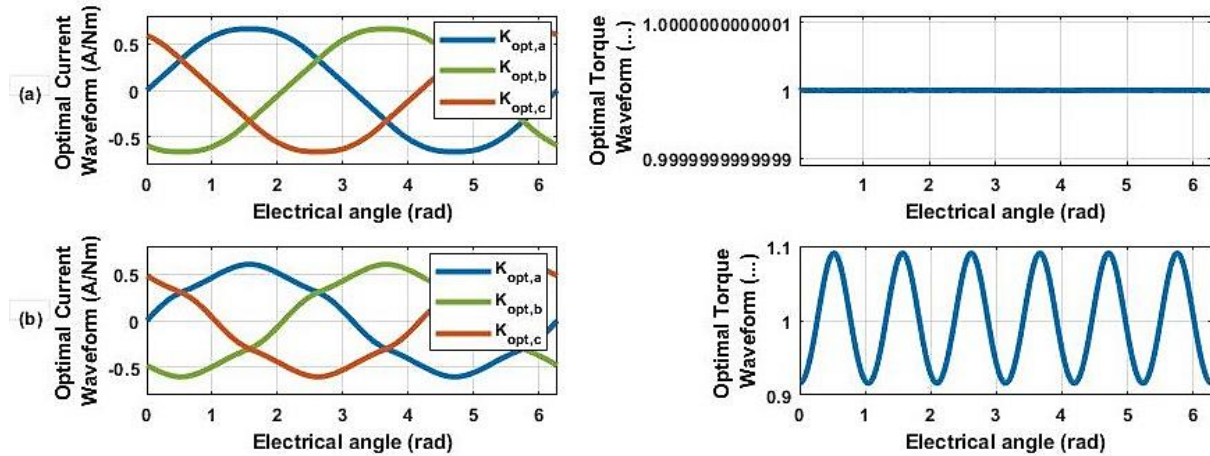


Fig. 53. Optimal Current and Torque Waveforms for (a): Minimal Torque Ripples; (b): Minimal Motor Losses.

In the same way, the optimal phase current waveforms for torque ripples reduction shown in Fig. 53 (a, left) can be found and stored in the table according to (5.17)-(5.22). The non-ideal B-Field waveform of the scooter air gap winding PM motor leads to the following harmonic coefficients of the optimal current shape for the torque ripple reduction  $\underline{a}_\tau = [0.58 \ -0.02 \ 0.0043 \ 0]$ . Thus, as it can be seen from Fig. 53 (b, right), the theoretical normalized torque does not contain any fluctuations due to compensation of additional harmonics of the B-Field.

The control parameters of PID controllers have been calculated according to (5.38) with the given motor parameters, sampling time, requested and current sensor time constants and are shown in TABLE XIII.

TABLE XIII. PID CONTROL SYSTEM PARAMETERS

Symbol	Description	Value	UOM
$K_P$	Proportional Term	0.1713	V/A
$K_I$	Integral Term	0.026	V/A
$K_D$	Derivative Term	0.041	V/A
$N_D$	PID Filter Term	0.74	—
$t_S$	Sensor Time Constant	1	$\mu s$
$\Delta t$	Sampling Time	10	$\mu s$
$f_{PWM}$	Switching Frequency	100	kHz
$f_{AAF}$	AAF Filter Frequency	50	kHz
$t_{Req}$	Requested Time Constant	20	$\mu s$

The bode diagram of discrete open loop transfer function  $D_{MS}(z)D_C(z)$  calculated according to (5.34) and (5.35) with the PID controller parameters in TABLE XIII. and presented in Fig. 54 (above) shows that the phase margin (PHM) according to the system 0dB crossing in the magnitude diagram is 8.3 degrees. The magnitude margin (GM) according to -180 deg of the phase diagram and the frequency of 200 krad/s is 2.7 dB that confirms the system stability considering the rated angular velocity of 1410 rad/s.

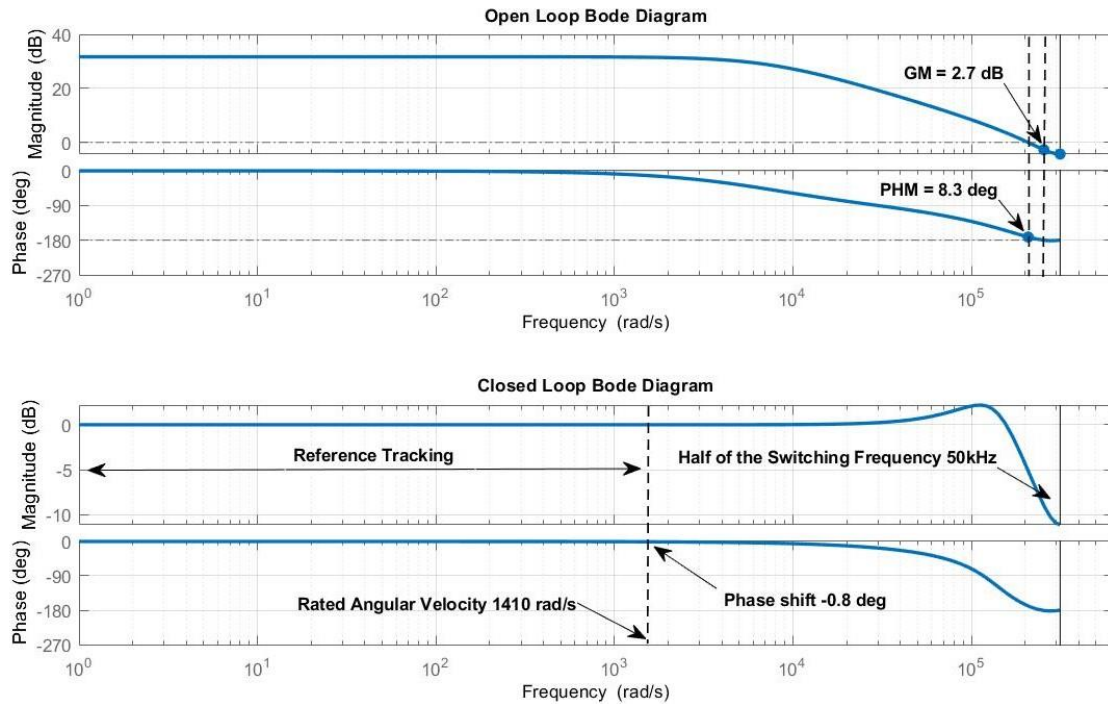


Fig. 54. Open/Closed Loop Bode Diagrams of OTMIC Control for Air Gap Winding Wheel-Hub Motor.

The discrete closed loop bode diagram of transfer function (5.36) illustrated in Fig. 54 (below) shows the small phase shift of -0.8 deg at the rated motor speed. This phase shift is small enough and cannot bring the system out of stability. In the worst case, it can lead to small additional harmonics in the phase current and torque waveforms that will be confirmed in Chapter 6.2.5.

## 6.2.4 Step Response of OTMIC Control

The motor dynamic behavior depends on motor parameters, sensors qualities or load, can be verified by means of phase currents  $\underline{i}$  and electrical torque  $T_E$  step response. Comparison of phase currents and torque measurement and simulation for OTMIC control used for scooter air gap winding PM motor carried out according to zero velocity and 5 Nm reference torque  $T_{Ref}$  (green) is shown in Fig. 55. The exciting fast phase current response shown in Fig. 55 (below) within only 35  $\mu$ s leads to the very high dynamics of this motor. The slight difference between the simulated (light colors) and the measured (dark colors) results stems from parasitic inductances and capacitances in power lines and supply, which affect the system due to the very low motor inductance of 1.5  $\mu$ H. Due to too low torque sensor bandwidth for this experiment, the electrical torque generated in the air gap winding  $T_E$  (blue), compared with the simulation results (red) and shown in Fig. 55 (above) has been estimated using the torque equation (3.8) taking into account the values of the measured phase currents, electric angle with the given motor geometric constant  $k_M$  and harmonic coefficients of B-Filed  $\underline{b}_k$ . Because of a very large

time constant of torque measuring rotating shaft about 1ms [108] compared to a very fast step response of the electrical torque, the motor output torque measurement  $T_M$  (violet) is defined by significantly increased response time. However, considering the torque sensor response time and (3.7)-(3.9), the simulation results can be confirmed with the measured output torque.

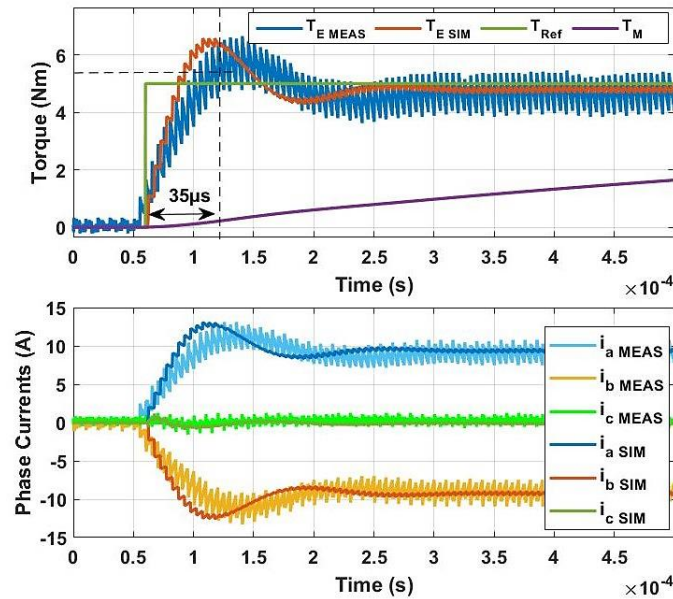


Fig. 55. Step Response of Simulation and Measured Phase Currents and Electrical Torque.

The simulated and measured signals of the control algorithm occurring in the microcontroller during the step response are shown in Fig. 56.

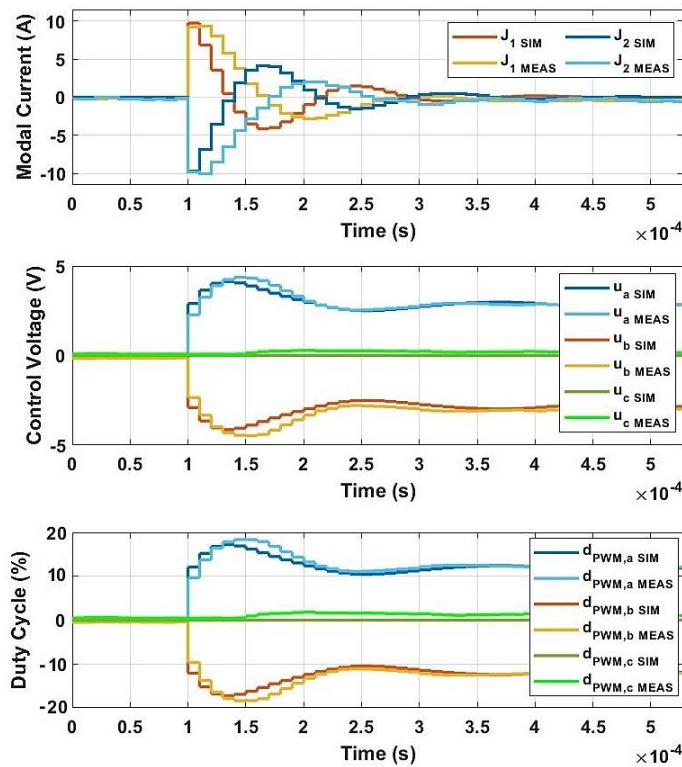


Fig. 56. Calculation Process of OTMIC Control Algorithm in the Microcontroller during Step Response.



As it can be seen from Fig. 56, mismatches between the simulation and experiment behaviors of modal currents  $J_1, J_2$ , control voltages  $u_a, u_b, u_c$  and duty cycles  $d_{PWM,a}, d_{PWM,b}, d_{PWM,c}$  are minimal, which emphasizes the high dynamics of the proposed system despite interference in the feedback circuit, parasitic inductance and capacitance and very low motor inductance.

### 6.2.5 Air Gap Winding Motor under Normal Operating Conditions

The simulation results of phase currents and electrical torque  $T_E$  during the normal operation of the proposed OTMIC control with (TRO) minimization of torque ripple (a) and (LO) minimization of motor losses (b) in comparison to the conventional FOC method (c) correspond to the references:  $\omega_M = 8 \text{ rad/s}$  and  $T_{Ref} = 10 \text{ Nm}$  are shown in Fig. 57. The first thing that can be noted from the simulation results is near-zero fluctuations of RMS torque value for OTMIC in contrast to the Field Oriented Control. This fact can also be confirmed by the current and torque harmonic distribution for the control approaches as shown in Fig. 57 (d). The amplitude of each harmonic component of torque and phase current waveforms is normalized in respect of fundamental one. The FFT analyses of the simulation phase currents and electrical torque underline and confirm the main idea of the proposed Optimal Torque and Modal Current Control method. According to the offline calculations described in Chapter 6.2.3, the phase current waveforms of the OTMIC control (blue and green) during normal operation have 5<sup>th</sup> and 7<sup>th</sup> harmonics as opposed to the conventional FOC control (red) as shown in Fig. 57 (d, left). This approach eliminates the identical harmonics from the torque waveform and minimizes the torque fluctuations. Thus, as it can be seen from Fig. 57 (d, right), the torque waveform of OTMIC with torque ripple optimization (blue) has near-zero additional harmonics as opposed to FOC control.

Measured phase currents and output torque  $T_M$  for OTMIC with TRO (a) and LO (b) versus the conventional FOC (c) are shown in Fig. 58. In opposite to the simulation results shown in Fig. 58, the behavior of output torque and phase currents for the proposed OTMIC control methods has a slight asymmetry due to a non-ideal speed reference by means of a load motor and errors in current and electrical angle measurements that could not have been completely avoided in the experimental platform. However, the measured results confirm the theoretical computations with a very good accuracy, that can be further validated with FFT analyses of the measured phase currents (left) and torque (right) shown in Fig. 58 (d) for both OTMIC methods and FOC. It can be noted that, during OTMIC control, the measured phase current has predetermined 5<sup>th</sup> and 7<sup>th</sup> harmonics. In case of OTMIC with TRO, this leads to compensation for additional parasitic harmonics as shown in Fig. 58 (d, right, blue). The phase current harmonic spectrum of OTMIC approaches has parasitical 2<sup>d</sup>, 4<sup>th</sup> and 6<sup>th</sup> harmonics. Respectively, a torque waveform consists of parasitical 2<sup>d</sup>, 3<sup>d</sup>, 4<sup>th</sup> and 5<sup>th</sup> harmonics due to inaccuracies in OTMIC control system and power lines. However, the values of these harmonics are less than 1% of the fundamental one and don't affect the system.

The output torque  $T_M$  measurements are shown in Fig. 59 (right) for OTMIC (a, b) and FOC (c). According to (3.7)-(3.9), an output torque consists of an electrical torque  $T_E$  reduced by the total loss torque  $T_L$  and a load. In addition, torque transducer errors also affect the accuracy in torque waveform measuring. Taking this information into account for better verification of the proposed control, the simulated RMS values of the electrical torque  $T_E$  for both OTMIC and FOC methods (a) can be compared to the measured electrical torque waveforms (b) as shown in Fig. 59. The experimental waveforms of an electrical torque can be found according to (3.8) as a function of an electrical angle with measured phase currents and B-Field harmonic coefficients.

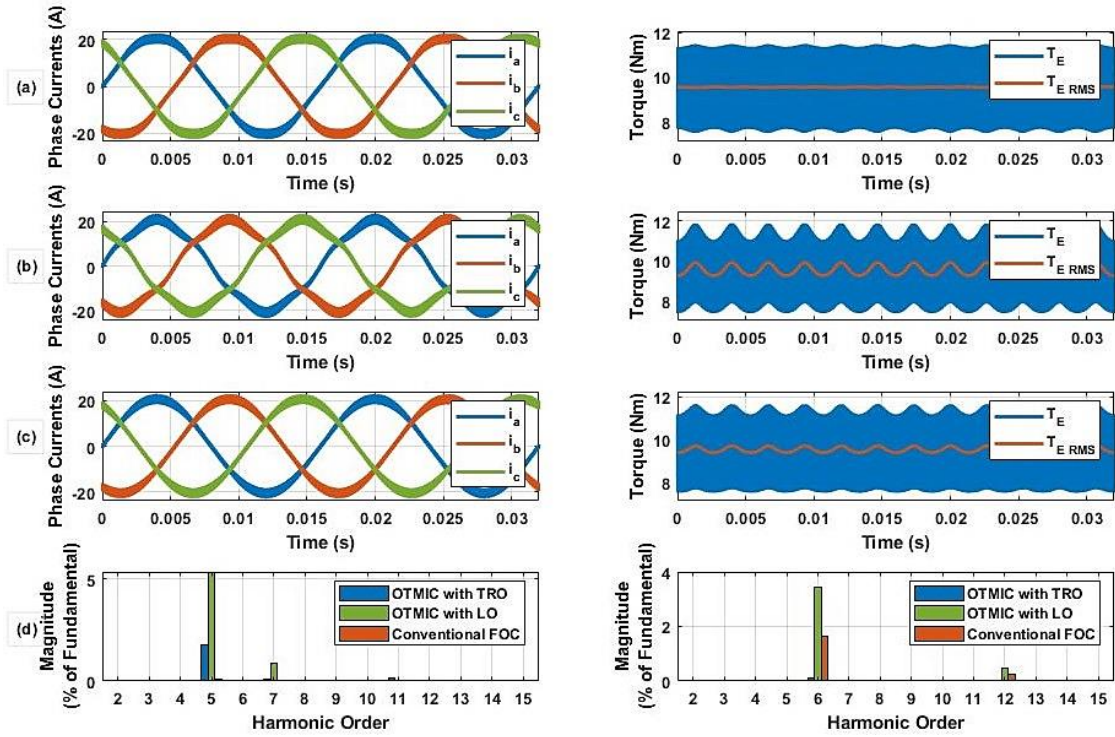


Fig. 57. Simulated Phase Currents and Electrical Torque  $T_E$  of (a): OTMIC with Torque Ripple Optimization; (b): OTMIC with Losses Optimization; (c): Conventional FOC control. (d): Harmonic Spectrum of Phase Current (left) and Torque (right) for Every Method.

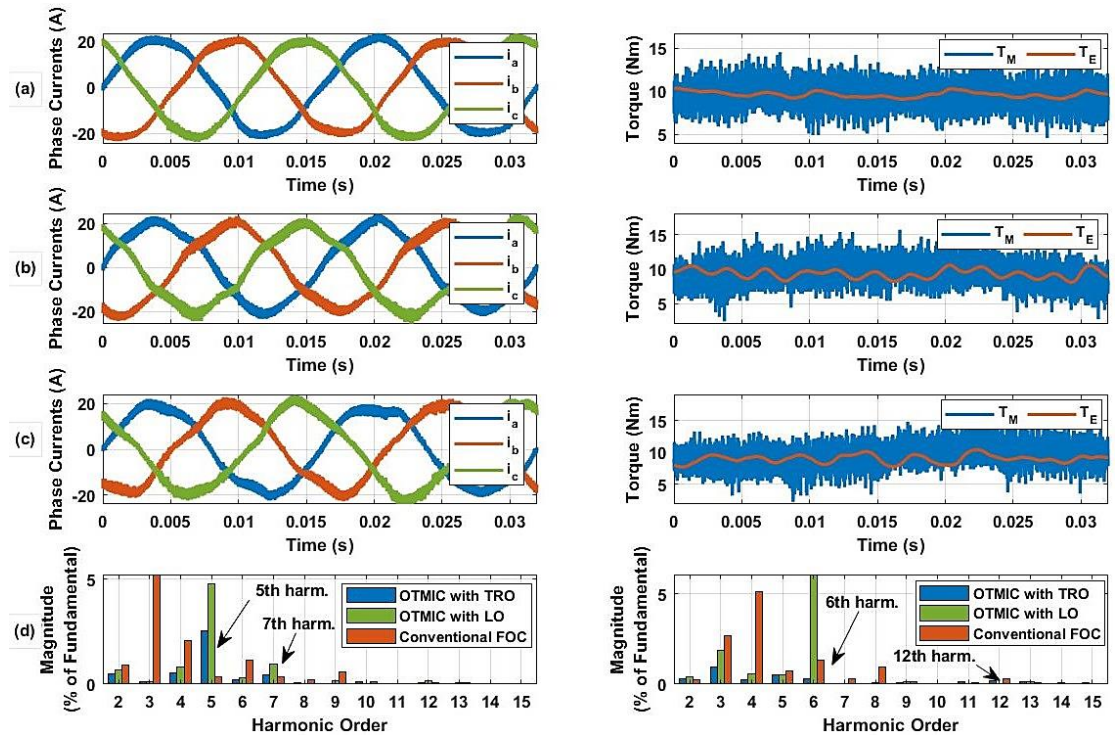


Fig. 58. Experimental Results of Measured Phase Currents and Output Torque  $T_M$  of (a): OTMIC with Torque Ripple Optimization; (b): OTMIC with Losses Optimization; (c): Conventional FOC Control. (d): Harmonic Spectrum of Phase Current (left) and Torque (right) for Every Method.

The simulated RMS waveform of the electrical torque for OTMIC with torque ripples minimization (blue) underline near-zero torque fluctuations in comparison to the conventional FOC control (red). These relationships can also be confirmed by the experimental results of the electrical torque shown in Fig. 59 (b). The behavior of the measured torque shows slight larger torque ripples of OTMIC control in comparison to the simulation caused by influence of the load motor, errors in the electrical angle and the current measurement. However, the experimental results underline the effectiveness of the proposed OTMIC control in comparison to the conventional FOC method.

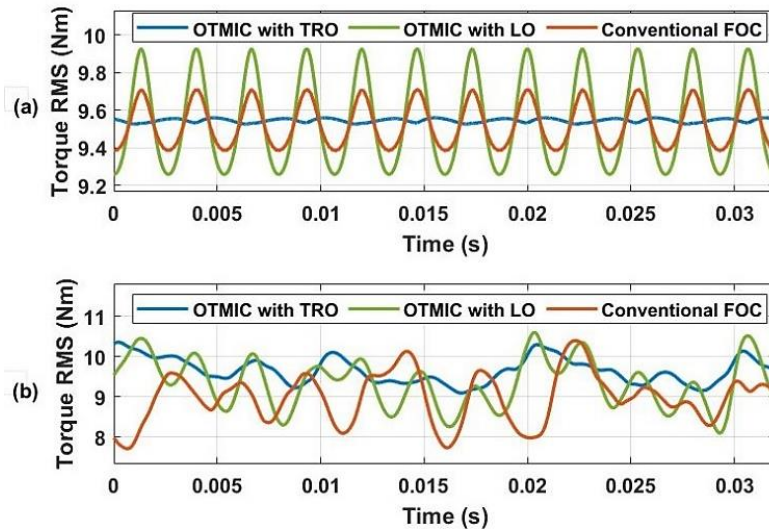


Fig. 59. Validation of Torque Ripples for every Method (a): Simulated RMS Value of Electrical Torque; (b): Measured RMS Value of Electrical Torque.

Due to limited capabilities of power electronics related to cooling of transistors [105], the phase current has been restricted to 20A. The simulation results under the normal operating conditions with rated motor power ( $\omega_M = 60 \text{ rad/s}$ ,  $T_{Ref} = 85 \text{ Nm}$ ) are shown in Fig. 60 for OTMIC with torque ripple reduction (a) and the conventional FOC (b) methods.

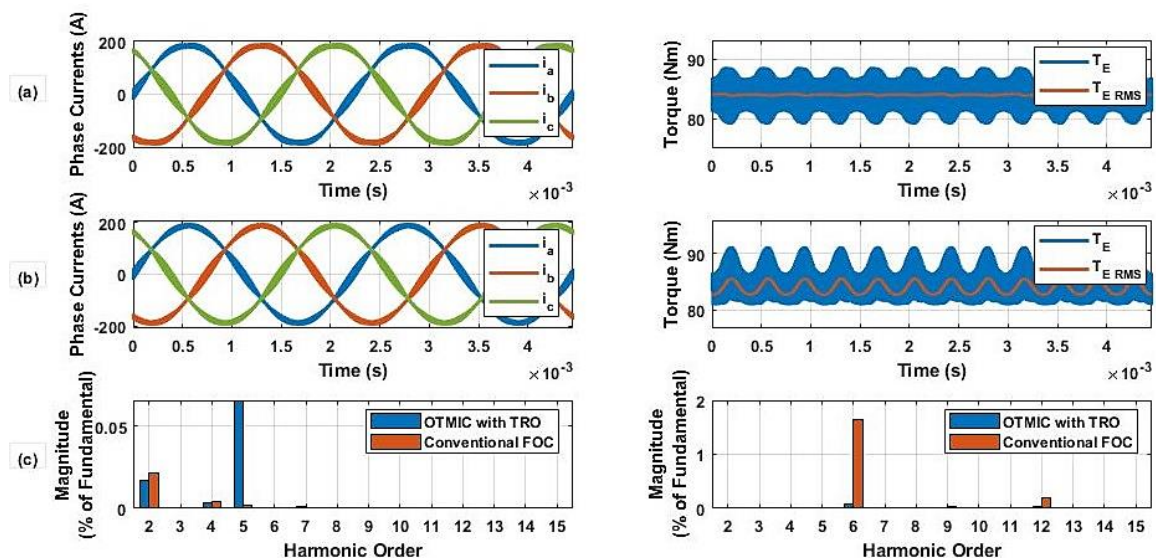


Fig. 60. Simulation Results of Phase Currents and Torque During normal Operation with Rated Power of Air Gap Winding Motor (a): OTMIC with Torque Ripple Optimization; (b): Conventional FOC Control. (c): Harmonic spectrum of Phase Current (left) and Torque (right) for Every Method.

It can be noted, that raise of an angular velocity and reference torque leads to increase of torque fluctuations for the proposed and the conventional approaches. Nevertheless, in an ideal system, the OTMIC control with TRO retains its benefits. In addition, these results can be validated with FFT analyses of the simulated phase current and electrical torque presented in Fig. 60 (c).

Considering the above experimental results, it can be summarized, that in a real system, in the absence of interference in the current and electrical angle measurement, the advantages of OTMIC for air gap winding PM motor control will be more significant. Thus, the effectiveness of the proposed Optimal Torque and Modal Current Control approach has been confirmed in simulation and during the experiment with FFT analyses and by direct comparison of torque fluctuations. In addition, the proposed OTMIC method shows better torque and phase current behaviors compared to the conventional Field Oriented Control in simulation and in practice.

### 6.2.6 Losses in Air Gap Winding Wheel-Hub Motor

The Optimal Torque and Modal Current Control with motor loss minimization based on optimization of phase current waveforms is able to improve loss rates and system efficiency. Slight disadvantage of this method is minor increase of torque ripples, which can possibly be reflected in the increased noise during the normal operation. The theoretical calculation of ohmic losses according to (3.18) compared to measurements for OTMIC with loss optimization (green), torque ripple reduction (blue) and conventional FOC (red) control systems are shown in Fig. 61. Ohmic losses have been estimated and measured with the given angular velocity  $\omega_M = 8 \text{ rad/s}$  and the range of reference torque from  $T_{Ref} = 1..10 \text{ Nm}$ . The ohmic losses simulation (left) together with the simulation of torque ripples in Fig. 61 describes a comparison between both optimization problems and the conventional FOC. It can be seen that reduction of torque ripples leads to increase of motor losses and vice versa. A traditional vector control approach gives the average values of losses und torque ripples in comparison to OTMIC. However, verification of these methods with an air gap winding PM motor confirms these results only for the proposed OTMIC control. Ohmic losses in case of the FOC control exceed the theoretical results and measured loss values for both OTMIC methods. It stems from the fact that phase current waveforms during the normal operating conditions of the conventional FOC are not sinusoidal and have enormous high fluctuations. According to the simulation and experimental results for the same torque reference, the OTMIC control makes it possible to reduce the motor losses to 9.5% in theory and to 11% in practice.

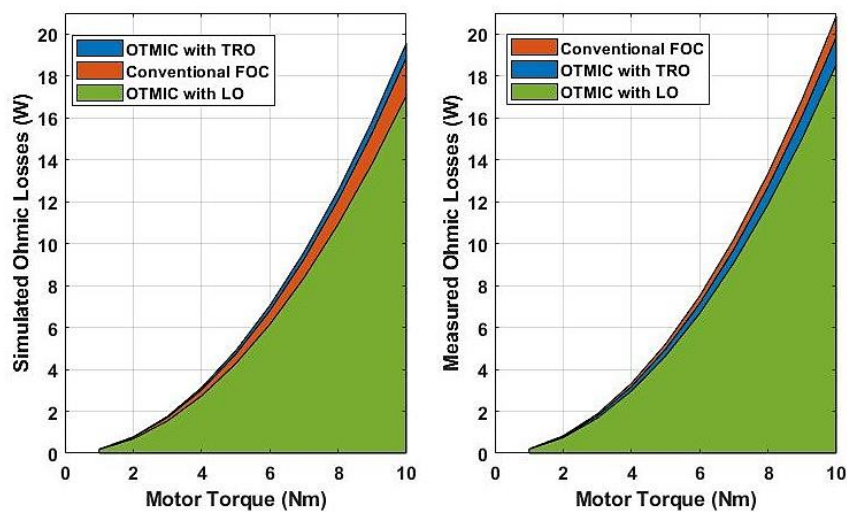


Fig. 61. Ohmic Motor Losses Simulation for OTMIC and FOC Control Methods

Thus, it can be concluded that for an air gap winding PM motor with a very low phase inductance and high number of pole pairs, traditional control methods like FOC are specified by deviations in the actual current and torque values from the references, and need to be improved, that requires a higher computation ability of a microprocessor. Verification of the proposed OTMIC control shows better resemblance of measured values to theoretical ones. OTMIC with motor loss optimization can be used in case, when it is necessary to reduce a motor loss and increase its efficiency. This will result in a slight increase in noises during PMSM operation. On the other hand, the operation noises can be reduced by minimization of the torque ripple with a slight increase of the system loss. During the normal motor operation, switching between these two optimization approaches can be easily done by replacing one table of optimal phase current waveforms with another.

### 6.3 OTMIC Control of Combined Winding Wheel-Hub Motor

According to [12], the mathematical model of combined winding PMSM can also be described with (3.1)-(3.6), (3.8) and (3.9) taking into consideration, that electrical torque consists of first torque provided by the Lorentz force generated by the B-field in air-gap and additional torque provided by the B-field in the stator back-iron. The total phase inductance  $L_s$ , the total phase resistance  $R_s$  and the total back-EMF values  $\underline{e}$  of both windings can be described as a sum of inductances (with additional contribution of mutual-inductances), resistances and back-EMF values of the air gap winding and the slot winding respectively [12]. The output torque

$$T_M = T_E - T_L + T_C = T_E - T_L + \sum_k a_{ck} \cos(6k\varphi_e) - \sum_k b_{ck} \sin(6k\varphi_e) \quad (6.10)$$

is given by the sum of electrical torque  $T_E$  and the cogging torque  $T_C$  reduced by a loss torque  $T_L$ , where  $a_{ck}$  and  $b_{ck}$  are harmonic coefficients. According to [12]  $T_E$  can be calculated according to (3.8) considering that B-Fields in the air gap and in the stator back-iron are almost identical. However, the torque minimization algorithm presented in Chapter 5.2 does not consider cogging torque. It means the additional torque fluctuations equal to cogging torque as a function of electrical angle even using the torque optimization algorithm. Nevertheless, this problem is not a part of this work and may be solved in the future by optimal slots filling or by including the cogging torque mathematical model based on the harmonic coefficients  $a_{ck}$  and  $b_{ck}$  and described in (6.10) into (5.14).

This chapter presents verification of the Optimal Torque and Modal Current Control algorithm in case of its use for control of combined winding wheel hub motor for an electric automobile. A combined winding PM motor will be described in section 6.3.1. The experimental setup that has been used for the proposed control verification is presented in section 6.3.2. Section 6.3.3 describes the estimation of PID control parameters and the optimal phase current waveforms for torque ripples reduction. The simulation and experimental results of OTMIC control in comparison to the conventional Field Oriented Control during normal operation conditions will be presented in the last part of this chapter.

#### 6.3.1 Combined Winding Wheel-Hub Motor

High-speed electric drives used in electric vehicles operate with high supply DC voltage value in the average range from 450 to 650V to overcome a back-EMF and to set a required torque reference. As it has been mentioned above, the air gap winding technology provides high specific torque and power densities of the motor. However, absence of slots leads to the very low motor inductance, and high-speed systems with supply voltage of over 100V and a vector control require an excessively high

switching frequency of approximately between 200 – 300 kHz to keep currents and torque ripples in the acceptable range [13]. Inverters available nowadays cannot operate with these required frequencies and high rated current over 100A in the same time. Thus, a solution for this drawback is either to change a vector control with a commutation control combined with a buck-boost converter, or to increase the phase inductance by adding slots to a stator geometry. Nevertheless, the algorithm of a buck-boost converter optimization described in Chapter 4 is able to minimize only switching current ripples. The phase current ripples during commutation time remain high, and their values increase with increase of supply DC voltage or the reference motor torque.

Thus, a new concept for very lightweight wheel-hub motors based on the combined slots and air gap winding technology presented by OvGU University in [3], [12] offers the greatest promise as an electric drive for high-voltage mobile application. Slight increase in the motor weight in comparison to the winding technology combined with the air gap winding design increases phase inductance and allows to use vector or OTMIC control based on inverters, available today, with a switching frequency in the range of 100 kHz. Moreover, combined winding design allows to increase the motor rated power and torque of two times in comparison with the air gap winding design [12]. Thus, the combined winding technology allows to maintain the advantages of the air gap winding in high specific torque and power densities of the motor and makes it possible to implement the control system proposed in Chapter 5. A prototype of the combined winding wheel hub motor for an electric car has been developed in OvGU research activity and shown in Fig. 62 (right) with its CAD model (left). The motor stator is shown in Fig. 62 (middle) for a more detailed presentation of the combined winding, which consists of slots and the air gap winding connected in series.

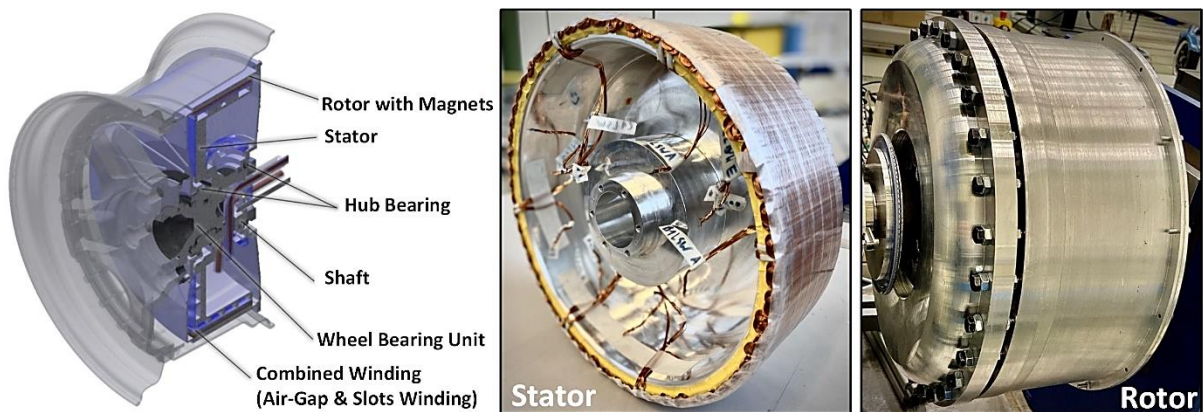


Fig. 62. Combined Winding Wheel Hub Motor of OvGU, left: CAD model, right: Prototype [6].

The combined winding technology with a straightforward elimination of the stator iron significantly reduces the motor weight to 16 kg while providing high rated power of 70 kW and torque of 600 Nm, and in addition increases the phase inductance to 45  $\mu\text{H}$ . The prototype of a wheel hub motor with the combined winding has a specific torque and power densities of 37.5 Nm/kg and 4.38 kW/kg, respectively, which is two times higher than other engines on the market today [3]. More wheel hub motor data are listed in TABLE XIV.

TABLE XIV. COMBINED WINDING WHEEL-HUB-MOTOR PARAMETERS [6]

Symbol	Description	Value	UOM
$p$	Number of Poles	112	—
$k_M$	Motor Constant	3.66	Nm/(TA)
$L_s + M_s$	Phase Inductance	45	$\mu H$
$R_s$	Phase Resistance	0.234	$\Omega$
$t_M$	Motor Time Constant	192.3	$\mu s$
$u_{DC}$	DC Voltage	650	V
$\omega_{rated}$	Rated Speed	115	rad/s
$T_{rated}$	Rated Torque	600	Nm
$c$	Constant of Coulomb Friction and Hysteresis Loss	4.3	Nm
$d$	Constant of Linear Mechanical Friction and Eddy Loss	0.08	Nm · s/rad
$\underline{b}_k$	B odd harmonics	[0.78 0.02 0.008 0.001]	

Nevertheless, the motor phase inductance remains low in comparison with the conventional slotted PMSM and requires 100 kHz switching frequency to keep phase current ripples approximately in the range under 5A, the same as in the previous 48V control system. In addition, the combined winding technology, due to small slots, produces slight but noticeable cogging torque that affects the system in the low speed range. However, it does not introduce significant errors into the system.

### 6.3.2 650V Experimental Setup

For verification of the Optimal Torque and Modal current Control proposed in Chapter 5 with torque ripples minimization in case its implementation for a 650V wheel hub motor with the combined winding, the experimental setup shown in Fig. 63 has been used. The experimental platform consists of the same load motor described in the previous experimental setup and used for speed generation, an incremental encoder A02H manufactured by Fritz Kübler GmbH, a Lorenz DR-2212 torque transducer with the measurement range of about  $\pm 500$  Nm and maximal speed of  $7000 \text{ min}^{-1}$  for the motor output torque measurements [113], and TopCon Quadro Power Supply capable to generate DC voltage up to 600V and current up to 60A [111].

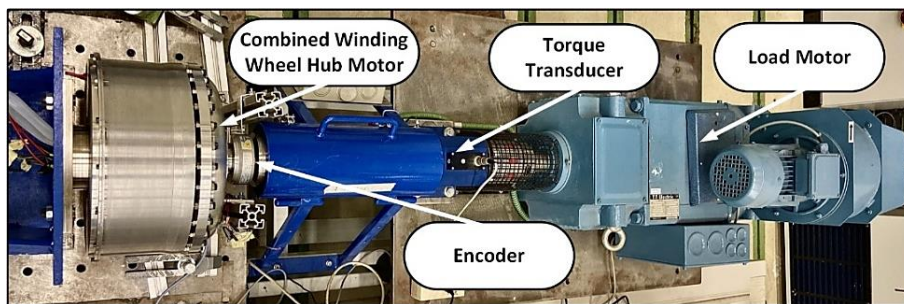


Fig. 63. Experimental Setup for 650V OTMIC Control System Verification.

The same ARM Cortex-M4F microcontroller and Allegro ACS730 current sensors as in the previous 48V system have been used. The inverter for the combined winding wheel hub motor shown in Fig. 64 has been obtained by connecting three single phase B2 modules made by GaN Systems with GaN MOSFETs GS66508T capable to switch up to 30 A at a rate of up to 300 kHz with 650V [106]. Phase current has been limited to 20A in amplitude due to limited cooling.

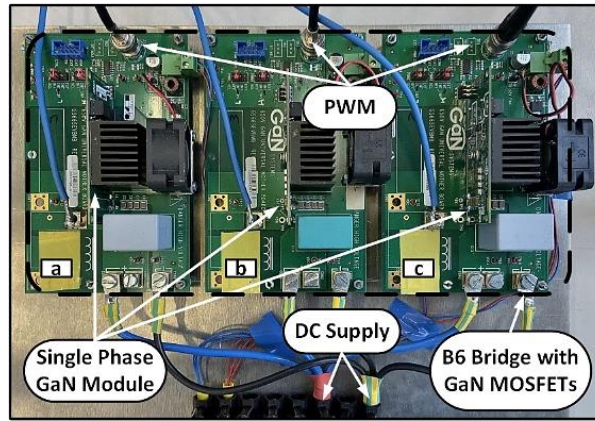


Fig. 64. Motor Control Hardware for 650V OTMIC Control System Verification.

The validation of OTMIC control with torque ripple optimization for a combined winding wheel hub motor has been investigated in all four quadrants using the assembled experimental platform and the B6 bridge based on the GaN MOSFETs with a control board, current sensors and an incremental encoder. On the one hand, the simulated OTMIC model have been verified with the experimental results. On the other hand, the OTMIC control has been compared to the conventional Field Oriented Control in simulation and in practice.

### 6.3.3 Offline Calculation of Combined Winding Motor Control System

The optimal phase current for torque ripples minimization of a combined winding motor can be calculated similarly with offline torque ripples optimization of an air gap winding motor presented in Chapter 6.2.3. The non-ideal B-Field with its additional harmonic coefficients of the combined winding motor is presented in Fig. 65 (left). According to (5.17) - (5.22), the optimal phase current coefficients for torque ripple reduction are  $\underline{a}_\tau = [0.855 \quad -0.016 \quad -0.0073 \quad 0.002]$ . Thus, Fig. 65 (right) shows the reference phase current waveforms and theoretical normalized electrical torque with zero fluctuations due to compensation of additional B-Field harmonics.

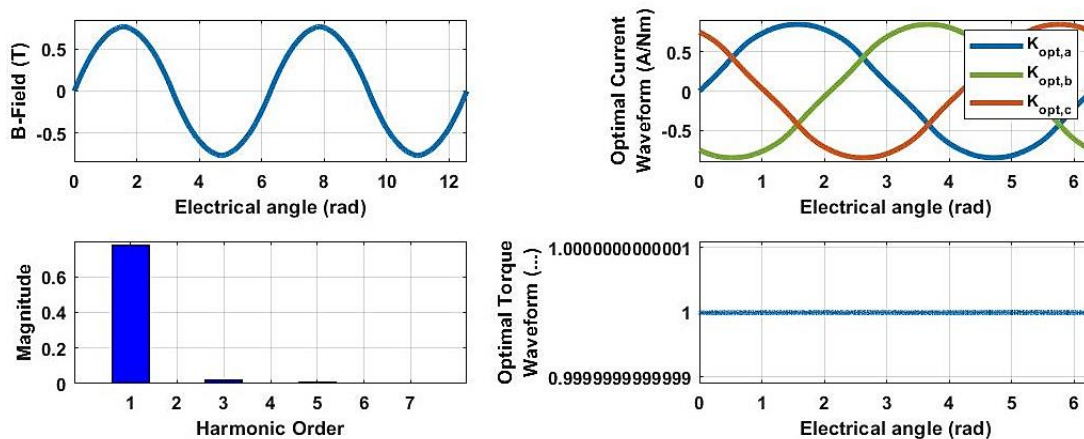


Fig. 65. B-field in a Combined Winding with its Harmonic Spectrum (left). Optimal Current and Torque Waveforms for a Combined Winding Motor (right).

The PID controller parameters have also been calculated according to (5.38) with parameters listed in TABLE XV.



TABLE XV. CONTROL SYSTEM PARAMETERS FOR COMBINED WINDING MOTOR

Symbol	Description	Value	
$K_P$	Proportional Term	4.7	V/A
$K_I$	Integral Term	0.234	V/A
$K_D$	Derivative Term	1.4	V/A
$N_D$	PID Filter Term	0.73	-
$t_S$	Sensor Time Constant	1	$\mu s$
$\Delta t$	Sampling Time	10	$\mu s$
$f_{PWM}$	Switching Frequency	100	kHz
$f_{AAF}$	AAF Filter Frequency	50	kHz
$t_{Req}$	Requested Time Constant	20	$\mu s$

The discrete open loop transfer function  $D_{MS}(z)D_C(z)$  calculated according to (5.34) and (5.35) with the parameters in TABLE XIII. can be described with the bode diagram presented in Fig. 66 (above). The results show the very good phase margin (PHM) of 93.5 deg and magnitude margin (GM) of 24.7 dB according to the frequencies 250 krad/s and 215 krad/s, respectively. In addition, these values are far from the rated angular velocity of 3220 rad/s. This confirms the system stability and robustness to changes in the system parameters and gains.

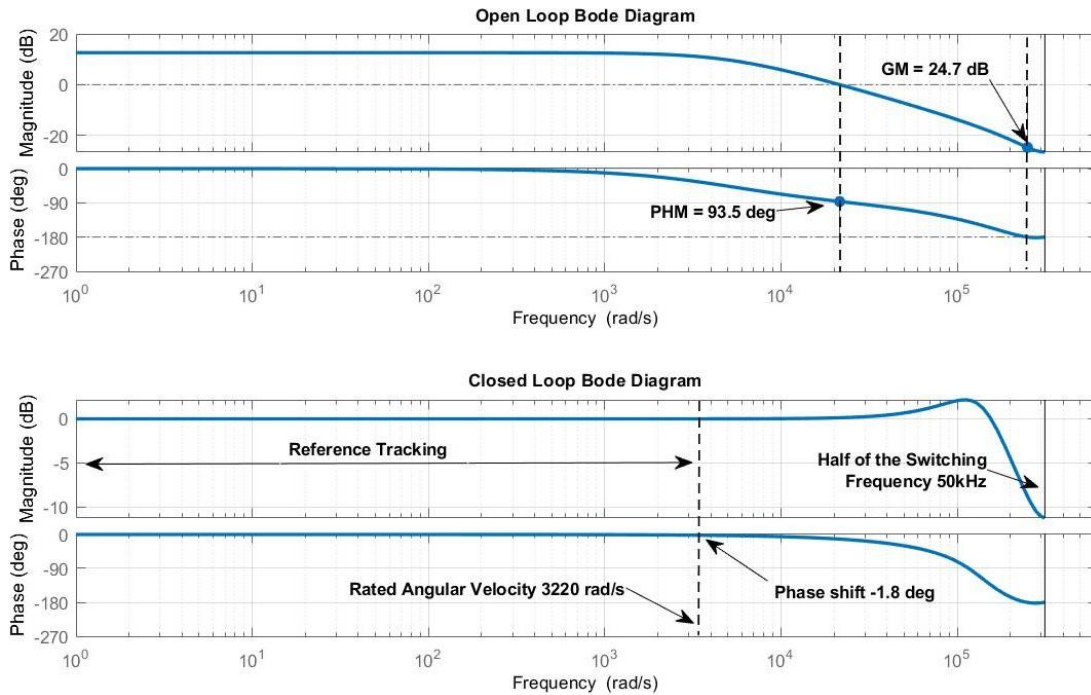


Fig. 66. Open/Closed Loop Bode Diagrams of OTMIC Control for Combined Winding Wheel-Hub Motor.

The discrete closed loop transfer function  $D(z)$  calculated according to (5.36), described with the bode diagram and presented in Fig. 66 (below) shows a much higher phase shift of -1.8 deg corresponding to the rated speed in comparison to the control system of the air gap winding motor. As the simulation results show, this phase shift cannot bring the system out of stability and robustness. However, it may lead to additional harmonics in electrical torque and phase currents that will be uncompensated by the PID controller. Furthermore, based on the bode diagrams of a closed loop function of OTMIC control for air gap and combined winding motors operated with rated speeds of 60 rad/s and 115 rad/s and presented in Fig. 54 and Fig. 66, respectively, it follows that the system stability is limited by rotational

speed. However, OTMIC control structure allows to estimate the limits of its stability faster and easier if compared to the other conventional control methods. The influence of the phase shift illustrated on the bode diagram of a closed loop transfer function of the motor torque will be presented in the next chapter based on the simulation results of the combined winding motor operation at the rated power.

### 6.3.4 Combined Winding Motor under Normal Operating Conditions

In correspondence with the references  $\omega_M = 8 \text{ rad/s}$  and  $T_{Ref} = 100 \text{ Nm}$ , Fig. 67 shows the phase currents and electrical torque  $T_E$  simulation results during normal operation of the proposal OTMIC (TRO) control with torque ripple optimization (a) in comparison to the conventional FOC method (b). As in case with the 48V control system, the same trend is observed in these simulation results of ideal control systems. Torque RMS value fluctuations of OTMIC are zero in contrast to the conventional FOC. However, due to a more sinusoidal B-field waveform compared to the air gap winding motor due to use a Halbach array magnetization principle, that emphasize the values of the B-field harmonic coefficients presented in the TABLE XIV. , the simulated torque RMS waveform of FOC is also insignificant. These results can be confirmed by the OTMIC and FOC current and torque harmonic distribution shown in Fig. 67 (d) that shows the magnitude of 6<sup>th</sup> harmonic equal 0.2% of the fundamental one for FOC control. However, it can be noted that these results, which from the first glance demonstrate a minimum difference between the proposed and the generally accepted method, in fact only emphasize the advantage of the OTMIC. In case of a perfect sinusoidal B-field waveform, both methods give the same results in ideal simulation models. In practice, this condition cannot be investigated due to the non-ideal permanent magnets and other inaccuracies during motor production, which underlines the importance of the proposed method. In addition, as shown in Fig. 67 (c, left), the phase currents of OTMIC control (blue) have 5<sup>th</sup> and 7<sup>th</sup> harmonics in contrast to the conventional FOC (red). Additional harmonics in current waveform eliminate the identical harmonics in torque waveform, while minimizing the torque ripples that can be confirmed by Fig. 67 (c, right).

The measured output torque  $T_M$  (right) and phase currents (left) for the proposed OTMIC control with TRO (a) and the conventional FOC (b) are shown in Fig. 68. In opposite to the simulation results, the experimental results for OTMIC control have slight asymmetry due to non-ideal speed reference by means of a load motor, influence of cogging torque and errors in feedback that could not have been completely avoided in experiment. However, the simulation results can be successfully validated with the experiment taking into account the FFT analyses of measured phase currents (left) and torque (right) shown in Fig. 68 (c) for both OTMIC and FOC approaches. The fast Fourier transform of measured phase currents for OTMIC control shows the requested 5<sup>th</sup> and 7<sup>th</sup> harmonics and parasitical 2<sup>nd</sup>, 3<sup>rd</sup> and 8<sup>th</sup> harmonics. It leads to evaluation of the 6<sup>th</sup> and 12<sup>th</sup> harmonics in the torque waveform. However, the measured electrical torque consists of the parasitical 2<sup>nd</sup> harmonic due to additional cogging torque produced by slot winding and inaccuracies in OTMIC control system and power lines. Nevertheless, an effect of cogging torque has not been a part of OTMIC control approach presented in Chapter 5 and can be investigated in the future work. However, these errors don't affect the system. In comparison to OTMIC control, the experimental results of the conventional FOC methods shows more inaccuracies that underlines the FOC sensitivity to the above listed errors.

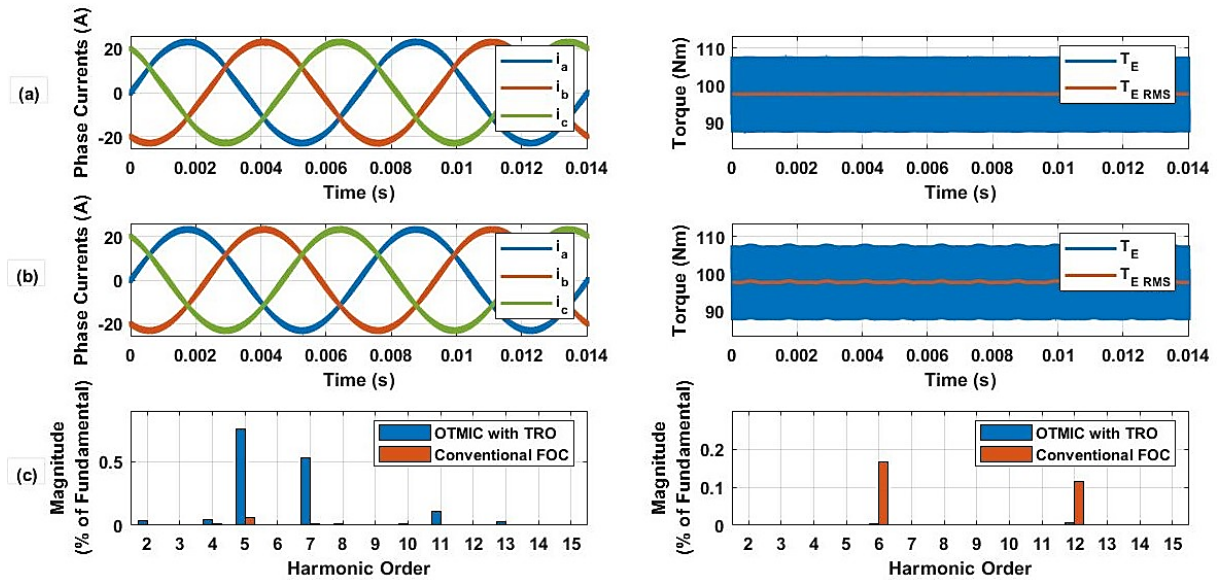


Fig. 67. Simulated Phase Currents and Electrical Torque  $T_E$  of (a): OTMIC with Torque Ripple Optimization; (b): Conventional FOC Control. (d): Harmonic Spectrum of Phase Current (left) and Torque (right) for Every Method.

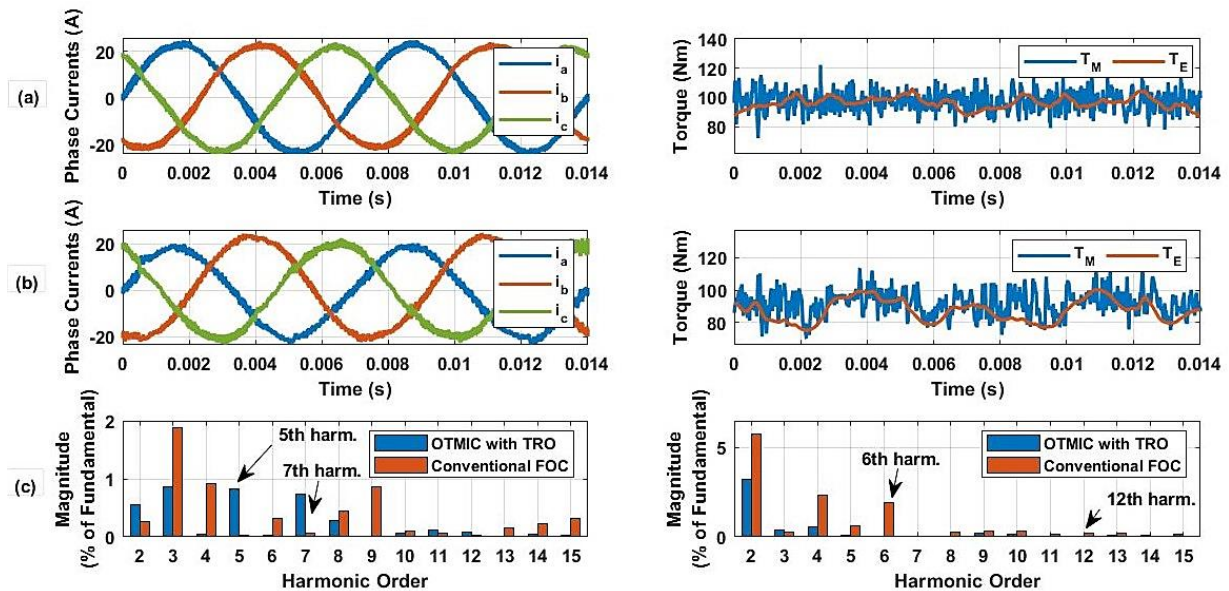


Fig. 68. Experimental Results of Measured Phase Currents and Output Torque  $T_M$  of (a): OTMIC with Torque Ripple Optimization; (b): Conventional FOC Control. (d): Harmonic Spectrum of Phase Current (left) and Torque (right) for Every Method.

As well as for the first control system implemented for the air gap winding motor, for a more detailed analysis of the torque ripples, the simulated RMS values of electrical torque  $T_E$  for OTMIC and FOC (a) are compared to the measured electrical torque waveforms (b) calculated according to (3.8) with the measured phase currents and B-Field as shown in Fig. 69. As the simulation results show, OTMIC control implementation for a combined winding wheel hub motor (blue) also leads to near-zero torque fluctuations in comparison to the conventional FOC control (red). It can also be confirmed by the measured electrical torque behavior. The influence of the load motor, cogging torque and sensors errors lead to slight larger torque ripples of OTMIC in comparison with simulation. However, the experimental

results underline the effectiveness of the optimization algorithm for torque ripples minimization used in the proposed OTMIC control.

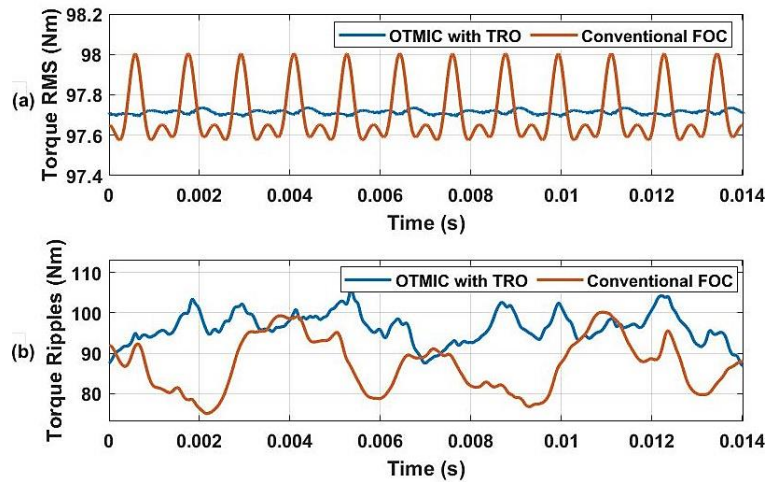


Fig. 69. Validation of Torque Ripples for OTMIC and FOC Methods (a): Simulated RMS Value of Electrical Torque; (b): Measured RMS Value of Electrical Torque.

Step-by-step calculations in the microcontroller of OTMIC control algorithm are shown in the Fig. 70. Left side of Fig. 70 describes the simulation results of the ideal OTMIC system without errors in current and electrical angle measurements as well as an influence of the load motor. The simulated ideal system is characterized by a nearly perfect match between the reference optimal phase current waveform  $i_{Ref}$  and the measured phase current actual values  $i$  as shown in Fig. 70 (left, a).

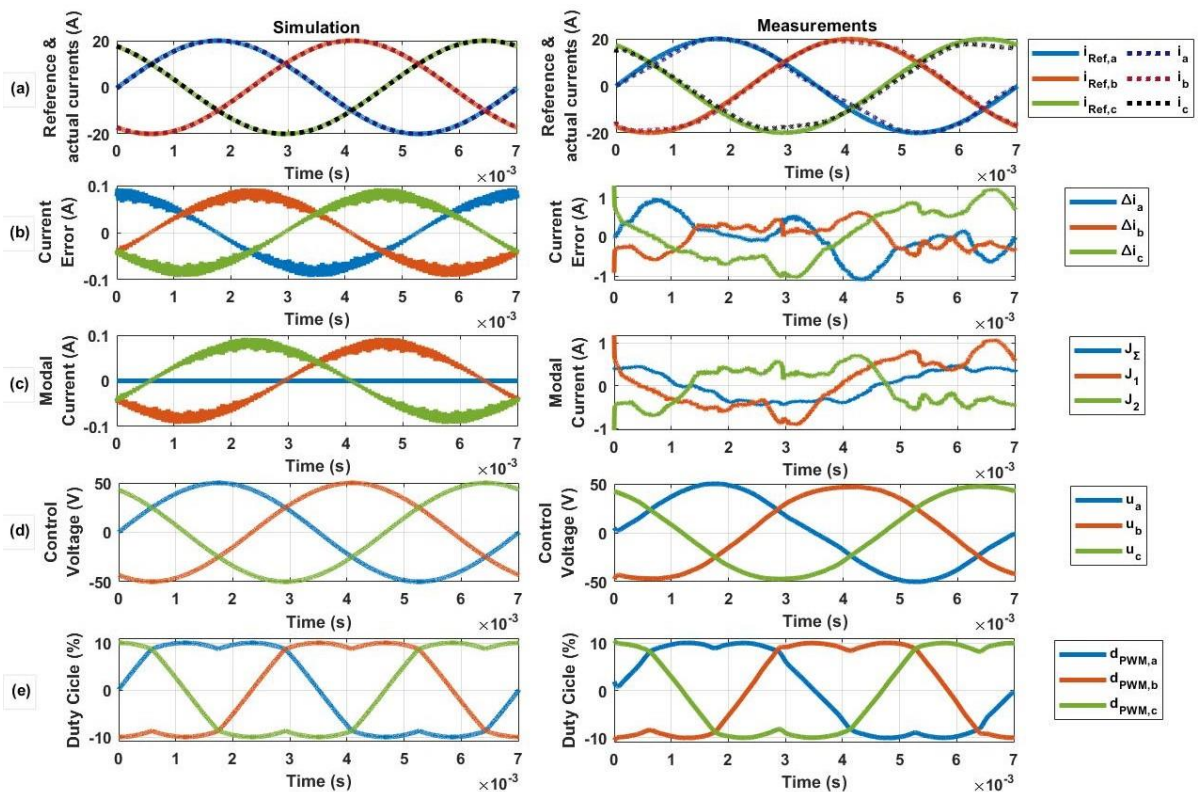


Fig. 70. Calculation Process of OTMIC Control Algorithm in the Microcontroller: Simulation (left) and Experimental Results (right).

As it is shown in Fig. 70 (left, b), small phase current error waveforms less than 0.1A can be seen. After the modal phase current transformation according to (5.25), shown in Fig. 70 (left, c) two completely decoupled modal currents  $J_1$  and  $J_2$  are compensated by two PID controllers separately. The redundant total current  $J_\Sigma$  is zero that underlines the absence of interferences in the feedback. PID controllers generate two control voltages transformed with equation (5.39) to three phase control voltages  $\underline{u}$  shown in Fig. 70 (left, d) and used as the inputs to MSVPWM. The MSVPWM output represents three phase duty cycles shown in Fig. 70 (left, e), calculated according to TABLE IX. and normalized relative to the supply voltage in the range from -1 and 1. The right side of Fig. 70 shows the experimental values of the signals illustrated on the left side. As it can be seen from Fig. 70 (right, a), in practice, the difference between the reference and the actual current values is more noticeable that is also emphasized by the waveforms of the phase current errors approximately equal to 1A at the maximum point and shown in the figure below. The measured redundant total current  $J_\Sigma$  is non-zero and reflects errors in the current measurement and other interference. However, as it can be seen from Fig. 70 (right, d and e), PID controllers compensate current errors and generate the necessary control voltages to set the motor in motion via MSVPWM, which also operates corresponding to the simulation results. Thus, it can be summarized that the OTMIC control algorithm presented in Chapter 5 is correct and can be verified by experiment. It can also be noted that the accuracy of the current sensors affects the control system according the star connection Kirchhoff's 1st Law (3.1). Therefore, for the correct operation of the OTMIC control algorithm for control of motors on an industrial scale, it is necessary to select accurately current sensors and take into account their features in order to reduce a feedback interference caused by changes in current sensor parameters, such as offset and sensitivity, under the influence of temperature and other factors.

As it has been mentioned above, due to the limited cooling capabilities of transistors, the phase current has been restricted to 20A. However, the simulation results shown in Fig. 71 for OTMIC with TRO (a) and the conventional FOC (b) confirm the effectiveness of OTMIC control under normal operating conditions with the rated power ( $\omega_M = 115 \text{ rad/s}$ ,  $T_{Ref} = 600 \text{ Nm}$ ) of the combined winding PM motor.

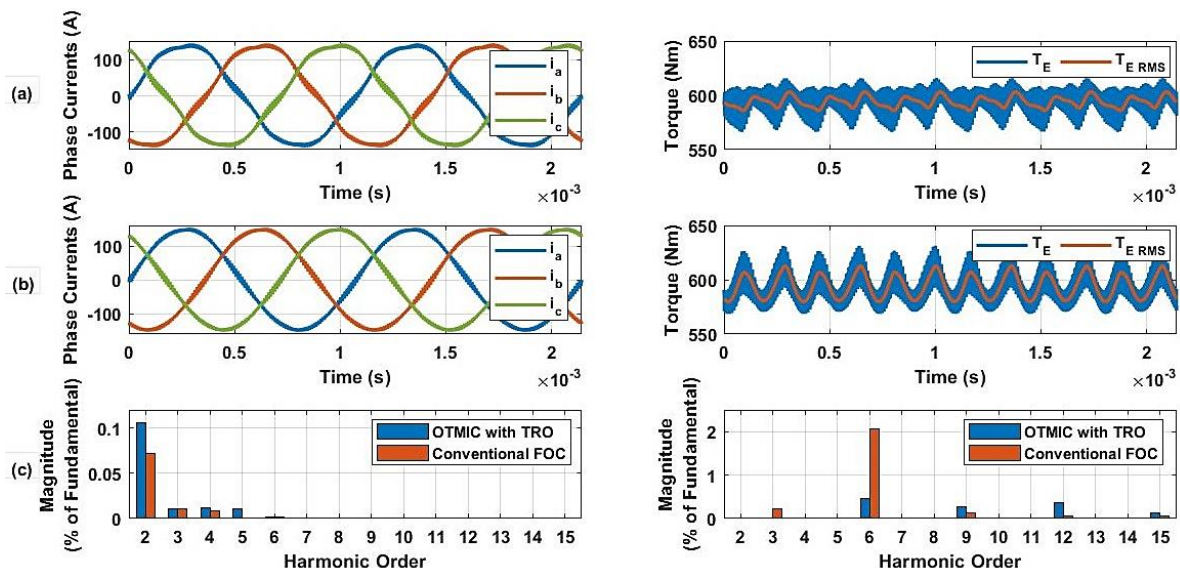


Fig. 71. Simulation Results of Phase Currents and Torque during Normal Operation with Rated Power of Combined Winding Motor (a): OTMIC with Torque Ripple Optimization; (b): Conventional FOC Control, (c): Harmonic Spectrum of Phase Current (left) and Torque (right) for Every Method.

As it can be noted from simulation results, increase of an angular velocity leads to additional torque fluctuations in OTMIC control caused by phase shifting between the reference and the actual phase currents. Nevertheless, in comparison to the conventional FOC, the proposed OTMIC control with the torque ripple minimization retains its benefits, which can be confirmed by FFT analyses of the simulated phase current and the electrical torque illustrated in Fig. 71 (c). Furthermore, in case of a more accurate PID parameters estimation for a high-speed motor control with a cogging torque compensation, the advantages of the OTMIC control may be more significant.

Thus, the effectiveness of the proposed Optimal Torque and Modal Current Control has also been confirmed in simulation and in practice on the combined winding wheel hub motor. The simulation and the experimental results of torque and currents behaviors of OTMIC has also been compared to the conventional Field Oriented Control. The FFT analyses and the direct comparison of torque fluctuations show better results of the Optimal Torque and Modal Current Control in comparison to FOC. In addition, the simulation results of the OTMIC control algorithm operation in microcontroller has been successfully verified by experiment.

## 7. Conclusion

This dissertation thesis proposes a Combined Optimal Torque and Modal Current Control method (OTMIC) for high-power PMSM motors with very low phase inductance, which is quite simple to implement on a standard industrial microcontroller and can be used in high-frequency control systems. Each of conventional vector control approaches known for today, from the point of view of application to a low inductance and simultaneously high-power PMSM are ineffective due to their time-consuming and complexity of implementation. It is related to the fact that these methods were designed for standard PMSM motors specified by a high phase inductance due to the large volume of copper in the stator winding, that does not require a high switching frequency of the inverter. On the other side of the ledger control methods designed for low inductance motors often for BLDC motors with six-step-commutation do not consider a high motor power. New design technologies of PMSM as air gap winding or combined winding can simultaneously reduce the weight of the engine while increasing its power, which leads to a decrease of phase inductance and requires a high switching frequency and high controller power to make every calculation in every sampling step.

Compared to the well-known Field Oriented Control (FOC) or other vector control methods based on the complex and cumbersome Clarke-Park Transformations, the proposed Combined Optimal Torque and Modal Current Control is deprived of such transformations and, thus, can be implemented more efficiently and simpler in terms of high frequency PM motor control, when the calculation time in microcontroller matters. The proposed in Chapter 5 OTMIC control has the capability of motor losses or torque ripples minimization without including an observer to the system, which is a great advantage in high frequency systems, when microcontroller calculation time matters. Described in Chapters 5.1 and 5.2, the OTMIC optimization algorithm can be investigated by means of a waveform calculation of three phase currents used as reference values in the Modal Current Control. The optimization approach considers a spectrum of all B-field harmonics to estimate the appropriate current waveform off-line and employs a very fast table-lookup for real-time implementation in a microcontroller. A temperature influence on the motor parameters or B-Filed harmonic coefficients can also be considered in the optimization algorithm. The Modal Current Control described in Chapter 5.3 and included in the OTMIC approach guarantees system stability, very fast dynamic response and matching of a given reference model. The full structure of the Combined Optimal Torque and Modal Current Control is presented in Chapter 5.5. Verification of the proposed OTMIC control described in Chapter 6 has been implemented using air gap winding and combined winding low inductance wheel hub motors with a phase inductance of only 1.5  $\mu\text{H}$  and 45  $\mu\text{H}$  operated at 48V and 650V, respectively. Both systems have been carried out using 100 kHz PWM switching frequency. Moreover, the simulation and experimental results of the OTMIC control have been compared with the conventional FOC approach.

The simulation results show that due to the transformations used in the conventional FOC, the phase currents waveforms don't have additional harmonics and are nearly ideally sinusoidal. It means that in case of a non-ideal B-Field waveform, it is difficult to adapt the phase current waveform to the specified requirements of torque or motor losses. On frequent occasions, for a conventional PMSM with high phase inductance, this problem is solved with an observer included to the system for compensation of B-Field additional harmonics. However, this solution is very complicated and difficult to apply using a common low-cost microcontroller for a high-frequency control of low inductance PMSMs with a large number of poles. Experimentally, due to a very low motor time constant and a large number of poles,

the Clarke-Park Transformations introduce additional errors uncompensated by a PID controller. It leads to significant phase current and torque deviations from the values given. In addition, due to Clarke-Park transformation, a high-frequency control system is more sensitive to errors in current and angle measurements.

The proposed Combined Optimal Torque and Modal Current Control shows a very good match between the experimental and theoretical results in comparison to the FOC. The measured results of the OTMIC step response show a very high system dynamics. Due to very low motor inductances and high switching frequency, parasitic inductances or capacities of a power line and supply are visible, but do not affect the control. The experimental results of normal operation of both wheel hub motors with a constant speed and reference torque underline the main advantages of the OTMIC control irrespective of small errors in electrical angle and current measurement, speed fluctuations due to the influence of the load motor and motor parameters changes, such as, increase in phase resistance as a function of temperature. In addition, the experimental results show, that the OTMIC control is less sensitive to errors in current measurements, as current sensor sensitivity or offset voltage changes, compared to the conventional method. Nevertheless, the OTMIC control needs an accurate current measurement to fulfill the star connection Kirchhoff's 1st Law, on which the Modal Current Control is based. However, this condition can be satisfied with the right choice of current sensors.

Summarizing, the Combined Optimal Torque and Modal Current Control of a low inductance high-power PM motor has the following advantages:

- simplicity of implementation using a common low-cost microcontroller;
- minimization of motor losses or torque ripples without use of an observer;
- ability to implement a back-EMF compensation and a field weakening with any type of PWM;
- ability to assess the state of the system by the value of the redundant modal total current  $J_{\Sigma}$ , which in ideal system condition should be zero;
- compatibility with other conventional electric motors such as PMSMs or BLDCs with a high phase inductance and any waveform of B-Field.

In addition to the OTMIC control, this dissertation provides an optimal solution of the optimization problem for a multiphase interleaved buck/boost converter by reducing weight as well as the total converter losses. This algorithm can be used for low-cost systems with a low inductance high-power PMSM controlled with six-step-commutation and the additional source current control by means of a multiphase interleaved buck/boost converter without using high-frequency transistors due to converter optimization. The interleaved converter optimization algorithm described in Chapter 4 takes into account the power electronic characteristics, electromagnetic properties of inductor coils and required operating conditions such as input supply DC voltage, rated output current and switching frequency. Moreover, the optimization model can be implemented with any kind of coil geometry and number of phases in an interleaved converter to obtain an optimal converter weight and total losses. The chain structure of the coil mathematical nonlinear model (voltage – magnetic induction – magnetic field intensity – current) describes the main principle of optimization. It permits to calculate a real nonlinear current form in the coil with consideration of the magnetization and saturation effects in it. This nonlinear coil model allows to find the optimal coil parameters to minimize a converter weight and total losses with the given supply converter voltage, rated current and switching frequency. The algorithm has been successfully tested and validated in practice on two prototypes of three phase interleaved buck converters with the different rated current values. The experimental results show minimal errors between the simulation and the test. The optimization algorithm can be used in compact, portable and low-cost



systems with low inductance PMSM where a hardware size matters, for example, in an electric scooters or longboards. In addition, the interleaved converter structure allows to reduce switching frequency by increasing the number of converter phases that is very important for low inductance air gap winding motors. Low-cost commutation control can be implemented with only one current sensor and does not have a trigonometric transformation in comparison with the vector control approach. However, the simulation and the experimental results show high phase current ripples in the commutation interval, which limit the supply voltage and rated current range for this control method and make it preferable to use the high-frequency OTMIC control.

There are many aspects relevant to the low inductance high-power PMSM control need to be explored in the future. The following proposals are made based on the research reported in this thesis.

In the field of a six-step commutation control with optimization of a buck-boost converter, the main suggestions for future work may be inclusion of a converter thermal model into the optimization algorithm. The results of this optimization may give a minimal loss with optimal converter weight including the weight of a cooling system. However, for the successful implementation of this idea, the thermal model must be described accurately enough. Another branch in the development of a six-step commutation control of low inductance PMSMs may be implementation of an algorithm aimed to reduce phase current peaks during commutation interval.

From the point of view of the Combined Optimal Torque and Modal Current Control, the opportunities for further research could be much greater. The first thing that can be investigated is implementation of this control method for conventional permanent magnet synchronous motors. This research will show the effectiveness of this method in control systems with a high cogging torque and at over high motor speeds, where a high switching frequency is not required, and the simplicity of the algorithm is no object. In the context of the OTMIC control of air gap or combined winding motors, over high-speed operation and evaluation of a cogging torque are also an important task that have to be solved for the successful development of e-Mobility.

## References

- [1] R. Kasper, D. Golovakha, "Combined Optimal Torque Feedforward and Modal Current Feedback Control for Low Inductance PM Motors", in submission process.
- [2] R. Kasper, D. Golovakha and F. Süberkrüb, "Combined Optimal Torque and Modal Current Control for Low Inductance PM Motor," 2019 IEEE International Conference on Mechatronics (ICM), Ilmenau, Germany, 2019, pp. 491-497.
- [3] R. Kasper, "Game-Changing Lightweight E-Motor Design Enables Unrivalled In-Wheel Drives and Other Applications.," In: EUROFORUM Deutschland GmbH (eds) CTI SYMPOSIUM 2018. Proceedings. Springer Vieweg, Berlin, Heidelberg.
- [4] O. Stamann, S. Jüttner, J. Sauerhering, A. Zörnig and R. Kasper, „Untersuchung von doppelseitig klebenden Elektroisierfolien mit wärmeleitfähigen Klebstoffschichten zum Fügen der Luftspaltwicklung von Leichtbau-Elektroantrieben“; In: 14. Magdeburger Maschinenbau-Tage 2019 - Magdeburger Ingenieurtag - 24. und 25. September 2019 : Tagungsband: 24. und 25. September 2019.
- [5] R. Kasper, M. Schmidt, R. Hinzelmann, A. Zörnig and N. Borchardt, "New Mathematical Approach for Eddy Current Loss in Air-Gap-Windings in a PMSM," 2019 IEEE 13th International Conference on Power Electronics and Drive Systems (PEDS), Toulouse, France, 2019, pp. 1-5.
- [6] S. Perekopskiy and R. Kasper, "Development and validation of a new kind of coupling element for wheel-hub motors," AIP Conference Proceedings, 2018.
- [7] D. Golovakha and R. Kasper, "Optimization of a multiphase interleaved buck converter based on electromagnetic processes in its elements," 2018 IEEE International Telecommunications Energy Conference (INTELEC), Turin, 2018, pp. 1-8.
- [8] D. Golovakha, H. Amiri and R. Kasper, „Theoretische Modellierung und experimentelle Validierung der Verlustleistung eines dreiphasigen Abwärtswandlers für die Ansteuerung eines Radnabenmotors mit geringer Induktivität,“ 13. Magdeburger Maschinenbau-Tage 2017. AUTONOM, VERNETZT, NACHHALTIG., Otto-von-Guericke-Universität Magdeburg 2017.
- [9] N. Borchardt and R. Kasper, "Analytical magnetic circuit design optimization of electrical machines with air gap winding using a Halbach array," 2017 IEEE International Electric Machines and Drives Conference (IEMDC), Miami, FL, 2017, pp. 1-7.
- [10] A. Zörnig, R. Hinzelmann and R. Kasper, „Der reibungsarme Radnabenmotor mit Radialrillenkugellagern,“ 15. Gemeinsames Kolloquium Konstruktionstechnik, Duisburg, Okt. 2017.
- [11] A. Zörnig, R. Hinzelmann, S. Perekopskiy and R. Kasper, „Vergleich der Berechnung und Messung der Verluste in Wälzlager und Dichtungen der Radnabenmotoren der OvGU,“ In: 13. Magdeburger Maschinenbau-Tage, Magdeburg, Sept. 2017.

- [12] R. Kasper and N. Borchardt, "Boosting Power Density of Electric Machines by Combining Two Different Winding Types," In: Proceedings of the 7th IFAC Symposium on Mechatronic Systems, Loughborough University, UK, September 5-8, 2016, S. 322–329.
- [13] N. Borchardt and R. Kasper, "Nonlinear design optimization of electric machines by using parametric Fourier coefficients of air gap flux density," 2016 IEEE International Conference on Advanced Intelligent Mechatronics (AIM), Banff, AB, 2016, pp. 645-650.
- [14] N. Borchardt, R. Hinzelmann, D. S. Pucula, W. Heinemann and R. Kasper, "Winding Machine for Automated Production of an Innovative Air-Gap Winding for Lightweight Electric Machines," in IEEE/ASME Transactions on Mechatronics, vol. 21, no. 3, pp. 1509-1517, June 2016.
- [15] A. Zörnig, R. Hinzelmann and R. Kasper, „Methodische Konstruktion eines Radnabenmotors mit Radialfluss-Luftspaltwicklung für Kleinwagen“. 14. Gemeinsames Kolloquium Konstruktionstechnik, Rostock, Okt. 2016.
- [16] A. Zörnig, D. D. Tran, D. V. Nguen, S. Höllwarth, R. Kasper, „Der Ringmotor mit Luftspaltwicklung als Direktantrieb für Fahrzeuge“. In: 12. Magdeburger Maschinenbau-Tage, Magdeburg, Sept. - Okt. 2015.
- [17] A. Zörnig and R. Kasper, "Engineering design of electrical wheel hub motors with air gap winding for vehicles", VDI Constr., 2015, 6, pp. 40–43.
- [18] N. Borchardt, "Modeling, electromechanical design and validation of a wheel hub motor with slotless air gap winding and high gravimetric power density". Ph.D. Dissertation, Otto-von-Guericke-Univ., Magdeburg, Germany, 2015.
- [19] R. Kasper, N. Borchardt and W. Heinemann, "Electric motor having an ironfree winding," Patent DE 10 2011 111 352 B4, Nov. 26, 2015.
- [20] N. Borchardt, B. Penzlin and R. Kasper, "Mechatronic model of a novel slotless permanent magnet DC-motor with air gap winding design," 2013 IEEE/ASME International Conference on Advanced Intelligent Mechatronics, Wollongong, NSW, 2013, pp. 1175-1180.
- [21] A. Zörnig, N. Vittayaphadung and R. Kasper, "Deformation and Modes of a Wheel Hub Motor with Air Gap Winding," 11. Magdeburger Maschinenbau-Tage, Magdeburg, Sept. 2013.
- [22] N. Borchardt, R. Kasper and W. Heinemann, "Design of a wheel-hub motor with air gap winding and simultaneous utilization of all magnetic poles," 2012 IEEE International Electric Vehicle Conference, Greenville, SC, 2012, pp. 1-7.
- [23] F. Martini, "World-record electric motor for aircraft," Siemens press, 24 March (2015). Available at: <http://www.siemens.com/press/en/feature/2015/corporate>.
- [24] A.J. Rix, M.J. Kamper, "Radial-Flux Permanent-Magnet Hub Drives: A Comparison Based on Stator and Rotor Topologies," IEEE Industrial Electronics, vol. 59, no. 6, pp. 2475-2483, Jun. 2012. R. L.
- [25] Protean Electric Limited: [www.proteanelectric.com](http://www.proteanelectric.com) (as of 21.04.2020).

- [26] J. Nagashima, "Wheel Hub Motors for Automotive Applications", Proceedings of the 21st Hybrid and Fuel Cell Electric Vehicle Symposium & Exhibition, Monaco, 02-06.04.2005.
- [27] C. Pille, F. Horch, „Von der Idee zum gießtechnisch umgesetzten Produkt,“ AluMag Light Weight Technology Road Show, 2011.
- [28] Hanselka, Holger: Der Elektromobile Antriebsstrang – Leicht und Zuverlässig. Antrieb Zukunft, Fraunhofer-Forum, 16.04.2012, München. [www.fraunhofer.de](http://www.fraunhofer.de) (as of 21.04.2020).
- [29] Schaeffler AG: Mobility for tomorrow. [www.schaeffler-events.com](http://www.schaeffler-events.com) (as of 21.04.2020).
- [30] T. Schencke, „Entwicklungsstand elektrischer Radnabenmotor,“ ACOD Workshop - Anforderungen an die Elektrifizierung von PKW-Antriebssträngen, Saalfeld, 06.12.2012.
- [31] Siemens AG: Antrieb in der Felge. [www.new.siemens.com/](http://www.new.siemens.com/) (as of 21.04.2020).
- [32] Fraunhofer-Institut für Fertigungstechnik und Angewandte Materialforschung: Entwicklung von Komponenten für Elektrofahrzeuge. [www.ifam.fraunhofer.de](http://www.ifam.fraunhofer.de) (as of 21.04.2020).
- [33] Schaeffler AG: Der Antrieb für das Stadtauto von morgen – Schaeffler und Ford zeigen Ideenauto mit E-Wheel Drive. [www.schaeffler.de](http://www.schaeffler.de) (as of 21.04.2020).
- [34] Tesla Motors, [www.tesla.com](http://www.tesla.com) (as of 21.04.2020).
- [35] Audi technology portal: Audi e-tron quattro concept. [www.audi-technology-portal.de](http://www.audi-technology-portal.de) (as of 21.04.2020).
- [36] B. Gombert, R. Fischer and W. Heinrich, „Elektrische Radnabenmotoren - Konstruktionskriterien und Fahrzeugintegration,“ In: ATZelektronik 01/2010, Vol. 5, Springer Automotive Media, 2010. – ISSN 1862-1791.
- [37] M. Schünemann, „Konzeption, Entwicklung und Umsetzung einer Fahrdynamikregelung für Kraftfahrzeuge mit elektrischen Einzelradantrieben“, Ph.D. Dissertation, Otto-von-Guericke-Univ., Magdeburg, Germany, 2017.
- [38] M. Mitschke, H. Wallentowitz, „Dynamik der Kraftfahrzeuge,“ 4. Aufl. Berlin, Heidelberg, New York: Springer Verlag, 2004. – ISBN 978-3-540-42011-8.
- [39] Stulrajter, Marek, Valéria Hrabovcová and Marek Franko. "PERMANENT MAGNETS SYNCHRONOUS MOTOR CONTROL THEORY." (2007).
- [40] Paitandi, Sourabh and Mainak Sengupta. "Analysis, design and implementation of sensorless V/f control in a surface-mounted PMSM without damper winding." *Sādhanā* 42 (2017): 1317-1333.
- [41] D. Sato and J. Itoh, "Open-loop control for permanent magnet synchronous motor driven by square-wave voltage and stabilization control," 2016 IEEE Energy Conversion Congress and Exposition (ECCE), Milwaukee, WI, 2016, pp. 1-8.
- [42] G. Andreescu, C. Coman, A. Moldovan and I. Boldea, "Stable V/f control system with unity power factor for PMSM drives," 2012 13th International Conference on Optimization of Electrical and Electronic Equipment (OPTIM), Brasov, 2012, pp. 432-438.
- [43] I. Boldea, A. Moldovan and L. Tutelea, "Scalar V/f and I-f control of AC motor drives: An overview," 2015 Intl Aegean Conference on Electrical Machines & Power Electronics

- (ACEMP), 2015 Intl Conference on Optimization of Electrical & Electronic Equipment (OPTIM) & 2015 Intl Symposium on Advanced Electromechanical Motion Systems (ELECTROMOTION), Side, 2015, pp. 8-17.
- [44] M. Fatu, R. Teodorescu, I. Boldea, G. Andreescu and F. Blaabjerg, "I-F starting method with smooth transition to EMF based motion-sensorless vector control of PM synchronous motor/generator," 2008 IEEE Power Electronics Specialists Conference, Rhodes, 2008, pp. 1481-1487.
- [45] A. Borisavljevic, H. Polinder and J. A. Ferreira, "Realization of the I/f control method for a high-speed permanent magnet motor," The XIX International Conference on Electrical Machines - ICEM 2010, Rome, 2010, pp. 1-6.
- [46] Abu-Rub, Haithem, Atif Iqbal and Jaroslaw Guzinski. "High performance control of AC drives with MATLAB/Simulink models." (2012).
- [47] Liuping Wang; Shan Chai; Dae Yoo; Lu Gan; Ki Ng, "PID Control System Design for Electrical Drives and Power Converters," in PID and Predictive Control of Electrical Drives and Power Converters using MATLAB / Simulink , , IEEE, 2015, pp.41-85.
- [48] A. Lidozzi, L. Solero, F. Crescimbeni and R. Burgos, "Vector control of trapezoidal back-EMF PM machines using pseudo-Park transformation," 2008 IEEE Power Electronics Specialists Conference, Rhodes, 2008, pp. 2167-2171.
- [49] Y. Li, P. Zhang, J. Hang, S. Ding, L. Liu and Q. Wang, "Comparison of dynamic characteristics of field oriented control and model predictive control for permanent magnet synchronous motor," 2018 13th IEEE Conference on Industrial Electronics and Applications (ICIEA), Wuhan, 2018, pp. 2431-2434.
- [50] Q. Song, Y. Li, C. Jia, « A Novel Direct Torque Control Method Based on Asymmetric Boundary Layer Sliding Mode Control for PMSM, » *Energies*, Vol. 11, pp.1-15, 2018.
- [51] F. Niu, K. Li and Y. Wang, "Direct Torque Control for Permanent-Magnet Synchronous Machines Based on Duty Ratio Modulation," in *IEEE Transactions on Industrial Electronics*, vol. 62, no. 10, pp. 6160-6170, Oct. 2015.
- [52] M. S. Merzoug and F. Naceri, "Comparison of field-oriented control and direct torque control for permanent magnet synchronous motor (PMSM)", *International Journal of Electrical and Computer Engineering*, vol. 2, no. 9, pp. 1797-1802, 2008.
- [53] F. Korkmaz, İ. Topaloğlu, M. F. Çakir and R. Gürbüz, "Comparative performance evaluation of FOC and DTC controlled PMSM drives," 4th International Conference on Power Engineering, Energy and Electrical Drives, Istanbul, 2013, pp. 705-708.
- [54] Zaihidee, Fardila M., Saad Mekhilef and Marizan Mubin. "Robust Speed Control of PMSM Using Sliding Mode Control (SMC)—A Review." (2019).
- [55] Kaboli, Aghay, A. Mohammadi, Alireza Fallahpour, Jeyraj Selvaraj and Nasrudin Abd Rahim. "Fuzzy logic based encoder-less speed control of PMSM for hub motor drive." (2017).

- [56] C. K. Lad and R. Chudamani, "Simple overlap angle control strategy for commutation torque ripple minimisation in BLDC motor drive," in *IET Electric Power Applications*, vol. 12, no. 6, pp. 797-807, 7 2018.
- [57] J. Wang, X. Huang, S. Zhao and Y. Fang, "Direct torque control for brushless DC motors in aerospace applications with single sided matrix converters with reduced torque ripple," *IECON 2017 - 43rd Annual Conference of the IEEE Industrial Electronics Society*, Beijing, 2017, pp. 4143-4149.
- [58] M. Masmoudi, B. E. Badsı and A. Masmoudi, "DTC of B4-Inverter-Fed BLDC Motor Drives With Reduced Torque Ripple During Sector-to-Sector Commutations," in *IEEE Transactions on Power Electronics*, vol. 29, no. 9, pp. 4855-4865, Sept. 2014.
- [59] M. R. Feyzi, M. Shafiei, M. Bahrami Kouhshahi and S. A. K. Mozaffari Niapour, "Position sensorless direct torque control of Brushless DC motor drives based on sliding mode observer using NSGA-II Algorithm optimization," *2011 2nd Power Electronics, Drive Systems and Technologies Conference*, Tehran, 2011, pp. 151-156.
- [60] Tarczewski, Tomasz, M. Skiwski, L. Niewiara and Lech M. Grzesiak. "High-performance PMSM servo-drive with constrained state feedback position controller." (2018).
- [61] Xu, Wen-Jun. "Permanent Magnet Synchronous Motor with Linear Quadratic Speed Controller." (2012).
- [62] Ramana, N. Venkata and V. N. Sastry. "A Novel Speed Control Strategy for Five Phases Permanent Magnet Synchronous Motor with Linear Quadratic Regulator." (2015).
- [63] M. A. M. Cheema, J. E. Fletcher, D. Xiao and M. F. Rahman, "A Linear Quadratic Regulator-Based Optimal Direct Thrust Force Control of Linear Permanent-Magnet Synchronous Motor," in *IEEE Transactions on Industrial Electronics*, vol. 63, no. 5, pp. 2722-2733, May 2016.
- [64] L. M. Grzesiak and T. Tarczewski, "Permanent magnet synchronous motor discrete linear quadratic speed controller," *2011 IEEE International Symposium on Industrial Electronics*, Gdansk, 2011, pp. 667-672.
- [65] A. G. de Castro, W. C. A. Pereira, T. E. P. Almeida, C. M. R. de Oliveira, J. R. B. A. Monteiro and A. A. de Oliveira, "Improved finite control-set model-based direct power control of BLDC motor with reduced torque ripple," *2016 12th IEEE International Conference on Industry Applications (INDUSCON)*, Curitiba, 2016, pp. 1-6.
- [66] D. Flieller, N. K. Nguyen, P. Wira, G. Sturtzer, D. O. Abdeslam, and J. Merckle, "A Self-Learning Solution for Torque Ripple Reduction For Non Sinusoidal Permanent Magnet Motor Drives Based on Artificial Neural Networks," *IEEE Transactions on Industrial Electronics*, vol. 61, no. 2, pp. 655-666, feb 2014.
- [67] C. Xia, B. Ji and Y. Yan, "Smooth Speed Control for Low-Speed High-Torque Permanent-Magnet Synchronous Motor Using Proportional-Integral-Resonant Controller," in *IEEE Transactions on Industrial Electronics*, vol. 62, no. 4, pp. 2123-2134, April 2015.
- [68] P. Kakosimos, M. Beniakar, Y. Liu and H. Abu-Rub, "Model predictive control for permanent magnet synchronous motor drives considering cross-saturation effects," *2017*

- IEEE Applied Power Electronics Conference and Exposition (APEC), Tampa, FL, 2017, pp. 1880-1885.
- [69] C. Li, C. Xia, Z. Zhou, T. Shi and Y. Yan, "Torque ripple reduction of permanent magnet synchronous motors based on predictive sequence control," 2017 20th International Conference on Electrical Machines and Systems (ICEMS), Sydney, NSW, 2017, pp. 1-5.
- [70] M. Zou, S. Wang, M. Liu and K. Chen, "Model Predictive Control of Permanent-Magnet Synchronous Motor with Disturbance Observer," 2019 IEEE International Symposium on Predictive Control of Electrical Drives and Power Electronics (PRECEDE), Quanzhou, China, 2019, pp. 1-6.
- [71] S. Yuntao, X. Xiang, Z. Yuan, Z. Hengjie and S. Dehui, "Design of explicit model predictive control for PMSM drive systems," 2017 29th Chinese Control And Decision Conference (CCDC), Chongqing, 2017, pp. 7389-7395.
- [72] S. Chai, L. Wang, and E. Rogers, "Model predictive control of a permanent magnet synchronous motor with experimental validation," *Control Engineering Practice*, vol. 21, no. 11, pp. 1584–1593, 2013.
- [73] Z. Ma, S. Saeidi and R. Kennel, "FPGA Implementation of Model Predictive Control With Constant Switching Frequency for PMSM Drives," in *IEEE Transactions on Industrial Informatics*, vol. 10, no. 4, pp. 2055-2063, Nov. 2014.
- [74] A. Abbaszadeh, D. Arab Khaburi and J. Rodríguez, "Predictive control of permanent magnet synchronous motor with non-sinusoidal flux distribution for torque ripple minimisation using the recursive least square identification method," in *IET Electric Power Applications*, vol. 11, no. 5, pp. 847-856, 5 2017.
- [75] Y. Zhang and H. Yang, "Model Predictive Torque Control of Induction Motor Drives With Optimal Duty Cycle Control," in *IEEE Transactions on Power Electronics*, vol. 29, no. 12, pp. 6593-6603, Dec. 2014.
- [76] Z. Zhou, C. Xia, Y. Yan, Z. Wang and T. Shi, "Torque Ripple Minimization of Predictive Torque Control for PMSM With Extended Control Set," in *IEEE Transactions on Industrial Electronics*, vol. 64, no. 9, pp. 6930-6939, Sept. 2017.
- [77] L. Dang, N. Bernard, N. Bracikowski and G. Berthiau, "Design Optimization with Flux Weakening of High-Speed PMSM for Electrical Vehicle Considering the Driving Cycle," in *IEEE Transactions on Industrial Electronics*, vol. 64, no. 12, pp. 9834-9843, Dec. 2017.
- [78] X. Zhu, Z. Xiang, C. Zhang, L. Quan, Y. Du, and W. Gu, "Coreduction of torque ripple for outer rotor flux-switching PM motor using systematic multi-level design and control schemes," *IEEE Trans. Ind. Electron.*, vol. 64, no. 2, pp. 1102-1112, Feb. 2017.
- [79] P. Sarkar and S. Bhunia, "SVPWM based vector control of PMSM drive in delta domain," 2017 International Conference on Electrical, Computer and Communication Engineering (ECCE), Cox's Bazar, 2017, pp. 5-10.
- [80] F. Wang, X. Mei, J. Rodriguez and R. Kennel, "Model predictive control for electrical drive systems-an overview," in *CES Transactions on Electrical Machines and Systems*, vol. 1, no. 3, pp. 219-230, September 2017.

- 
- [81] Tan, Bo, Zhiguang Hua, Lu Zhang and Chun Fang. "A New Approach of Minimizing Commutation Torque Ripple for BLDCM." (2017).
- [82] X. Chen and G. Liu, "Sensorless Optimal Commutation Steady Speed Control Method for a non-ideal Back-EMF BLDC Motor Drive System including Buck Converter," in *IEEE Transactions on Industrial Electronics*.
- [83] V. Viswanathan and J. Seenithangom, "Commutation Torque Ripple Reduction in the BLDC Motor Using Modified SEPIC and Three-Level NPC Inverter," in *IEEE Transactions on Power Electronics*, vol. 33, no. 1, pp. 535-546, Jan. 2018.
- [84] Y. Xu, Y. Wei, B. Wang and J. Zou, "A Novel Inverter Topology for Brushless DC Motor Drive to Shorten Commutation Time," in *IEEE Transactions on Industrial Electronics*, vol. 63, no. 2, pp. 796-807, Feb. 2016.
- [85] X. Li, C. Xia, Y. Cao, W. Chen and T. Shi, "Commutation Torque Ripple Reduction Strategy of Z-Source Inverter Fed Brushless DC Motor," in *IEEE Transactions on Power Electronics*, vol. 31, no. 11, pp. 7677-7690, Nov. 2016.
- [86] M. Bertoluzzo, G. Buja, R. K. Keshri and R. Menis, "Sinusoidal Versus Square-Wave Current Supply of PM Brushless DC Drives: A Convenience Analysis," in *IEEE Transactions on Industrial Electronics*, vol. 62, no. 12, pp. 7339-7349, Dec. 2015.
- [87] A. Serpi, G. Fois, M. Porru, A. Damiano and I. Marongiu, "Space vector control of permanent Magnet Brushless DC Machines," 2016 XXII International Conference on Electrical Machines (ICEM), Lausanne, 2016, pp. 1194-1200.
- [88] G. Buja, M. Bertoluzzo and R. K. Keshri, "Torque Ripple-Free Operation of PM BLDC Drives With Petal-Wave Current Supply," in *IEEE Transactions on Industrial Electronics*, vol. 62, no. 7, pp. 4034-4043, July 2015.
- [89] J. Fang, X. Zhou and G. Liu, "Precise Accelerated Torque Control for Small Inductance Brushless DC Motor," in *IEEE Transactions on Power Electronics*, vol. 28, no. 3, pp. 1400-1412, March 2013.
- [90] C. Xia, Y. Xiao, W. Chen and T. Shi, "Torque Ripple Reduction in Brushless DC Drives Based on Reference Current Optimization Using Integral Variable Structure Control," in *IEEE Transactions on Industrial Electronics*, vol. 61, no. 2, pp. 738-752, Feb. 2014.
- [91] Q. Xun and Y. Liu, "Commutation Torque-ripple Minimization for Brushless DC Motor Based on Quasi-Z-Source Inverter," 2018 XIII International Conference on Electrical Machines (ICEM), Alexandroupoli, 2018, pp. 1439-1445.
- [92] M. Esteki, B. Poorali, E. Adib and H. Farzanehfard, "Interleaved Buck Converter With Continuous Input Current, Extremely Low Output Current Ripple, Low Switching Losses, and Improved Step-Down Conversion Ratio," in *IEEE Transactions on Industrial Electronics*, vol. 62, no. 8, pp. 4769-4776, Aug. 2015.
- [93] D. Lyu, Y. Sun, C. A. Teixeira, Z. Ji, J. Zhao and Q. Wang, "A Modular Multilevel Dual Buck Inverter With Adjustable Discontinuous Modulation," in *IEEE Access*, vol. 8, pp. 31693-31709, 2020.



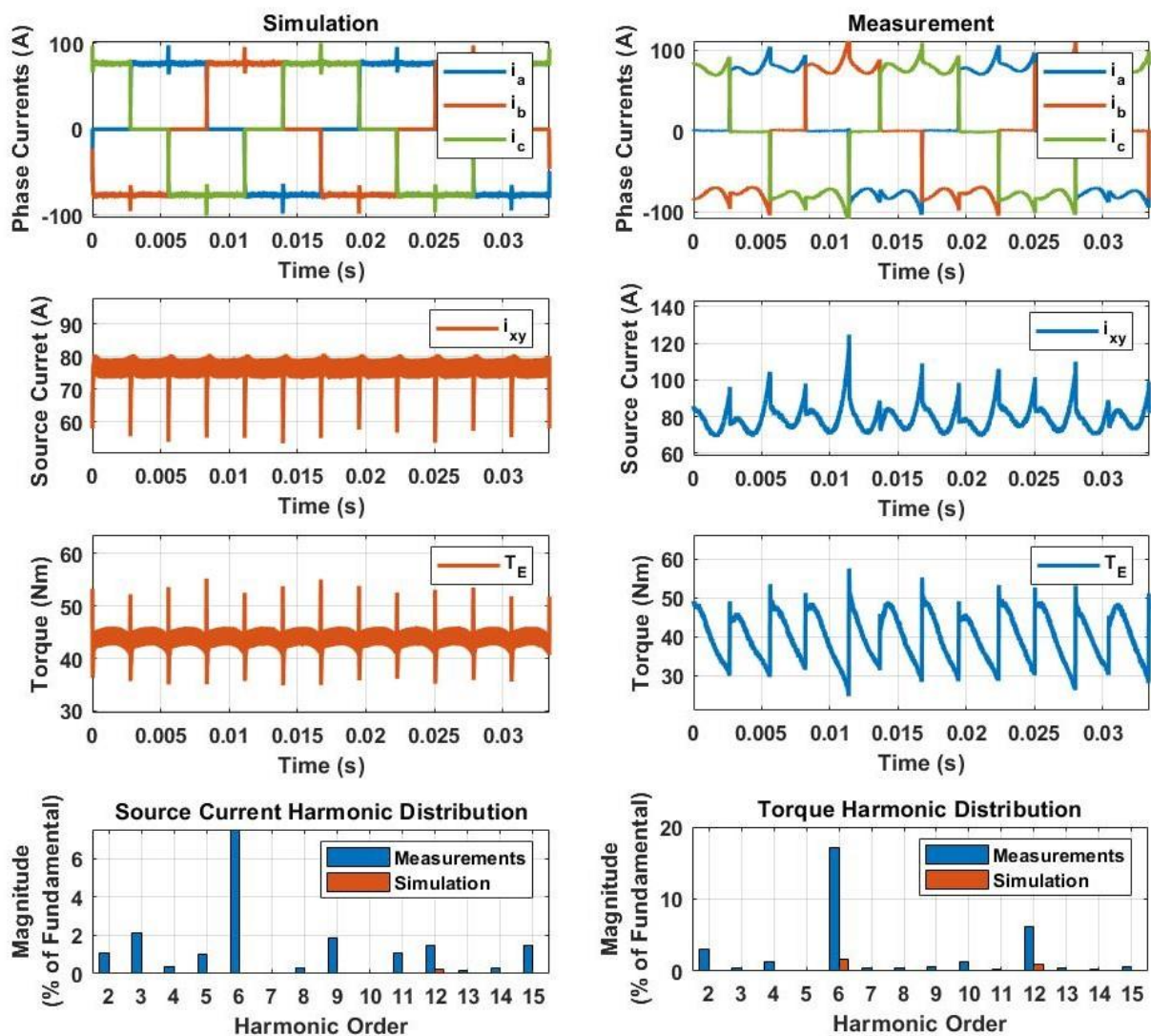
- [94] N. A. Dung, H. Hsieh, J. Lin, H. Chiu and J. Lai, "Design of Bidirectional DC-DC Converter for Energy Storage System in High Power Application," 2019 IEEE 4th International Future Energy Electronics Conference (IFEEEC), Singapore, Singapore, 2019, pp. 1-4.
- [95] L. Schrittwieser, M. Leibl, M. Haider, F. Thöny, J. W. Kolar and T. B. Soeiro, "99.3% Efficient Three-Phase Buck-Type All-SiC SWISS Rectifier for DC Distribution Systems," in IEEE Transactions on Power Electronics, vol. 34, no. 1, pp. 126-140, Jan. 2019.
- [96] Mclyman, C. W. T.. "Transformer and inductor design handbook." (1988).
- [97] Jiles, David and David L. Atherton. "Theory of ferromagnetic hysteresis." (1986).
- [98] Snelling, E. C. and David E. A. Giles. "Ferrites for inductors and transformers." (1983).
- [99] Mayergoyz, Isaak D.. "Mathematical models of hysteresis and their applications." (2003).
- [100] D. Graovac, M. Pürschel and A. Kiep, "MOSFET Power losses calculation using the datasheet parameters," Infineon Application Note, ver.1.1, (July 2006).
- [101] J. Rodriguez and P. Cortes, Predictive control of power converters and electrical drives, 1st ed. John Wiley & Sons, Inc., 2012.
- [102] D. J. Griffiths, Introduction to Electrodynamics. 4nd ed., Instock 2012, ISBN-13: 9780321856562.
- [103] Babel, Gerhard: Elektrische Antriebe in der Fahrzeugtechnik. 2. Aufl. Wiesbaden : Vieweg+Teubner Verlag, 2009. – ISBN 978-3-8348-0563-8.
- [104] Magnetics: Magnetics powder core catalog, 2015, Accessed January 2016, <https://www.mag-inc.com> (as of 21.04.2020).
- [105] Infineon catalog: OptiMOS 5 Power-Transistor, 100V, IPT015N10N5, 2015
- [106] Gan Systems, Board User Guide. Rev. 2016-06-07 GaN Systems Confidential, <https://gansystems.com> (as of 21.04.2020).
- [107] Allegro MicroSystems Datasheet, ACS730, 1 MHz Bandwidth, Galvanically Isolated Current Sensor IC in Small Footprint SOIC8 Package. ACS730-DS, Rev. 7 MCO-0000147. 2018.
- [108] KTR – Group Datasheet, DATAFLEX 32/... Torque Measuring Shaft Operating/Assembly instructions, KTR-N 49015 EN. Edition 5. ISO 16016. 2017-01-02 Pz.
- [109] Cypress, Semiconductor: 32-Bit Microcontroller FM4 Family Peripheral Manual Timer Part. Doc. No. 002-04858 Rev.\*B. 198 Champion Court San Jose, CA 951341709, 2017.
- [110] Kübler Incremental encoders Datasheet, A02H [www.kuebler.com/de](http://www.kuebler.com/de) (as of 21.04.2020).
- [111] TopCon Quadro Power Supply Unit Datasheet, [www.regatron.com](http://www.regatron.com) (as of 21.04.2020).
- [112] T-T Electric Datasheet, LAK 4160-C <http://www.t-telectric.com> (as of 21.04.2020).
- [113] Lorenz Messtechnik Datasheet, DR-2212 [www.lorenz-messtechnik.de](http://www.lorenz-messtechnik.de) (as of 21.04.2020).
- [114] Bieniek, Tomasz & Janczyk, Grzegorz & Sitnik, Adam & Messina, Angelo. (2019). The "first and euROPEAn siC eigTh Inches pilOt line" - REACTION project as a Driver for key European SiC Technologies focused on Power Electronics Development.

- 
- [115] Cypress, Semiconductor: 32-Bit Microcontroller FM4 Family Peripheral Manual Analog Macro Part. Doc. No. 002-04860 Rev.\*B. 198 Champion Court San Jose, CA 95134-1709, 2017.
- [116] Cypress, Semiconductor: FM4-176L-S6E2CC-ETH. Rev v13. San Jose, CA 951341709: Cypress, August 2014.
- [117] Cypress, Semiconductor: 32-Bit Microcontroller FM4 Family Peripheral Manual. Rev.\*D. San Jose, CA 95134-1709: Cypress Semiconductor, 2017. – Document Number: 002-04856.
- [118] Yang Yeepien and Ting Yiyuan, “Improved Angular Displacement Estimation Based on Hall-Effect Sensors for Driving a Brushless Permanent-Magnet Motor,” *IEEE Transactions on Industrial Electronics*, Vol. 61, No. 1, pp. 504-511, Jan. 2014.
- [119] D. Reigosa, D. Fernandez, C. González, S. B. Lee and F. Briz, "Permanent Magnet Synchronous Machine Drive Control Using Analog Hall-Effect Sensors," in *IEEE Transactions on Industry Applications*, vol. 54, no. 3, pp. 2358-2369, May-June 2018.
- [120] F. G. Capponi, G. D. Donato, L. D. Ferraro, O. Honorati, M. C. Harke, and R. D. Lorenz, “AC brushless drive with low-resolution hall-effect sensors for surface-mounted PM machines,” *IEEE Trans. Ind. Appl.*, vol. 42, no. 2, pp. 526–535, March/April 2006.

## Appendix

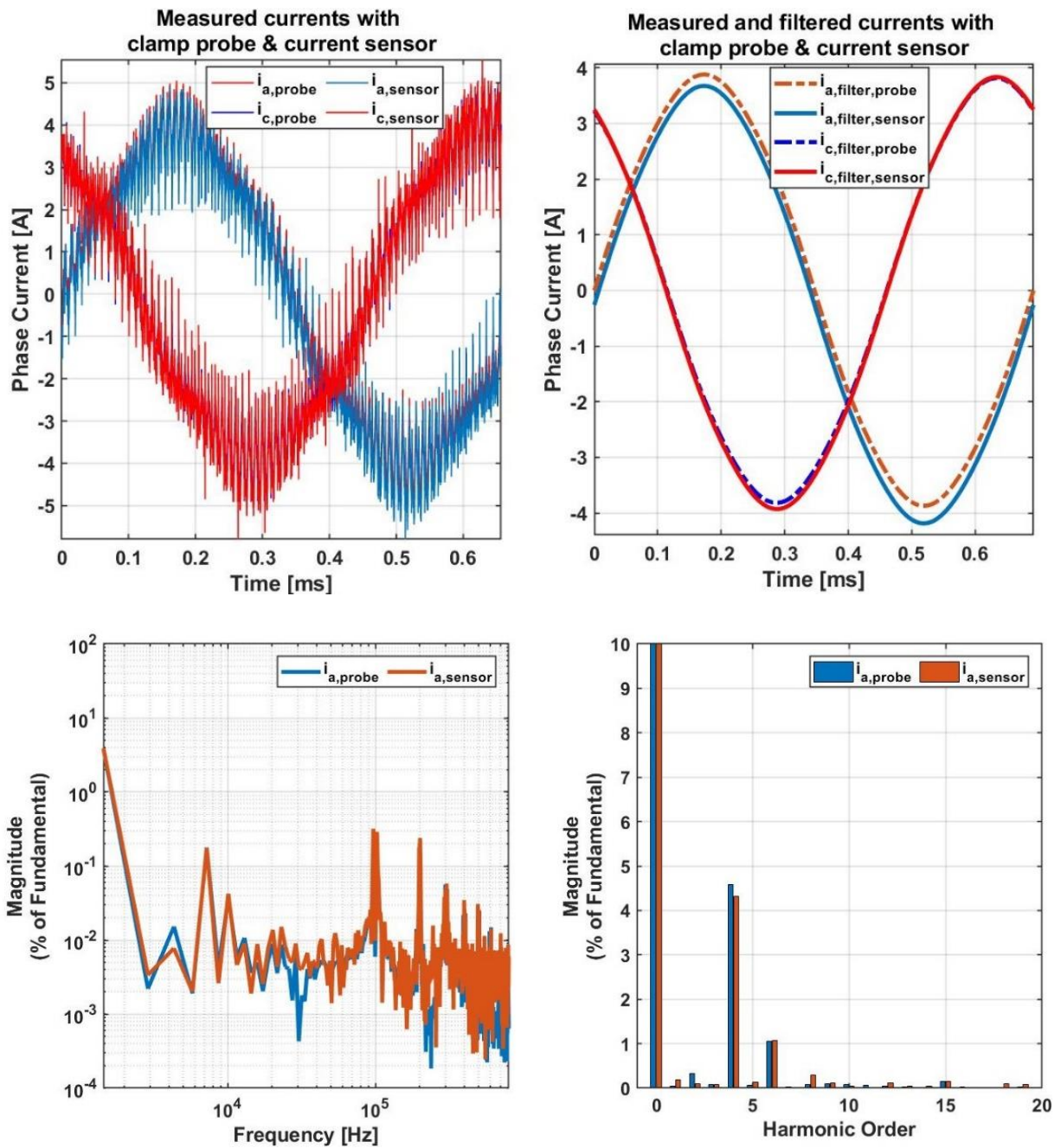
### Appendix A – Six-step Commutation with Source Current Control

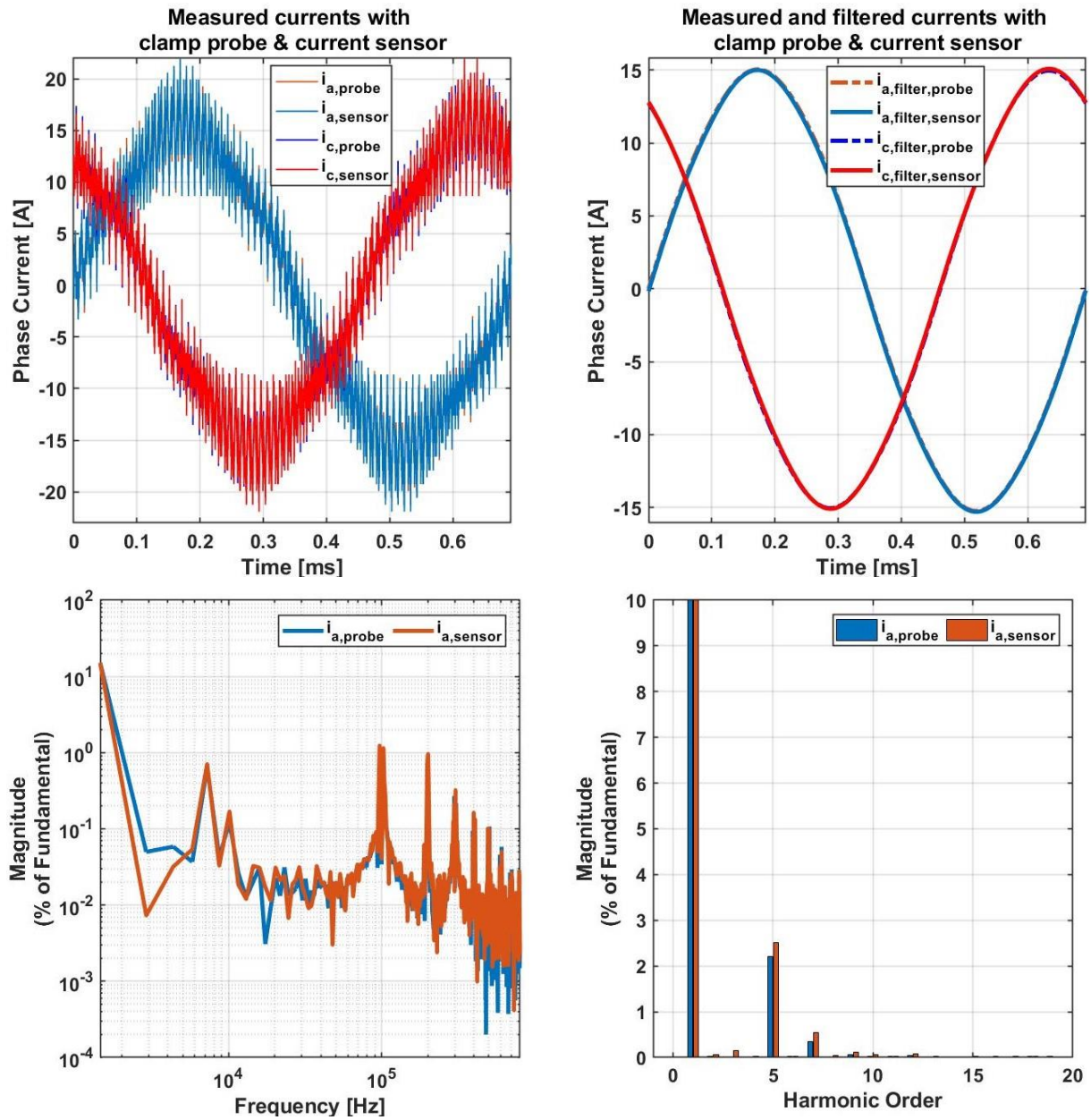
Simulation and measurement results have been obtained with the references  $\omega_M = 8 \text{ rad/s}$  and  $i_{Ref} = 80 \text{ A}$  for air gap winding wheel-hub motor presented in Chapter 6.2 with parameters in TABLE XII. The conventional six-step commutation with source current control described in Chapter 3.5 has been combined with optimized three-phase interleaved buck DC-DC converter presented in Chapter 4.3 in Fig. 32 and optimized according to the algorithm proposed in Chapter 4. Converter optimization algorithm allows to control air gap winding motor without the use of high switching frequency, which can be confirmed with results shown below.



## Appendix B – Accuracy Verification of Allegro Current Sensors

Figures below show the difference in current measurement using a current sensor Allegro ACS733 KLATR - 40ABT and the high-precision current probe Teledyne LeCroy CP031A.





The experiment has been carried out for current amplitudes 4 and 15 A using the circuit diagram shown below.

